Reaction calorimetry and structural crystal properties of non-ideal binary rhabdophane solid solutions ($Ce_{1-x}REE_xPO_4{\cdot}nH_2O$)

Alexander P. Gysi[*a,b], Nicole C. Hurtig[b], Hannah Juan Han[a], Emma C. Kindall[c], Xiaofeng Guo[c], Dmitrii A. Kulik[d], George Dan Miron[d]

[a] New Mexico Bureau of Geology and Mineral Resources, New Mexico Institute of Mining and Technology, 801 Leroy Place, Socorro, NM 87801, USA

[b] Department of Earth and Environmental Science, New Mexico Institute of Mining and Technology, 801 Leroy Place, Socorro, NM 87801, USA

[c] Department of Chemistry, Washington State University, Pullman, WA 99164, USA

[d] Paul Scherrer Institute, Laboratory for Waste Management, Villigen PSI 5232, Switzerland

* Corresponding author: e-mail, alexander.gysi@nmt.edu

Tel: +1 575-835-5754

To be submitted to GCA, for the Special Issue "Hydrothermal Geochemistry and Beyond: A Tribute to Terry M. Seward"

REVISION 1

Keywords: rhabdophane; calorimetry; thermodynamics; Raman spectroscopy; X-ray diffraction

Abstract

Rhabdophane is a hydrous phosphate that commonly replaces monazite as a weathering product in critical mineral deposits during the alteration of rare earth elements (REE) bearing carbonatites and alkaline igneous complexes. It is an important host to the light (L)REE (i.e., La to Gd) but the stability and structure of binary solid solutions between the Ce and the other LREE endmembers have not yet been determined experimentally. Here we present room temperature calorimetric experiments that were used to measure the enthalpy of precipitation of rhabdophane ($Ce_{1-x}REE_xPO_4{\cdot}nH_2O$; REE= La, Pr, Nd, Sm, Eu, and Gd). The solids were characterized using X-ray diffraction, scanning electron microscopy, Raman spectroscopy, and the role of water in the rhabdophane structure was further determined using thermogravimetric analysis coupled with differential scanning calorimetry. The calorimetric experiments indicate a non-ideal behavior for all of the binary solid solutions investigated with an excess enthalpy of mixing (ΔH^{ex}) described by a 2- to 3-term Guggenheim parameters equation. The solid solutions were categorized into three groups: 1) binary Ce-La and Ce-Pr which display positive ΔH^{ex} values with a slight asymmetry; 2) binary Ce-Nd and Ce-Sm which display negative ΔH^{ex} values with a nearly symmetric shape; 3) Ce-Eu and Ce-Gd which display both negative and positive ΔH^{ex} values with nearly symmetric shape. The excess Gibbs energy (ΔG^{ex}) of the solid solutions was further investigated using a thermodynamic analysis approach of aqueous-solid solution equilibria and the optimization programs GEMS and GEMSFITS. The resulting ΔG^{ex} values combined with the calorimetric ΔH^{ex} values indicate that there is likely an excess entropy contribution implying important short-range structural modifications in the solid solutions dependent on the deviation of the REE ionic radii from the size of Ce^{3+}. These observations

corroborate with the trends in the Raman ν_1 stretching bands of the PO_4-site. The excess molar volumes determined from X-ray diffraction analysis further indicate an overall asymmetric behavior in all of the studied binary solid solutions, which becomes increasingly important from La to Gd. The pronounced short-range order-disorder occurring in groups 2 and 3 solid solutions mimics some of the behavior observed from previous studies in anhydrous monazite solid solutions. This study highlights the potential to use the chemistry and the structural modifications of rhabdophane as potential indicators of formation conditions in geologic systems and permits improving our modeling capabilities of REE partitioning in critical minerals systems.

1. INTRODUCTION

Monazite is the monoclinic (*$P2_1/n$*) anhydrous form of the REE phosphates and a major host to the light (L)REE in natural systems including La to Gd (Ni et al., 1995). Experimental studies have convincingly shown that the solubility of REE is however controlled by the mineral rhabdophane at temperatures below ~100 °C (Du Fou de Kerdaniel et al., 2007; Gausse et al., 2016; Ochiai and Utsunomiya, 2017; Arinicheva et al., 2018). The latter is a metastable hydrated REE phosphate ($REEPO_4 \cdot 0.667H_2O$) with a monoclinic (*C*2) structure (Mesbah et al., 2014; Rafiuddin and Grosvenor, 2016). Rhabdophane is commonly found as an alteration product of monazite associated to surface weathering of carbonatites, which can lead to important secondary REE enrichment such as in the Bear Lodge REE deposit (Andersen et al., 2016, 2017; Hutchinson et al., 2022). Low temperature fluid-mediated dissolution and re-precipitation processes have also important implications for resetting monazite ages (Berger et al., 2008; Williams et al., 2011; Seydoux-Guillaume et al., 2012). Furthermore, the low solubility of REE phosphates (e.g. Byrne and Kim, 1993; Gausse et al., 2016), makes them ideal solids for immobilizing actinides associated to radioactive wastes (Du Fou de Kerdaniel et al., 2007; Dacheux et al., 2013). A prerequisite to model the stability of these REE phosphates is however knowledge of their thermodynamic properties. Particularly, the REE phosphates form solid solutions in natural systems, which can potentially be linked to physicochemical conditions prevailing during their genesis in fluid-rock systems.

The solubility of both, monazite and rhabdophane, have been determined as a function of temperature for all of the endmembers (e.g. Poitrasson et al., 2004; Cetiner et al., 2005; Gausse et al., 2016; Gysi et al., 2018; Van Hoozen et al., 2020), and their thermodynamic properties have been determined using calorimetry including enthalpy, entropy, and heat capacity (e.g. Ushakov et al., 2001; Thiriet et al., 2004, 2005; Popa and Konings, 2006; Gavrichev et al., 2008, 2009, 2015, 2016; Shelyug et al., 2018). Only a few experimental studies have investigated the mixing and structural properties of monazite for binary solid solutions involving La, Nd, Eu, and Gd (e.g. Geisler et al., 2016; Hirsch et al., 2017; Neumeier et al., 2017; Huittinen et al., 2017; Schlenz et al., 2019), which generally exhibit a non-ideal solid solution behavior that tends to become more pronounced with increased differences ionic radii of the substituting REE. In contrast, the properties of rhabdophane solid solutions, particularly those involving the Ce endmembers, are still unknown. The latter are important because they control the mobility of the LREE in natural systems according to the common occurrences of Ce-rich rhabdophane (Andersen et al., 2017; Ichimura et al., 2020; Giovannini et al., 2021; Cook et al., 2023). An interesting observation made in the experimental study by Liu et al. (2022) is the apparent influence of the hydrated/non-hydrated sites of the rhabdophane structure on the incorporation of Nd^{3+} into rhabdophane-(Ce), which has not yet been explored extensively. Previous experimental work on rhabdophane solid solutions has been largely focused on the incorporation of actinides in the rhabdophane structure (Qin et al., 2017; Huittinen et al., 2018) and optical/microstructural and thermal properties of a few mixed rhabdophane compositions (Colomer et al., 2018; Liu et al., 2022). Therefore, there is need to determine the thermodynamic properties of solid solutions, particularly for the binary system involving the Ce-rich rhabdophane compositional endmember prevalent in natural systems.

In this study, room temperature calorimetric experiments are presented for the determination of the enthalpy of precipitation of the entire LREE binary rhabdophane solid solution series $(Ce_{1-X}REE_X)PO_4 \cdot nH_2O$ (REE = La, Pr, Nd, Sm, Eu, Gd). These experiments are used to explore the hypothesis that the rhabdophane solid solutions display a non-ideal solid solution controlled by the ionic radii of the REE, similar to the behavior of the anhydrous REE phosphates. The enthalpies of precipitation are use to retrieve the excess enthalpy mixing for these rhabdophane solid solutions and the precipitated solids were further characterized using powder X-ray diffraction, Raman spectroscopy, thermogravimetric analysis and differential scanning calorimetry. These methods allow determining the unit cell parameters of rhabdophane, their water contents, and their non-ideal solid solution behavior (i.e., excess volume of mixing and molecular vibrational properties). The experimental investigation was further complemented by a thermodynamic analysis using aqueous-solid solution equilibria modeling and thermodynamic parameter optimizations using GEMS and GEMSFITS (Kulik et al., 2013; Miron et al., 2015), for deriving the excess Gibbs energy of mixing. These combined approaches were used to derive a thermodynamic solid solution model of the full binary rhabdophane solid solution series.

2. METHODS

2.1. Materials

Two types of stock solutions were prepared for the rhabdophane precipitation experiments. Rare earth elements (i.e., La, Ce, Nd, Pr, Eu, and Gd) bearing stock solutions were prepared by dissolving solid REE nitrates (Alfa Aesar, 99.99 to 99.999 % purity) into Milli-Q water (18.2 MΩ·cm) to reach a concentration of ~250 mmol/kg REE. The phosphate-bearing solutions (~40 mmol/kg P) were prepared by dissolving solid $NH_4H_2PO_4$ (Acros Organics Chemicals, 99.999 %

purity, trace metal basis) into Milli-Q water. Blank solutions for sample dilutions and element analysis were prepared by adding nitric acid (Fisher Scientific, trace element grade) into Milli-Q water to reach a matrix concentration of 2% HNO_3. Stock solutions of 0.1 M hydrochloric acid (Inorganic Venture, NIST traceable) and TRIS powder (Sigma-Aldrich, 99.9 % purity) were used for standardizing the calorimeter.

2.2. Experimental methods

2.2.1. Reaction calorimetry

Calorimetric experiments were conducted at room temperature (20.0 ±1.0 °C) using a Parr 6755 reaction calorimeter equipped with a Parr 6772 high-precision thermometer. The calorimeter consists of a silver-lined Dewar flask, a glass reaction cell with a Teflon dish and a stirring and an opening mechanisms. This calorimetric method allows for mixing of two aqueous solutions brought close to thermal equilibrium and was adapted here based on the carbonate solid solutions precipitation study by Katsikopoulos et al. (2009). Here, the precipitation of REE phosphates was induced by mixing the REE-bearing nitrate with the phosphate-bearing stock solution according to the following reaction,

$$REE^{3+}\,(aq) + PO_4^{3-}\,(aq) + n H_2O\,(aq) \rightarrow REEPO_4 \cdot n H_2O\,(s) \quad (1)$$

The calorimeter was first standardized each day by dissolving 0.50 g of TRIS buffer into 100 g of 0.1 M HCl solution to determine its heat content. A typical REE phosphate precipitation experiment consists of first loading separately the glass cell with 2 g of the ~250 mmol/kg dissolved REE-bearing nitrate stock solution and loading of the Deware flask with 100 g of the ~40 mmol/kg phosphate-bearing stock solution. For endmember rhabdophane synthesis experiments, only a single REE nitrate solution (i.e., La, Ce, Nd, Pr, Eu, or Gd) was added to the cell; for binary solid solution synthesis experiments, the REE stock solutions of individual endmembers were added in varying mole fraction proportions in each experiment. The experimental run IDs indicate the mixing proportions of these starting solutions, which are also close to the measured compositions of the synthesized solids (Table 1).

At the beginning of an experiment, the calorimeter is first assembled and the closed glass cell is brought in thermal equilibrium for ~4 h with the solution in the Deware flask. After thermal equilibration, the cell is stirred and the calorimeter equilibrated for ~10 min before the glass cell is opened to allow mixing of the REE-bearing nitrate and the phosphate-bearing solutions which results in instantaneous precipitation of rhabdophane. The measured temperature difference and standardized heat content of the calorimeters are used to determine the enthalpy of precipitation (ΔH^{ppt}_{ss}) at room temperature; the mole amounts of precipitates are determined from the difference in REE concentrations measured in the starting REE stock solutions and the final REE concentrations of the reacted and filtered experimental solutions. Each experiment was carried out in duplicates to quadruplicates with the same endmember proportions to determine the experimental uncertainty. Solids were collected by filtration of the experimental solutions through a 0.45 μm membrane filter using a vacuum pump and then oven-dried overnight at ~60–75 °C. These low temperatures are used to avoid any significant dehydration of structural water, which was observed to occur above 100–250 °C (Shelyug et al., 2018). The dried solids were then stored in a desiccator before further characterization. The solution compositions were determined at the end of each experiment by filtering fluid aliquots through a 0.22 um filter followed by acidification with nitric acid, and if necessary, further dilution with a 2% HNO_3 blank solution.

2.2.2. Thermogravimetric analysis coupled with differential scanning calorimetry

Thermogravimetric analysis (TGA) and differential scanning calorimetry (DSC) were performed using a Setaram SetSYS calorimeter. The TGA-DSC was conducted from 28 to 700 °C with a heating rate of 5 °C/min under a flowing N_2 atmosphere of 20 mL/min. The temperature and sensitivity of the instrument were calibrated by heating repeatedly indium, tin, lead, zinc, and aluminum across their fusion point at the temperature change rates of 5, 10, 15, and 20 °C/min. The calibration and methodology which are detailed above is described in more detail in previous reports (Strzelecki et al., 2022a; Goncharov et al., 2022). The DSC data was fit to a spline interpolation baseline. For dehydration enthalpy calculations, integrations of DSC data were performed over the time ranging corresponding to 50–150 °C for the first dehydration and 150–300 °C for the second dehydration step. These temperature ranges are similar to previously established ranges for the two-step dehydration process for rhabdophane endmembers between 25 and 500 °C (Mesbah et al., 2014).

2.3. Analytical methods

The REE concentrations of the starting stock solutions and filtered experimental solutions were analyzed using an Agilent 5900 inductively coupled plasma optical emission spectrophotometer (ICP-OES) with axial viewing mode and an Agilent 7500 quadrupole ICP mass spectrometer

(ICP-MS), respectively, at the Analytical Geochemistry Laboratory in the New Mexico Bureau of Geology and Mineral Resources, New Mexico Institute of Mining and Technology. The ICP-MS is equipped with an in-line He collision cell to reduce REE oxide formation. Both, samples and standards were diluted and prepared using a 2% nitric acid (Fisher Scientific, trace metal grade) blank solution. The instrumental drift was monitored using an in-line internal indium standard spike (Inorganic Ventures, NIST traceable). External calibration standards were prepared using serial dilutions from a multi-element REE standard solution (Inorganic Ventures, NIST traceable, CMS-1, 10 ±0.04 ppm), with four to seven calibration points in a concentration range from 50 ppb to 5 ppm for ICP-OES measurements, and a concentration range from 0.01 to 50 ppb for ICP-MS analysis. The analytical precision of ICP-OES analysis based on repeated 50 ppb standard analysis is better than 2 % in the considered concentration range. The detection limits for REE measured using ICP-OES is 5 ppb based on 5σ (standard deviation of the mean) of multiple blank analyses. The analytical precision of REE standard analysis using ICP-MS analysis is better than 2 % based on repeated standard analysis of a 5 ppb REE check standards. The detection limits of ICP-MS analysis range is 5 ppt REE based on 5σ of multiple blank analyses with a limit of quantification of ~8 ppt based on 10σ of multiple blank analyses. The REE concentrations of the reacted experimental solutions range between 0.1 to 10 ppb with analytical precisions ranging between 1 to 3 % in this concentration range based repeated standard analysis.

Powder X-ray diffraction (XRD) analyses were conducted using a Panalytical X'Pert Pro diffractometer and Cu-Kα radiation with scanning 2θ angles ranging between 5 to 70° in 0.02° steps. Powdered samples were dry pressed and mounted on amorphous silica plates with randomly oriented crystals. The Rietveld refinement software MAUD (Lutterotti et al., 1999) was used for refining the unit cell parameters of rhabdophane endmembers and solid solutions. The initial crystal structure and lattice parameter of rhabdophane was adopted from the monoclinic *C*2 structure of rhabdophane-(Sm) determined by Mesbah et al. (2014). This allowed determining first the crystal lattice parameters for the endmembers synthesized in our study and also determine peak broadening (i.e., due to small crystallite sizes) and shifts in 2θ angles and other parameters before refining the lattice parameters of the binary solid solutions. An example of refined parameters for rhabdophane-(Sm) and more details about the method are given in the Supplementary Material.

The mole fraction REE in the rhabdophane precipitates was determined using an Hitachi S-3200N scanning electron microscope equipped with a Thermo Fisher Noran System 6 energy dispersive spectrometer (EDS). The samples were mounted on carbon tape and carbon coated. An acceleration voltage of 15.0 kV with a working distance of 15 mm was used perform EDS analysis. Several points across multiple grains were measured to detect any heterogeneity, and SEM images were inspected for morphology, crystallinity, and sizes of mineral aggregates.

Raman spectroscopy was performed on a Horiba LabRAM HR Evolution confocal microscope equipped with a 533 nm excitation Nd:YAG laser and a motorized XYZ stage. Analyses of the rhabdophane water peak were performed using a 50x LWD objective (NA =0.5; WD = 10.6 mm) and a 600 grooves/mm grating with a spectral resolution of 1.5 cm^{-1}. Spectra were collected at 10% laser power, 20 s exposition time and 5 accumulations. Analyses of vibrational phosphate stretching (v_1, v_3) bands were performed using a 1800 grooves/mm grating with a spectral resolution better than 0.5 cm^{-1}. Spectra were collected at 25% laser power, 100 s exposition time and 5 accumulations. The instrument was calibrated using a first-order Si line at 520.7 cm^{-1} (silicon wafer). The Raman spectra were de-convoluted using Fityk 1.3.1 (Wojdyr, 2010).

2.4. Experimental data treatment

The excess volume of mixing (ΔV^{ex}) was determined for each rhabdophane solid solution by measuring their unit cell parameters using powder XRD, and is derived according to:

$$\Delta V^{ex} = V_{ss} - V_{mm} \quad (2)$$

where V_{ss} is the molar volume (in cm^3/mol) of a binary solid solution and V_{mm} is the molar volume of an ideal mechanical mixture. The latter can be calculated from the molar volumes of the rhabdophane endmembers ($V_{rhabdophane}$),

$$\Delta V_{mm} = (1\text{-}x)\ V_{rhabdophane\text{-}(Ce)} + x\ V_{rhabdophane\text{-}(REE)} \quad (3)$$

where x is the mole fraction REE (La, Pr, Nd, Sm, Eu, and Gd) in the binary $(Ce_{1\text{-}X}REE_X)PO_4{\cdot}nH_2O$ rhabdophane solid solution.

The excess enthalpy of mixing (ΔH^{ex}) of the binary rhabdophane solid solutions were determined from calorimetric measurements according to:

$$\Delta H^{ex} = \Delta H^{ppt}{}_{ss} - \Delta H^{ppt}{}_{mm} \quad (4)$$

where ΔH^{ppt}_{ss} corresponds to the measured enthalpy of precipitation of the rhabdophane solid solution (i.e. using a mixture of two REE-bearing nitrate solutions in the calorimeter cell); ΔH^{ppt}_{mm} corresponds to the precipitation enthalpy of a mechanical mixture of pure rhabdophane endmembers (i.e. using a single REE-bearing nitrate solutions in the calorimeter cell). The latter can easily be determined for each mechanical mixture composition from the measured precipitation enthalpies of each rhabdophane endmember ($\Delta H^{ppt}_{rhabdophane}$),

$$\Delta H^{ppt}_{mm} = (1\text{-}x)\ \Delta H^{ppt}_{rhabdophane\text{-}(Ce)} + x\ \Delta H^{ppt}_{rhabdophane\text{-}(REE)} \qquad (5)$$

The method employed here is similar to the one presented by Katsikopoulos et al. (2009), which doesn't require determining the heat of dilution in order to derive the enthalpy of mixing from the calorimetric experiments. The heat of dilution is, within experimental uncertainty, the same in all of the experiments and can be considered negligible because: 1) the proportions of REE-bearing nitrate solutions (i.e., 2 ml in the cell) to phosphate-bearing stock solutions (i.e., 100 ml in the Deware flask) remain the same in all of the experiments; 2) the heat of dilution cancels out in the derivation of ΔH^{ex} according to Eq. 4, which however, necessitates measuring the $\Delta H^{ppt}_{rhabdophane}$ values for all of the rhabdophane endmembers of interest.

2.5. Thermodynamic modeling

2.5.1. Aqueous-solid solution equilibrium calculations

Aqueous speciation and activities of solid solution endmembers were determined in the experimental aqueous-solid solution (Aq−SS) system using the GEMS code package (Kulik et al., 2013) v. 3.9.6 and the MINES thermodynamic database (Gysi et al., 2023). The thermodynamic properties used include data for aqueous species from Supcrt92, slop98.dat (Shock and Helgeson, 1988; Haas et al., 1995; Shock et al., 1997), data for REE oxides and hydroxides (Diakonov et al., 1998; Konings et al., 2014; Navrotsky et al., 2015), monazite and xenotime (Gysi et al., 2015, 2018; Van Hoozen et al., 2020; Gysi and Harlov, 2021), which were augmented in this study with data for rhabdophane from the solubility study by Gausse et al. (2016) and the calorimetric, thermogravimetry, and XRD study by Shelyug et al. (2018). These datasets are summarized and reviewed in details in the study by Pan et al. (2024).

The Gibbs Energy Minimization approach (GEM) was used for thermodynamic calculations because it offers a straightforward way to solve Aq−SS equilibria from given input bulk chemical composition, pressure and temperature including for highly non-ideal solid solutions (Kulik, 2006; Kulik et al., 2010). Furthermore, the GEMS code package includes a process-path simulator with a graphical output option to construct Lippmann diagrams (Kulik et al., 2010). These diagrams were constructed in the present study to assess solutus and solidus curves (Prieto, 2009) for evaluating the Aq−SS equilibrium of the binary rhabdophane solid solutions precipitated in the experiments.

The TSolMod library (Wagner et al., 2012) implemented in the GEMS code package was used for all of the activity model calculations. The properties of H_2O were calculated from the IAPS-84 equation of state (Kestin et al., 1984). The activity of charged aqueous species was calculated using the extended Debye-Hückel equation (Robinson and Stokes, 1968) and activity coefficients for neutral species were set to unity. The solid solution activity model was chosen based on the best fits to the results from the calorimetric experiments. For a non-ideal subregular (asymmetric) solid solution model, the binary Redlich-Kister solid solution model can be used based on the Guggenheim function (Prieto, 2009), given by:

$$\Delta G^{ex} = RT\,x(1-x)[a_0+a_1(2x-1)+a_2(2x-1)^2] \quad (6)$$

where ΔG^{ex} is the excess Gibbs energy of mixing; a_0, a_1, and a_2 are the dimensionless Guggenheim coefficients or interaction parameters (derived from the experimental data in this study); *R is* the ideal gas constant; *T* the temperature in Kelvin. The activity coefficients (γ_i) for two endmembers (where i= 1 and 2, the index of each endmember) in a binary solid solutions are calculated according to:

$$\ln\gamma_1= x_2^2\,[a_0-a_1(3x_1-x_2)+a_2(x_1-x_2)(5x_1-x_2)] \quad (7)$$

$$\ln\gamma_2= x_1^2\,[a_0+a_1(3x_2-x_1)+a_2(x_2-x_1)(5x_2-x_1)] \quad (8)$$

2.5.2. Thermodynamic parameter optimizations

The standard molar Gibbs energies of formation from the elements ($\Delta_f G^\circ$) of rhabdophane endmembers and the binary solid solution interaction parameters were optimized at 25 °C and 1 bar using the GEMSFITS code (Miron et al., 2015). These optimizations are carried out using the composition of the experimental aqueous solutions (i.e., molality of dissolved elements) and the compositions of the rhabdophane solid solutions (i.e., mole fraction REE in the solid solution) precipitated in the calorimeter. The optimizations involve first calculation of chemical equilibrium in each system using the GEM approach, followed by optimization of the parameters ($\Delta_f G^{\circ}$ and a_0-a_2 in Eqs. 6-8) in order to match the calculated and measured compositions of the aqueous and solid solutions. The GEM approach for chemical equilibrium, aqueous speciation and solid solutions model calculations described above are implemented in the GEMS code package (Kulik et al., 2013) and the TSolMod library (Wagner et al., 2012), which are both also used in the program GEMSFITS (Miron et al., 2015). The starting values for the rhabdophane endmembers thermodynamic properties were taken from the solubility experiments by Gausse et al. (2016) and the interaction parameters derived in the present experimental study.

3. EXPERIMENTAL RESULTS

3.1. Powder XRD

3.1.1. Characterization of synthetic rhabdophane powder homogeneity and refined unit cell parameters

The synthetic rhabdophane endmembers and binary solid solutions all display relatively broad but distinct and systematic XRD peaks consistent with crystalline rhabdophane powders (Figs. 1-3). The broadness of these peaks is typical for solids synthesized at room temperature, which can result from compositional heterogeneity and small crystallite sizes (e.g. Katsikopoulos et al., 2009). Compositional variations measured in SEM-EDS multiple point analysis indicate 1σ values of the average with compositional variations of less than 1 % (Table 1), even in powders from separate replicate precipitation experiments with the same starting solutions. The size of the crystals are generally <1 μm and form 100s of nanometers in size aggregates with no discernible secondary REE phase observed in SEM imaging (Supplementary Material) or detected using XRD (Figs. 1-3). These observations indicate that the rhabdophane precipitates are homogeneous at the micron scale. Any heterogeneity (i.e. compositional or crystallinity/amorphous grain) is therefore likely minor and at the nanometer scale and difficult to characterize.

Figure 1 shows a comparison of the X-ray diffractograms between the different rhabdophane-(La) to -(Gd) endmembers. Major reflections are observed at Miller indices of (51-1) and (711) with a clear shift to higher 2θ angles with decreased ionic radius of the REE considered (i.e., 1.216 Å for La and 1.107 Å for Gd in 9-fold coordination; Shannon, 1976). The lattice parameters of the synthetic rhabdophane endmembers were refined using the monoclinic (*C*2) structure (Mesbah et al., 2014; Rafiuddin and Grosvenor, 2016; Shelyug et al., 2018). Figure 2 shows that the *a*, *b*, and *c* crystal lattice parameters all display a clear linear relationship with increased ionic radius of the REE. Comparison with the rhabdophane crystal lattice parameters refined in the studies by Mesbah et al. (2014), Ochiai and Utsunomiya (2017), and Shelyug et al. (2018) indicates an overall good agreement with our data. The refined *a*-axis matches these studies well, whereas the refined *b*- and *c*-axes are slightly lower or higher by ~0.10−0.20 Å in our study, respectively. The best fit to all diffractograms could only be achieved with these lattice parameters to yield reasonable refined β angles ranging between 115.5° to 115.9° for both the refined endmembers and the solid solutions (Table 1). Using these refined lattice parameters, the calculated unit cell volumes (V_{cell}) indicate a systematic and linear increase with increased ionic radii of the REE (Fig. 2d). Rhabdophane endmembers with larger ionic radii (i.e., La, Ce, Pr, and Nd) display refined V_{cell} values that are distinctly smaller in comparison to unit cell volumes determined in other studies (Mesbah et al., 2014; Ochiai and Utsunomiya, 2017; Shelyug et al., 2018). In contrast, refined V_{cell} values of rhabdophane endmembers with smaller ionic radii (i.e., Sm, Eu, and Gd) closely match these other studies.

A possible explanation for the observed differences could be the effects of experimental crystal growth conditions (i.e., pH, solution saturation, equilibration time, temperature, etc.) which can potentially affect the crystallinity, crystallite sizes, structure, and the water contents of these hydrated REE phosphates (Ochiai and Utsunomiya, 2017; Liu et al., 2022). The homogeneity of the solid solutions can be further verified using the Full Half Width Maxima (FHWM) or XRD peak broadness of the solid solutions which should lie within those of their endmember compositions (Katsikopoulos et al., 2009). The fitted peak shifts and FHWM of the main XRD reflections (Figs. 1 and 3) for Ce-Nd and Ce-Gd rhabdophane indicate systematic and close to linear trends between solid solutions and endmembers (Supplementary Material). These trends are interpreted to indicate a lack of major chemical or structural heterogeneity in the synthesized powders. The relatively broad peaks and FHWM generally between 1.0−1.6, indicates very small crystallite sizes, and result from the poor crystallinity of the solids synthesized at ambient conditions. The measured XRD peak positions are comparable but display broader peaks in comparison to rhabdophane synthesized at high temperature and crystallized for several days by Liu et al. (2022); their study reports crystal sizes of over 200 nm using transmission electron microscopy. Surface properties are however unlikely to control the trends observed for the retrieved lattice parameters. Particularly, because these surface effects result in more significant XRD peak loss and become important for crystallite sizes of less than 10 nm which are usually accompanied by excess water adsorbed on the surface (Majzlan et al., 2003; Mazeina and Navrotsky, 2005). The Raman and TGA/DSC data presented further below indicate that water is structural in the synthesized rhabdophane in our study. Therefore, both the trends observed in the refined diffractograms (Fig. 1) and refined unit cell parameters (Fig. 2) suggest that the solids synthesized in our calorimetric experiments are homogeneous and large enough to further evaluate the systematics of their solid solutions.

X-ray diffractograms for the Ce-Nd and Ce-Gd binary rhabdophane solid solutions precipitated in the calorimetry experiments are shown in Figure 3. The diffractograms for Ce-Nd indicate a slight shift in 2θ angles with addition of Nd in the solid solution for reflections on the Miller indices (51-1), (-222), and (711) (Fig. 3a). The solid solutions with mole fraction compositions close to the Ce endmember (x_{Nd} = 0.10, 0.25, and 0.35) display a slight shift to lower 2θ angles, whereas the intermediate solid solution (x_{Nd} = 0.65) is close to the Ce endmember and the solid solutions closer to the Nd endmember (x_{Nd} = 0.75 and 0.90) are shifted to slightly higher 2θ angles. The diffractograms for the Ce-Gd solid solution (Fig. 3b) display a similar but more pronounced shift in 2θ angles with a shift to lower angles for solid solution compositions closer to the rhabdophane-(Ce) endmember (x_{Gd} = 0.10, 0. 25, and 0.35), and a shift to higher angles for solid solution compositions closer to the rhabdophane-(Gd) endmember (x_{Gd} = 0.65, 0. 75, and 0.90).

3.1.2. Molar volume (V_{ss}) and excess volume of mixing (ΔV^{ex}) of binary solid solutions

The trends in the X-ray diffractograms presented above are also in line with the molar volumes of the solid solutions and their excess volumes of mixing (Figs. 4 and 5). This is illustrated by the systematic increase in asymmetry with increased differences in ionic radii between Ce and the other REE in the solid solution. The V_{ss} values determined from the refined crystal unit cell parameters (Table 1) deviate from the ideal mixing line for almost all binary rhabdophane solid solutions except the Ce-Pr solid solution series which plots closest to this line (Fig. 4). This indicates that the solid solutions display generally a non-ideal volume of mixing, which was further quantified according to Eqs. 2 and 3 using the refined unit cell volumes in Table 1.

Figure 5 shows the excess volume of mixing as a function of mole fraction REE in the solid solution. All the binary solid solutions display positive ΔV^{ex} values up to ~0.4–0.7 $cm^3 \cdot mol^{-1}$. The solid solutions showing closest behavior to a symmetric excess volume of mixing are the Ce-La, Ce-Pr, and Ce-Nd binaries, whereas the solid solutions with larger differences in ionic radii including Ce-Sm, Ce-Eu, and Ce-Gd display larger asymmetries. The ΔV^{ex} values of binary rhabdophane solid solutions were fitted using a Guggenheim function according to:

$$\Delta V^{ex} = \mathrm{R}T\,x(1\text{-}x)[a_0+a_1(2x\text{-}1)+a_2(2x\text{-}1)^2] \qquad (9)$$

where x is the mole fraction REE in the binary Ce-REE rhabdophane solid solution; a_0, a_1, and a_2 are the Guggenheim coefficients; R *is* the ideal gas constant; T the temperature in Kelvin. Several different models were tested including a regular model (where a_1 and a_2 = 0), and subregular asymmetric models with two and three coefficients. Table 2 summarizes all of the fitted coefficients and the corresponding R^2 values for each fit. Figure 5 shows that the best fit to the experimental data was achieved using the subregular 3-coefficients Guggenheim model with R^2 values of 0.94–0.99 for the Ce-La, Ce-Pr, and Ce-Nd solid solutions and lower R^2 values of 0.86–0.87 for the Ce-Sm, Ce-Eu, and Ce-Gd solid solutions. Using more than three coefficients resulted in unrealistic curve shapes indicating over fitting of the data. Therefore, we recommend the fitted values from the subregular 3-coefficients Guggenheim model in Table 2 for modeling the ΔV^{ex} of binary rhabdophane solid solutions. The shapes of the peaks observed in a ΔV^{ex} vs. x_{REE} diagram (Fig. 5) indicate that the REE with ionic radius closest to Ce (i.e., La, Pr and Nd) form solid solutions closest to a regular solid solution with slight asymmetry. The latter becomes more pronounced in solid solutions where Ce is substituted with REE of decreasing ionic radius (i.e., Sm, Eu, and Gd).

3.2. Reaction calorimetry

3.2.1. Precipitation of REE

The amount of rhabdophane precipitated in each solution calorimetric experiments was calculated based on the measured REE concentrations in the stock solutions and the quenched experimental solutions after rhabdophane precipitation (Table 3). Figure 6 shows a systematic linear relationship between the amount of REE precipitated vs. x_{REE} and also a dependence on the ion size difference between Ce and the substituting REE. The only solid solutions showing a slight positive slope is the Ce-La rhabdophane solid solution (Fig. 6a). The precipitation behavior between Ce-Pr and Ce-Nd rhabdophane solid solutions is almost similar with a small decrease (~0.05−0.04 mmol) in REE precipitated with increased amounts of the substituting REE (Fig. 6b-c). In contrast, the amount of precipitated rhabdophane decreases more significantly (by ~0.8 mmol) for the Ce-Sm, Ce-Eu, and Ce-Gd solid solutions with increased amounts of the substituting REE (Fig. 6d-f).

3.2.2. Excess enthalpy of mixing (ΔH^{ex})

The measured enthalpies of precipitation are listed in Table 3 and show average uncertainties of 0.5 kJ/mol based on replicate experiments. The excess enthalpy of mixing was calculated from the enthalpy of precipitation according to Eqs. 4 and 5 and using the experimental data listed in Table 3. Figure 7 shows that the experimental data for the Ce-La and Ce-Pr rhabdophane solid solutions display both positive ΔH^{ex} values of up to ~2 kJ/mol. In contrast, the experimental data for the Ce-Nd and Ce-Sm rhabdophane solid solutions display negative ΔH^{ex} values of ~1−2 kJ/mol. The experimental data for the Ce-Eu and Ce-Gd rhabdophane solid solutions both display an asymmetry with small negative ΔH^{ex} values close to the endmember compositions and positive ΔH^{ex} values for intermediate compositions. The ΔH^{ex} values for all of these binary rhabdophane solid solutions were fitted using a Guggenheim function according to:

$$\Delta H^{ex} = \mathrm{R}T\,x(1\text{-}x)[a_0+a_1(2x\text{-}1)+a_2(2x\text{-}1)^2] \qquad (10)$$

where x is the mole fraction REE in the binary Ce-REE rhabdophane solid solution; a_0, a_1, and a_2 are the dimensionless Guggenheim coefficients; R *is* the ideal gas constant; T the temperature in Kelvin. Similar to the fits for the molar volume, several different models were tested including a regular model (where a_1 and a_2 = 0) and asymmetric models with 2- (i.e., subregular) and 3-coefficients, respectively. Table 4 summarizes all the fitted coefficients and the corresponding R^2 of the fits. The best fit to the experimental data for rhabdophane with larger REE was a subregular 2-coefficients model with R^2 values of 0.45−0.82 for Ce-La and Ce-Pr solid solutions (Fig. 7a-b). For the rhabdophane solid solutions with smaller REE, the best fit to the experimental data was a subregular 3-coefficients Guggenheim model with R^2 values of 0.40−0.75 for the Ce-Nd, Ce-Sm, Ce-Eu and Ce-Gd solid solutions (Fig. 7c-f). Using more than 3 coefficients resulted in unrealistic curve shapes for the Ce-La and Ce-Pr binary due to data over fitting. Therefore, we recommend using the subregular 2-coefficients model for the Ce-La and Ce-Pr binary solid solutions, and the subregular 3-coefficients model for the other solid solutions for calculating their excess enthalpy of mixing from Table 4.

3.3. TGA-DSC analysis

The weight loss and enthalpies for the first (ΔH_{dehy1}) and second (ΔH_{dehy2}) steps of the dehydration process are given in Table 5. The combined enthalpy values for the whole dehydration process sum to higher values than demonstrated in previous work (Shelyug et al., 2018). Previous work established a trend of increasing dehydration temperature with ionic radius (Shelyug et al., 2018), which can also be observed in the TG data for the Ce-Nd and Ce-Gd series shown in Figure 8; the temperature associated with each dehydration step decreased with increased Ce content of the solid solution. The TG-DSC data for the Ce-Gd series are shown in Figure 8b. The water contents for Ce-Nd and Ce-Gd series are both ~1 mol H_2O (Table 5), which are consistent with previous studies where water contents were reported to range from 0.5 to ~2 mol H_2O (Anfimova, et al. 2014; Ochiai and Utsunomiya, 2017; Shelyug et al., 2018). Due to the low temperature condition for rhabdophane crystallization, additional water seen in some of the other studies may relate to the formation of amorphous phases that are usually hydrated (or hydroxylated) but not detected via XRD analysis.

3.4. Raman spectroscopy

Measured Raman spectra show that the peak center of the symmetric stretching vibrational band of the phosphate tetrahedron (ν_1-PO_4) is shifted from 970.1 cm^{-1} in monazite-(Ce) to 977.2 cm^{-1} in rhabdophane-(Ce) and that the asymmetric stretching vibration (ν_3-PO_4) shifts from 1055 cm^{-1} to 1085 cm^{-1}, respectively (Fig. 9a; Table 6). For reference 970 cm^{-1} was measured in Silva et al. (2006) and 972 cm^{-1} in Errandonea et al. (2018) for monazite-(Ce), respectively. Peaks are considerably broader in rhabdophane and ν_1-PO_4 is de-convoluted by three overlapping subpeaks, whereas in monazite the peaks are narrow and can be de-convoluted by only one peak. The ν_1-PO_4 subpeaks at higher wavenumbers in rhabdophane increase linearly with decreasing ionic radii in endmembers (Fig. 9b) and solid solutions and range from 977.2 cm^{-1} for the Ce to 992.4 cm^{-1} for Gd endmembers (Fig.10). This shift is related to the changes in vibrational energies of the PO_4 tetrahedron due to decreasing ionic radius and higher atomic number in the Gd endmember compared to lighter REE such as La and Ce. The rhabdophane-(Ce), -(Nd) and -(Gd) endmembers (Clavier et al, 2018; Liu et al., 2022) were previously measured using Raman spectroscopy showing a peak position of the main ν_1-PO_4 peak overlapping with the linear trends and endmembers in this study (Fig. 9b).

The full width at half maximum (FWHM) of the ν_1-PO_4 peak shows a considerable broadening from rhabdophane-(Ce) at 5.73 cm^{-1} to rhabdophane-(Nd) and -(Eu) at 10.70 cm^{-1} and 10.60 cm^{-1} and to rhabdophane-(Gd) at 8.32 cm^{-1} (Table 6; Fig. 10). An excess peak broadening (Δ_{FWHM}) was calculated to assess the relative departure of the FWHM values of the solid solutions from a linear interpolation between FWHM values of the endmembers (Fig. 10). The Δ_{FWHM} values of the Ce-Pr solid solutions remain roughly constant at 5.45 ±0.18 cm^{-1}

showing minimal deviations from the linear trend between the two endmembers (Fig. 10b). In contrast, the Δ_{FWHM} values of the Ce-Nd solid solutions start displaying minor positive deviation from a linear fit close to the endmembers and a negative deviation at mole fraction x_{Nd} of ~0.5 for the intermediate solid solution compositions (Fig. 10d). The Ce-Eu and Ce-Gd solid solutions show large positive Δ_{FWHM} values, indicating departure from an ideal solid solution, and display peak asymmetries occurring close to the Ce-rich rhabdophane compositional endmember (Fig. 10f, h).

The vibrational stretching bands for water in rhabdophane endmembers show the typical range from 2800 to 3700 cm^{-1} (Fig. 9c). The normalized water peak intensities are similar for rhabdophane-(La) and -(Ce), with a slight decrease in peak intensities for the rhabdophane-(Pr) and stronger decrease in peak intensities for the rhabdophane-(Nd) and -(Gd) endmembers. This trend corroborates with the lower water contents measured in rhabdophane containing the REE with smaller ionic radius as confirmed by TGA-DSC analysis (i.e., Ce, Nd>Gd; Table 5). Raman spectra for rhabdophane-(Nd), -(Sm), -(Eu) and -(Gd) endmembers are affected by fluorescence (Fig. 9c). The Raman band for water can be fitted by three subpeaks corresponding to network water (~3280 cm^{-1}), intermediate (~3460 cm^{-1}) and strong OH bonds (~3580 cm^{-1}) (Kolesov, 2006; Sun, 2009; Knight et al. 2019). The Raman water bands measured by Clavier et al. (2018) for rhabdophane-(Gd) agrees with our study with peaks observed at 3330, 3470 and 3540 cm^{-1}, showing a prominent intermediate peak (peak 2) and a minor network water (peak 1). The Raman water subpeak area percent for network water (ν_1-H_2O peak 1) systematically decreases from 75 to 40 % and for intermediate water ν_1-H_2O peak 2) increases from 19 to 45 % with decreasing ionic radii of the REE (Fig. 9d). This trend indicates that water molecules become more constrained (Knight et al., 2018) due to the smaller unit cell volumes from La to Gd, which we interpret to represent structural water as opposed to adsorbed water on the surface.

4. DISCUSSION AND THERMODYNAMIC DATA EVALUATION

4.1. Derivation of ΔG^{ex} from calorimetry data

4.1.1. Assumption of random mixing and distinction of different solid solution groups

As a first approximation we assume that the rhabdophane solid solutions are controlled by random mixing with the absence of any non-configurational entropy contributions. Their excess entropy (ΔS^{ex}) is then equal to zero and the excess Gibbs energy (ΔG^{ex}) is equal to the excess enthalpy. This assumption permits making use of the interaction coefficients derived from the fitted ΔH^{ex} values from the experimental data (Eq. 10, Table 4) to derive the ΔG^{ex} values of each solid solution. The Gibbs energy of mixing (ΔG^{mix}) can then be derived according to the relation:

$$\Delta G^{ex} = \Delta G^{mix} - \Delta G^{mix,\ ideal} \quad (11)$$

where $\Delta G^{mix,ideal}$ represents the ideal Gibbs energy of mixing, which is calculated from the configurational entropy ($\Delta S^{mix,\ ideal}$),

$$\Delta G^{mix,\ ideal} = -T\Delta S^{mix,ideal} = \mathrm{R}T(x_1 \ln x_1 + x_2 \ln x_2) \quad (12)$$

where R is the ideal gas constant; T is the temperature in Kelvin; x_1 and x_2 are the mole fractions of each endmember in a binary solid solution series. As shown in Figure 11a-b, the data can be subdivided into three groups: 1) solid solutions with ΔG^{ex} values >0 across the compositional range, resulting in ΔG^{mix} <0 for compositions close to the Ce endmembers, and ΔG^{mix} >0 for intermediate compositions (if $\Delta G^{ex}+\Delta G^{mix,ideal} > 0$); 2) solid solutions with ΔG^{ex} values <0 resulting in ΔG^{mix} <0 across the entire compositional range; 3) solid solutions with ΔG^{ex} values <0 close the endmember compositions and values >0 for intermediate compositions, resulting in ΔG^{mix} <0 across the entire compositional range with two minima close to the endmember compositions.

Group 1 solid solutions include the Ce-La and Ce-Pr binary rhabdophane solid solutions with a slight asymmetry and lower ΔG^{mix} towards the Ce endmember. This is in line with ΔH^{ex} values >0 (Fig. 7) indicative of a slight tendency towards unmixing with an asymmetric miscibility gap displaying two binodal minima defined at x_{REE} of ~0.15−0.35 and x_{REE} of ~0.95−0.98 (Fig. 11b). This should result in the formation of a Ce-rich binary solid solution phase and a phase close to rhabdophane-(La) and -(Pr) endmember compositions. The behavior of these solid solutions and the observed wide miscibility gap are somewhat similar as observed in the study by Katsikopoulos et al. (2009) for the calcite-kutnahorite solid solution series. The observed miscibility gap was called "metastable" due to assumption that the phase behavior observed in their experiments (i.e., synthesis of complete solid solution series and ΔH^{ex} values >0) is due to random ordering. However, the Mn endmember also exists as an ordered endmember with the potential of ordering and unmixing effects (Katsikopoulos et al., 2009). Similarly, in our experiments the observed complete solid solution series in the precipitation experiments are indicative of possible metastable conditions at room temperature, in which, unmixing and/or ordering could both be inhibited for these solid solutions due to instantaneous precipitation of disordered rhabdophane solid solutions at supersaturation. Typically, such solid solutions are controlled by the size of the substituting ion which creates a larger strain on the crystallographic site the larger deviation from the ideal ionic size. Mesbah et al. (2014) suggests that the monoclinic rhabdophane-(Sm) endmember has Sm^{3+} occurring 1/3 in the 8-fold coordination and 2/3 in the 9-fold coordination. This is in line with the average ionic size of La^{3+} of 1.183 Å (1.116 Å in 8-fold and 1.216 Å in 9-fold) being closer to the average ionic radius of Ce^{3+} of 1.178 Å (1.143 Å in 8-fold and 1.196 Å in 9-fold) in comparison to Pr^{3+} with an average ionic size of 1.161 Å (1.126 in 8-fold and 1.179 Å in 9-fold). This results in smaller excess Gibbs energy for the Ce-La binary over the Ce-Pr binary solid solution. The lower ΔG^{mix} values for the Ce-La binary rhabdophane solid solution therefore indicates a lower strain and larger compositional field where the solid solution composition is more stable than an equivalent mechanical mixture of the endmembers.

Group 2 includes the Ce-Sm and Ce-Nd binary rhabdophane solid solutions. In contrast to group 1, these solid solutions display negative ΔH^{ex} values (Fig. 7), which indicates the possible ordering in the structure of these rhabdophane solid solutions. Hence, ΔG^{ex} may be expected to differ from ΔH^{ex} (i.e., $\Delta S^{ex}\neq 0$), in which randomness cannot be assumed perfect (Prieto, 2009). The observed negative ΔG^{mix} values in the entire compositional range of these solid solutions (Fig. 11b) and the almost symmetric shape of the Ce-Sm binary indicates a lack of miscibility gap. In contrast, the binary Ce-Nd solid solutions display a slight convex upward trend for intermediate compositions. The latter indicate the possible presence of order-disorder effects for x_{REE} values between ~0.2 and 0.8. Particularly, the ΔH^{ex} function curve (and also ΔG^{ex}, see further below) is flattened in the middle of the composition interval which indicates the presence of short-range ordering (SRO), i.e. a tendency to form nm-sized local clusters (Vinograd and Winkler, 2010).

Group 3 solid solutions include Ce-Eu and Ce-Gd binary rhabdophane solid solutions, which are both likely to display stronger SRO effects than group 2 solid solutions. The latter is due to the larger differences in ionic radii of the substituting REE and possibly due to the water contents and molecule types incorporated into the rhabdophane structure. These observations corroborate with the observed ΔV^{ex} values from XRD (Fig. 5) displaying an asymmetry and the FHWM of the $v1$ Raman spectra (Fig. 10) indicating an increase in asymmetry of the phosphate bond stretching modes when comparing Pr and Nd with the Eu and Gd binary solid solution series. The ΔG^{mix} values of group 3 solid solution series display two minima defined at x_{REE} of ~0.15−0.2 and ~0.85−0.9 that can be caused by SRO effects with a relatively strong lattice strain elevating the ΔH^{ex} function up at intermediate compositions (Fig. 7e,f).

In summary, the observations above indicate groups 2 and 3 rhabdophane solid solutions have a non-negligible excess entropy contribution due to SRO effects, whereas group 1 indicates negligible SRO effects and only a slight tendency for unmixing. Further inspecting the trends derived from water chemistry (Fig. 6), reveals that there is no observable anomaly in the amount of solid solution precipitated as a function of solid solution composition for any of the binary solid solutions studied. This indicates that unmixing of two phases in the experimental run products are unlikely to occur, which corroborates with the sharp XRD peak shifts (Fig. 3) and the systematic Raman spectra observed in these solid solutions (Figs. 9 and 10).

4.1.2. Estimation of excess entropy (ΔS^{ex}) from XRD molar volume data

The excess Gibbs energy of rhabdophane solid solutions can be further evaluated assuming that ΔS^{ex} is not equal to zero and therefore including possible order-disorder effects in the solid solutions. The excess Gibbs energy can then be calculated from the calorimetric ΔH^{ex} data (Table 3) and ΔS^{ex} according to:

$$\Delta G^{ex} = \Delta H^{ex} - T\Delta S^{ex} \quad (13)$$

where ΔS^{ex} can be retrieved from knowledge of the entropy of mixing (ΔS^{mix}) and the ideal entropy of mixing ($\Delta S^{mix,ideal}$, i.e. configurational entropy, assuming total disorder and random mixing in the structure),

$$\Delta S^{ex} = \Delta S^{mix} - \Delta S^{mix,ideal} \quad (14)$$

Here the configurational entropy term ($\Delta S^{mix,ideal}$) was calculated based on the Boltzmann equation and the excess entropy of mixing, attributed from the vibrational entropy term ($\Delta S^{mix,vib}$), can be estimated based on an empirical relation between the standard absolute entropy (S^{o}_{298K}) and molar volume (V_m) of a compound (Jenkins and Glasser, 2003; Glasser, 2011; Strzelecki et al., 2022a). Typically, these equations are used to calculate S^{o}_{298K} for minerals (Guo et al., 2016; Strzelecki et al., 2020, 2022b; Goncharov et al., 2022). A revised linear equation was presented by Strzelecki et al. (2022a) for phosphate minerals based on the approach presented by Jenkins and Glasser (2003): $S^{o}_{298\,K} = k\cdot(V_m) + c$, where coefficient k is 2.46 ±0.03 $J\cdot mol^{-1}\cdot K^{-1}$ and c is 5.79 ±7.03 $J\cdot mol^{-1}\cdot K^{-1}$, and V_m ($cm^3\cdot mol^{-1}$) is derived from the XRD data in the present study

(Table 1). The obtained $\Delta S^{mix,vib}$ values (Table S1) reflect the change in the vibrational entropy based on the volumetric change of the unit cell, which is expected to be small, ranging from 0.1 to 1.7 ±2.4 $J \cdot mol^{-1} \cdot K^{-1}$ (Fig. 12a). Using this approach, the calculated $\Delta S^{mix,ideal}$ dominates the total entropy of mixing ΔS^{mix} contributing 2.3 to 5.8 $J \cdot mol^{-1} \cdot K^{-1}$ (Fig. 12b).

A comparison of ΔG^{ex} values derived in Figures 11a-b and Figure 11c-d shows the effect of using the excess entropy derived above. The excess entropy results in an overall decrease in calculated ΔG^{ex} values and thus more negative calculated ΔG^{mix} values. Nevertheless, the trends observed for the three different solid solution groups distinguished above remain similar.

4.2. Aqueous solution-solid solution (Aq-SS) equilibria calculations

4.2.1. Derivation of ΔG^{ex} from GEMSFITS optimizations and fitting of solid solution interaction parameters

In contrast to the two other approaches presented in section 4.1., the calculated ΔG^{ex} and ΔG^{mix} values based on solubility calculations and GEMSFITS optimizations display much smaller deviations from ideal mixing and only a slight asymmetry (Fig. 11e-f). The latter is more pronounced in group 2 (Ce-Nd and Ce-Sm binary) and group 3 (Ce-Eu and Ce-Gd binary) solid solutions with ΔG^{ex} values close to 0 (i.e., close to an equivalent mechanical mixture) and ΔG^{mix} values displaying a symmetric shape for the Ce-La and Ce-Sm binary and a slight asymmetry at x_{REE} values of 0.6–0.7 for all of the other binary solid solutions (Fig. 11f). The optimized interaction parameters for the excess Gibbs energy of each binary solid solutions (a_0-a_2 based on Eqs. 6-8) and the optimized standard Gibbs energy of formation ($\Delta_f G^o$) derived for each endmembers are listed in Table 7.

The calculated negative ΔG^{mix} values (Fig. 11f) suggest stabilization across the entire binary compositional range, whereas the lack of minima suggests a lack of unmixing/immiscibility. These results are in line with the observed near stoichiometric composition of the synthesized solid solutions with respect to the initial REE compositions added to the experimental solutions (Table 3). The difference between the ΔG^{mix} values calculated from the Aq-SS approach (Fig. 11f) versus the two other approaches (Fig. 11b,d) further indicates that the excess enthalpy derived from calorimetry is not the only contribution to the excess Gibbs energy. Therefore, the shapes of the ΔG^{ex} and ΔG^{mix} curves derived from the Aq-SS approach must likely be compensated by non-ideal entropy contributions (ΔS^{ex} and ΔS^{mix}). The latter were calculated by combining the optimized ΔG^{ex} values from Table 7 with the measured calorimetric ΔH^{ex} values from Table 4 according to Eqs. 13 and 14.

Figure 12 shows that the resulting excess entropy contributions are indeed quite larger for the Aq-SS approach versus those derived from a simple linear correlation based on XRD volumetric data. The entropy of mixing values are generally all positive and display an almost symmetric shape for both approaches. However, the ΔS^{mix} derived from the Aq-SS approach yields more information due to the higher ΔS^{ex} contribution vs. the configurational entropy resulting in a corresponding separation into the three solid solution groups (Fig. 12c,d). The lowest ΔS^{mix} values determined from the Aq-SS equilibria approach are found for the Ce-La and Ce-Pr binaries (group 1) with slight asymmetric peak shapes. The Ce-Nd and Ce-Sm binaries (group 2) display a positive symmetric shape, with the Ce-Nd binary starting to show a slight convex downward inflection. The latter becomes more pronounced for the Ce-Eu and Ce-Gd binaries (group 3) both displaying a minimum at a x_{REE} composition of ~0.55 indicating SRO effects for this solid solution group. These SRO effects are consistent with the measured Raman ν_1-PO_4 stretching bands for group 3 solid solutions with FWHM values departing from ideal behavior (Fig. 10f,h). A similar SRO effect is described in Vinograd and Winkler (2010) and in Kulik et al. (2010) based on atomistic simulations for the excess enthalpy and entropy of different types of solid solutions, which display such a convex depression controlled by local ordering with decreased temperature.

In conclusion, the optimized ΔG^{ex} values derived from the Aq-SS approach (Fig. 11e) result in calculated non-ideal entropy contribution that support the measured calorimetric excess enthalpy of mixing (Fig. 7) and the three groups distinguished for the rhabdophane solid solutions presented in this study. Therefore, the ΔG^{ex} values calculated from Table 7 are recommended to simulate the stability and compositions of these rhabdophane solid solutions, together with the calorimetric data derived in this study (Table 4). Particularly, because the resulting ΔG^{mix} values (Fig. 11f) result in the stabilization across each of the binary solid solution series corroborating with the measured compositions of the synthesized solid solutions in the experiments (Table 3).

4.2.2. Lippmann solubility diagrams

Lippmann diagrams are useful to further interpret the partitioning behavior of two elements (cations or anions) A and B in (A,B)C series between an aqueous solution and a binary solid solution, and determine potential miscibility gaps, departure from stoichiometric saturation, etc. In the binary rhabdophane solid solution system, the classic Lippmann total solubility product (e.g. Prieto, 2009) is described by:

$$\sum\Pi = \{PO_4^{3-}\}(\{REE^{3+}\}+\{Ce^{3+}\}) \quad (15)$$

where the braces indicate the ion activities in aqueous solution; for the pure endmembers, this represents the equilibrium solubility product. The variation of log∑Π values are plotted as an ordinate simultaneously against an abscissa of the solid solution mole fraction x_{REE} ("solidus" curve) and against an abscissa of the aqueous ion activity mole fraction $x_{REE}{}^{3+}$ ("solutus" curve),

$$x_{REE}{}^{3+} = \{REE^{3+}\}/(\{REE^{3+}\}+\{Ce^{3+}\}) \quad (16)$$

A horizontal line crossing the solidus and the solutus defines the composition of a solid solution in equilibrium with an aqueous solution. A large difference in composition between solidus and solutus points corresponds to a strong partitioning of an ion between a solid and an aqueous phase. The advantage of the ion-activity Lippmann solubility product is that it permits also to inspect the solubility product K^{o}_{SP} for the end member compositions. However, such ∑Π diagram has a drawback because it requires first to convert the measured total dissolved concentrations of REE and P into ion activities, which needs aqueous speciation equilibria calculations for each experimental system. A more convenient way to illustrate the solutus curve consists of using the total aqueous element concentration [] (molality or molarity) scale, which is expressed as a total dissolved element (TE) scale solutus curve:

$$\log_{10}\sum\Pi_{TE} = \log_{10}[P] - \log_{10}([REE]+[Ce]) \quad (17)$$

$$x_{REE,TEaq} = [REE]/([REE]+[Ce]) \quad (18)$$

Such Lippmann diagrams are directly computable in GEMS (Kulik et al., 2010) and retain the overall shape and topology of the classic Lippmann diagrams which are just shifted up along the ordinate axis. The experimentally measured solubility data in co-existing aqueous and solid solutions can then directly be plotted over the modeled curves (Fig. 13).

Figure 13 shows the Lippmann diagrams constructed using the optimized solid solution interaction parameters from the Aq-SS equilibria calculations. Comparison between the computed solutus curves and the experimental aqueous solution REE compositions indicates that the experimental data are reproduced fairly well from the optimized parameters listed in Table 7. However, the relative y-axis position of the calculated solidus/solutus curves strongly depends on: 1) the retrieved standard Gibbs energy of formation of the endmembers; and 2) the uncertainties of the solubility data. The average optimized ΔfG value for rhabdophane-(Ce) is -2,002 with a standard deviation of ±1 kJ/mol (Table 7). While this uncertainty is relatively small, it is capable of slightly shifting the computed solutus and solidus curves relative to the experimental data on the y-axis. This explains some of the observed discrepancies between the the computed curves (e.g. Ce-Pr and Ce-Nd binaries) and the experimental data which are difficult to resolve because all of the solid solutions include the rhabdophane-(Ce) compositional endmember. The optimized ΔfG values of rhabdophane endmembers in Table 7 indicate a systematic increase by 8 to 15 kJ/mol in comparison to the initial values derived from the solubility experiments by Gausse et al. (2016). For comparison, the reported uncertainties by Gausse et al. (2016) are quite large for Gibbs energies derived from their solubility products and range from 3 to 10 kJ/mol.

The resulting computed solidus/solutus curves in the Lippmann diagrams (Fig. 13) indicate a systematic Ce enrichment in the solid solutions relative to the aqueous solution which is enriched in the substituting REE. Groups 1 and 2 solid solutions (i.e., Ce-La, Ce-Pr, Ce-Nd, and Ce-Sm binaries) display an almost full overlap between solutus and solvus curves, implying that the aqueous solution and solid solution display similar REE composition (i.e., stoichiometric saturation). The Ce-Pr binary displays a peritectic at x_{REE} of ~0.4 and the Ce-Nd binary displays an eutectic point at x_{REE} of ~0.85 indicating a potential miscibility gap. Comparison between the Ce-Sm, Ce-Eu, and Ce-Gd binary solid solutions (Fig. 13d-f) indicates an increased gap between solidus and solutus curves. These solid solutions display therefore a preference for the formation of a Ce-rich solid solution with increased differences between the ionic radius Ce and the substituting REE from Sm to Gd.

4.3. Comparison to other rhabdophane studies and controls on crystal structure distortion

Only a few studies have investigated the properties of binary rhabdophane solid solutions, and to our knowledge, our study is the first to determine the thermodynamic properties of such solid solutions. Previous experimental work on rhabdophane largely focused on the incorporation of actinides in the rhabdophane structure (Qin et al., 2017; Huittinen et al., 2018) and optical/microstructural and thermal properties of mixed compositions (Buissette et al., 2004; Colomer et al., 2018; Liu et al., 2022).

In the study by Liu et al. (2022), the effects of ion concentrations and pH were studied to investigate the precipitation of Ce-Nd rhabdophane solid solutions from acidic solutions. Density functional theory calculations combined with XRD, Raman and other mineral characterization methods (i.e., SEM, TEM, and XPS) indicate that Nd is preferentially incorporated in non-hydrated sites with the presence of lattice distortion along the crystallographic *b*-axis (Liu et al., 2022). These observations corroborate with the solid solution grouping in our study and the prevalence of SRO effects displayed by the strong anomalies in the retrieved ΔH^{ex} and ΔS^{ex} functions for group 3 solid solutions (Ce-Eu and Ce-Gd binaries) and a smaller anomaly for the Ce-Nd binary (Figs. 7 and 12). The distortion on the phosphate tetrahdron depends on the size of the substituting REE, which is reflected by the Raman shifts on the symmetric ν_1-PO_4 vibrational bands that linearly increase from Ce to Nd, and becomes more pronounced for Ce-Eu and Ce-Gd binaries (Fig. 10c,e,g). The ΔV^{ex} functions derived in our study further indicate an asymmetry in the crystal structure that increases with larger differences in ionic radii of the substituting REE (Fig. 5).

Further inspection of the X-ray diffractograms by Liu et al. (2022) indicates the formation of single-phase Ce-Nd rhabdophane solid solutions in agreement with our observations. Rhabdophane powders synthesized in our study display however broader peaks and some peak shifts to lower 2θ angles for intermediate Ce-Nd binary compositions (Fig. 3a); our solid solutions also display more water content (Table 5, i.e. up to ~1 mol instead of 0.667) and display generally a smaller unit cell volume. The sharper X-ray diffractogram peaks and closer to ideal water contents in the study by Liu et al. (2022) might be explained by their synthesis method which was conducted at higher temperature and for longer time periods (i.e., 90 °C and up to 12 days). In our study, the solids synthesized are likely dominated by nucleation due to high supersaturation and the instantaneous precipitation in the calorimeter with reactions occurring at room temperature. Therefore, the binary rhabdophane solid solutions are also affected by aging and pH of the solution, which explains the high variability in structural properties of rhabdophane synthesized at various conditions as noted by Ochiai and Utsunomiya (2017) for endmember rhabdophane synthesis.

Huittinen et al. (2018) studied the incorporation of Cm^{3+} into a La-Gd rhabdophane solid solution using extended X-ray absorption fine-structure spectroscopy (EXAFS) and time-resolved laser-induced fluorescence spectroscopy (TRLFS). Similar to Liu et al. (2022), their study points to the importance of the hydrated vs. non-hydrated site configuration for ion substitution in the rhabdophane structure with a particular preference of Cm^{3+} substitution in the non-hydrated site (Huittinen et al., 2018). Their study further points out that 2/3 of the rhabdophane lattice sites are associated with water and therefore a preferential substitution on the non-hydrated site, which is somewhat indicative of local order-disorder in the crystal structure. These observations are in line with the SRO that becomes prevalent in group 3 solid solutions identified in our study.

4.4. Comparison to studies on monazite and controls of REE incorporation in non-ideal REE phosphate solid solutions

The thermodynamic mixing and structural properties of anhydrous monazite solid solutions have been investigated by several studies, including binary solid solutions involving La, Nd, Eu, and Gd (Popa et al., 2007; Li et al., 2014; Geisler et al., 2016; Hirsch et al., 2017; Neumeier et al., 2017; Huittinen et al., 2017; Schlenz et al., 2019). Based on these previous studies, there seems to be a growing consensus that the REE phosphates exhibit a slight non-ideal solid solution behavior that tends to become more pronounced with larger differences in the ionic radius of the

the substituting REE. Despite the anhydrous nature of these solid solutions, the following comparisons can be made with the rhabdophane solid solutions for enthalpy, volume, and structural properties.

Geisler et al. (2016) studied the structural changes in binary La-Eu monazite solid solutions using XRD and IR/Raman spectroscopy. In their study, they observed an excess molar volume (up to ~0.8 $Å^3$) and systematic shifts in Raman vibrational frequencies related to a structural distortion in the solid solutions (Geisler et al., 2016). Their XRD data (ΔV^{ex} vs. x_{Eu} diagram) indicate a slight asymmetry close to the monazite-(La) endmember which was fit to a regular solid solution model. This asymmetry is more prevalent in our study for the rhabdophane Ce-Eu solid solution (Fig. 5) but the overall higher excess volume for the endmember with the larger ionic radius (i.e., La and Ce over Eu) seems to prevail in both types of REE phosphate solid solutions.

Huittinen et al. (2017) characterized a series of Eu^{3+} doped La-Gd monazite solid solutions using Raman spectroscopy and TRLFS. Their results indicate a linear relationship between vibrational normal modes (v_1-v_4) and a broadening of Raman bands (i.e., FWHM of v_1, v_3, v_4) from the pure rhabdophane-(La) and -(Gd) endmembers to intermediate solid solutions (Huittinen et al., 2017). A similar relationship was observed in the Raman spectra from the rhabdophane solid solutions synthesized in our study (Figs. 9 and 10). The study by Huittinen et al. (2017) further concludes that a large contraction or distortion of the LnO_9 polyhedron results in a slight compression of the PO_4 tetrahedron and a loss of SRO around the LnO_9 polyhedron. Similarly, the rhabdophane Ce-Eu and Ce-Gd solid solutions also display SRO effects as deduced based on our calorimetric study (Figs. 7 and 12). These SRO effects can also be recognized in the study by Popa et al. (2007), where the excess enthalpy was determined using drop calorimetry at 1000 K for a series of binary monazite La-Nd, La-Eu, and La-Gd solid solutions. All of these solid solutions display a slight non-ideal excess enthalpy (~2-4 kJ/mol) which becomes more significant with decreased temperature. Some deviations in excess enthalpy data can be seen in comparison to the fitted regular model by Popa et al. (2007). Although these deviations are within their experimental uncertainty, it is interesting to note that for example the binary La-Gd monazite solid solution displays similar double peak inflections as observed in our calorimetric study (Fig. 7). It should be noted that enthalpies in their study do not strictly refer to the enthalpy of mixing, and therefore only a qualitative comparisons can be made to their data. Nevertheless, closer inspection of the oxide melt calorimetric data derived by Neumeier et al. (2017) suggests that binary monazite La-Eu and La-Gd solid solutions can be fit to a regular solid solution model, although these data show as well some deviations from this model which are difficult to resolve within experimental uncertainty of their method. Further comparison to the oxide melt solution calorimetric data by Schlenz et al. (2019) indicates that the enthalpy of mixing of binary La-Nd monazite solid solutions displays a strong asymmetry (i.e, with a maxima at x_{Nd} = 0.3) that were fit to a subregular solid solution model. Their Raman spectra indicate disturbances of local SRO reflected by an increase in the FWHM of the ν_1-PO4 stretching band as observed in our study for binary rhabdophane solid solutions (Fig. 10d,f,h).

5. CONCLUSIONS

The thermodynamic and structural properties of binary rhabdophane solid solutions were investigated using calorimetry, TGA-DSC, Raman and XRD. The measured excess enthalpies and volumes as well as the derived Gibbs energy functions indicate a non-ideal behavior for all the studied solid solutions which can be fit to an asymmetric Guggenheim function (Tables 2, 4, and 7).

Three major groups of solid solutions with different mixing behavior were distinguished here for the first time, including group 1) Ce-La and Ce-Pr binaries, group 2) Ce-Nd and Ce-Sm binaries, and group 3) Ce-Eu and Ce-Gd binaries, respectively. Several competing mechanisms were recognized to affect their measured enthalpies (Fig 7): i) departure of the ionic radius size of the substituting REE^{3+} from Ce^{3+}; ii) miscibility gaps or tendency for unmixing; iii) short-range ordering effects. Group 1 displays ΔH^{ex} values >0 which indicates a tendency towards unmixing, whereas groups 2 and 3 solid solutions display ΔH^{ex} values <0 which indicates a tendency of SRO most pronounced for Ce-Eu and Ce-Gd binary solid solutions (Fig. 7).

The Aq-SS approach was used to optimize the standard Gibbs energy of formation of the compositional endmembers, their interaction parameters, and also to derive the ΔG^{ex} and ΔG^{mix} functions for each solid solutions (Fig. 11e,f). These results are consistent with the precipitation of the full compositional solid solution range studied in the experiments and the REE aqueous solution chemistry. The solids synthesized in the calorimetric experiments are likely homogeneous solid solutions with a lack of any indication of unmixing based on the observed single peaks in X-ray diffractograms (Fig. 3) and the linear relationships between ν_1-PO_4 Raman bands and x_{REE} (Fig. 10). The precipitation behavior of these solid solutions (Fig. 6) displays a clear systematic from La to Gd, with a general preference of Ce incorporation in the solid solution over the smaller and heavier REE (i.e., Nd to Gd).

The non-ideal solid solution behavior and short-range ordering has been previously recognized in REE phosphates due to the preferential incorporation of the substituting REE on the non-hydrous LnO_9-site of rhabdophane (Huittinen et al., 2018; Li et al., 2022). The non-ideal solid solution characteristics and similarities in short-range ordering and lattice strain has also been observed in monazite solid solutions (Geisler et al., 2016; Huittinen et al., 2017; Neumeier et al., 2017; Schlenz et al., 2019).

The ΔH^{ex} and ΔV^{ex} functions for rhabdophane (Figs. 5 and 7) derived in our experimental study are very systematic and display intriguing structural and energetics in the rhabdophane structure than need to be further investigated using molecular dynamic simulations and EXAFS to better understand the local structural changes observed from Raman, XRD, and reflected in the calorimetric experiments. The data generated in this study comprise the first thermodynamic dataset on binary Ce-REE rhabdophane solid solutions, and therefore provides an important fundamental framework to simulate their stability and control on REE partitioning in natural systems. This work also has important implications in the study of immobilization of actinides in radioactive waste repositories.

ACKNOWLEDGMENTS

This project was supported by the National Science Foundation (NSF) grant EAR-2032761 to AG. This project also benefited from NSF-MRI grant EAR-2117061 to N.H. and A.G, which was used to acquire the Raman instrument. The TGA-DSC analyses were supported through NSF grant EAR-2149848 to XG. We would like to thank B. Frey from the Analytical Geochemistry

Laboratory in the New Mexico Bureau of Geology and Mineral Resources for assistance on ICP-OES and ICP-MS instruments, and research assistants M. Payne and R. Heath who contributed to the experimental data acquisition. We are honored to contribute to this special GCA issue dedicated to Terry M. Seward. AG: "Terry has influenced my career path several decades ago as an undergraduate/graduate student at ETH Zurich and well beyond. I am grateful to have met Terry who introduced me to aqueous geochemistry, my PhD advisor Andri, and who was also the impetus for my interest in hydrothermal geochemistry. Terry's research always was an inspiration on my scientific journey". We are grateful for the careful comments and suggestions from two anonymous reviewers, and we would like to thank Executive Editor Jeffrey Catalano and Guest Editor Kono Lemke for handling this manuscript.

APPENDIX A. SUPPLEMENTARY MATERIAL

Supplementary Tables include the calculated entropy of mixing from section 4.1.2. (Table S1), the calculated ΔG^{ex} and ΔG^{mix} (Tables S2), and the calculated ΔS^{ex} and ΔS^{mix} (Table S3). Additional XRD refinement and FHWM can be found in Tables S4 and S5, and Figure S1-S2, and SEM images in Figure S3.

DATA AVAILABILITY

Data are available through Mendeley Data (doi: 10.17632/47zptxbnd4.1) at https://data.mendeley.com/datasets/47zptxbnd4/1

941 **REFERENCES**

Andersen A. K., Clark J. G., Larson P. B. and Donovan J. J. (2017) REE fractionation, mineral speciation, and supergene enrichment of the Bear Lodge carbonatites, Wyoming, USA. Ore Geol. Rev. 89, 780–807.

Andersen A. K., Clark J. G., Larson P. B. and Neill O. K. (2016) Mineral chemistry and petrogenesis of a HFSE(+HREE) occurrence, peripheral to carbonatites of the Bear Lodge alkaline complex, Wyoming. Am. Mineral. 101, 1604–1623.

Anfimova T., Li Q., Jensen J. O. and Bjerrum N. J. (2014) Thermal stability and proton conductivity of rare earth orthophosphate hydrates. Int. J. Electrochem. Sci. 9, 2285–2300.

Arinicheva Y., Gausse C., Neumeier S., Brandt F., Rozov K., Szenknect S., Dacheux N., Bosbach D. and Deissmann G. (2018) Influence of temperature on the dissolution kinetics of synthetic $LaPO_4$-monazite in acidic media between 50 and 130 °C. J. Nucl. Mater. 509, 488–495.

Berger A., Gnos E., Janots E., Fernandez A. and Giese J. (2008) Formation and composition of rhabdophane, bastnäsite and hydrated thorium minerals during alteration: Implications for geochronology and low-temperature processes. Chem. Geol. 254, 238–248.

Buissette V., Moreau M., Gacoin T., Boilot J.P., Chane-Ching J.Y. and Le Mercier T. (2004) Colloidal synthesis of luminescent rhabdophane $LaPO_4:Ln^{3+} \cdot x\ H_2O$ (Ln = Ce, Tb, Eu; $x \approx 0.7$) nanocrystals. Chem. Mater. 16, 3767–3773.

Byrne R. H. and Kim K.-H. (1993) Rare earth precipitation and coprecipitation behavior: The limiting role of PO_4^{3-} on dissolved rare earth concentrations in seawater. Geochimica et Cosmochimica Acta 57, 519–526.

Cetiner Z. S., Wood S. A. and Gammons C. H. (2005) The aqueous geochemistry of the rare earth elements. part XIV. the solubility of rare earth element phosphates from 23 to 150 °C. Chem. Geol. 217, 147–169.

Clavier N., Mesbah A., Szenknect S. and Dacheux N. (2018) Monazite, rhabdophane, xenotime & churchite: vibrational spectroscopy of gadolinium phosphate polymorphs. Spectrochim. Acta. A. Mol. Biomol. Spectrosc. 205, 85–94.

Colomer M. T., Zur L., Ferrari M. and Ortiz A. L. (2018) Structural-microstructural characterization and optical properties of Eu^{3+},Tb^{3+}-codoped $LaPO_4{\cdot}nH_2O$ and $LaPO_4$ nanorods hydrothermally synthesized with microwaves. Ceram. Intern. 44, 11993–12001.

Cook N. J., Ciobanu C. L., Wade B. P., Gilbert S. E. and Alford R. (2023) Mineralogy and distribution of REE in oxidised ores of the Mount Weld Laterite Deposit, Western Australia. Minerals 13, 656.

Dacheux N., Clavier N. and Podor R. (2013) Versatile monazite: resolving geological records and solving challenges in materials science. monazite as a promising long-term radioactive waste matrix: benefits of high-structural flexibility and chemical durability. Am. Mineral. 98, 833–847.

Diakonov I. I., Ragnarsdottir K. V. and Tagirov B. R. (1998) Standard thermodynamic properties and heat capacity equations of rare earth hydroxides:: II. Ce(III)-, Pr-, Sm-, Eu(III)-, Gd-, Tb-, Dy-, Ho-, Er-, Tm-, Yb-, and Y-hydroxides. comparison of thermochemical and solubility data. Chem. Geol. 151, 327–347.

Du Fou de Kerdaniel E., Clavier N., Dacheux N., Terra O. and Podor R. (2007) Actinide solubility-controlling phases during the dissolution of phosphate ceramics. J. Nucl. Mater. 362, 451–458.

Errandonea D., Gomis O., Rodríguez-Hernández P., Muñoz A., Ruiz-Fuertes J., Gupta M., Achary S. N., Hirsch A., Manjon F. J., Peters L., Roth G., Tyagi A. K. and Bettinelli M.

(2018) High-pressure structural and vibrational properties of monazite-type $BiPO_4$, $LaPO_4$, $CePO_4$, and $PrPO_4$. J. Phys.: Condens. Matter 30, 065401.

Gausse C., Szenknect S., Qin D. W., Mesbah A., Clavier N., Neumeier S., Bosbach D. and Dacheux N. (2016) Determination of the solubility of rhabdophanes $LnPO_4 \cdot 0.667H_2O$ (Ln = La to Dy). Eur. J. Inorg. Chem. 2016, 4615–4630.

Gavrichev K. S., Gurevich V. M., Ryumin M. A., Tyrin A. V. and Komissarova L. N. (2016) Low-temperature heat capacity and thermodynamic properties of $PrPO_4$. Geochem. Int. 54, 362–368.

Gavrichev K. S., Gurevich V. M., Ryumin M. A., Tyurin A. V. and Komissarova L. N. (2015) Heat capacity and thermodynamic functions of $SmPO_4$ at 10–1600 K. Geochem. Int. 53, 607–616.

Gavrichev K. S., Ryumin M. A., Tyurin A. V., Gurevich V. M. and Komissarova L. N. (2008) Refined heat capacity of $LaPO_4$ in the temperature range 0–1600 K. Thermochim. Acta 474, 47–51.

Gavrichev K. S., Ryumin M. A., Tyurin A. V., Gurevich V. M. and Komissarova L. N. (2009) The heat capacity and thermodynamic functions of $EuPO_4$ over the temperature range 0–1600 K. Russ. J. Phys. Chem. 83, 901–906.

Geisler T., Popa K. and Konings R. J. M. (2016) Evidence for lattice strain and non-ideal behavior in the $(La_{1-x}Eu_x)PO_4$ solid solution from X-ray diffraction and vibrational spectroscopy. Front. Earth Sci. 4.

Giovannini A. L., Bastos Neto A. C., Porto C. G., Takehara L., Pereira V. P. and Bidone M. H. (2021) REE mineralization (primary, supergene and sedimentary) associated to the Morro dos Seis Lagos Nb (REE, Ti) deposit (Amazonas, Brazil). Ore Geol. Rev. 137, 104308.

Glasser L. (2011) Thermodynamics of condensed phases: formula unit volume, V_m , and the determination of the number of formula units, Z , in a crystallographic unit cell. J. Chem. Educ. 88, 581–585.

Goncharov V. G., Nisbet H., Strzelecki A., Benmore C. J., Migdisov A. A., Xu H. and Guo X. (2022) Energetics of hydroxylbastnäsite solid solutions, $La_{1-x}Nd_xCO_3OH$. Geochim. Cosmochim. Acta 330, 47–66.

Guo X., Szenknect S., Mesbah A., Clavier N., Poinssot C., Wu D., Xu H., Dacheux N., Ewing R. C. and Navrotsky A. (2016) Energetics of a uranothorite ($Th_{1-x}U_x SiO_4$) solid solution. Chem. Mater. 28, 7117–7124.

Gysi A. P. and Harlov D. (2021) Hydrothermal solubility of $TbPO_4$, $HoPO_4$, $TmPO_4$, and $LuPO_4$ xenotime endmembers at pH of 2 and temperatures between 100 and 250 °C. Chem. Geol. 567, 120072.

Gysi A. P., Harlov D. and Miron G. D. (2018) The solubility of monazite ($CePO_4$), $SmPO_4$, and $GdPO_4$ in aqueous solutions from 100 to 250 °C. Geochim. Cosmochim. Acta 242, 143–164.

Gysi A. P., Hurtig N. C., Pan R., Miron G. D. and Kulik D. A. (2023) MINES thermodynamic database, In: New Mexico Bureau of Geology and Mineral Resources, version 23.

Gysi A. P., Williams-Jones A. E. and Harlov D. (2015) The solubility of xenotime-(Y) and other HREE phosphates ($DyPO_4$, $ErPO_4$ and $YbPO_4$) in aqueous solutions from 100 to 250 °C and p_{sat}. Chem. Geol. 401, 83–95.

Haas J. R., Shock E. L. and Sassani D. C. (1995) Rare earth elements in hydrothermal systems: Estimates of standard partial molal thermodynamic properties of aqueous complexes of the rare earth elements at high pressures and temperatures. Geochim. Cosmochim. Acta 59, 4329–4350.

Hirsch A., Kegler P., Alencar I., Ruiz-Fuertes J., Shelyug A., Peters L., Schreinemachers C., Neumann A., Neumeier S., Liermann H.-P., Navrotsky A. and Roth G. (2017) Structural, vibrational, and thermochemical properties of the monazite-type solid solution $La_{1-x}Pr_x PO_4$. J. Solid State Chem. 245, 82–88.

Huittinen N., Arinicheva Y., Kowalski P. M., Vinograd V. L., Neumeier S. and Bosbach D. (2017) Probing structural homogeneity of $La_{1-x}Gd_xPO_4$ monazite-type solid solutions by combined spectroscopic and computational studies. J. Nucl. Mater. 486, 148–157.

Huittinen N., Scheinost A. C., Ji Y., Kowalski P. M., Arinicheva Y., Wilden A., Neumeier S. and Stumpf T. (2018) A spectroscopic and computational study of Cm^{3+} incorporation in lanthanide phosphate rhabdophane ($LnPO_4 \cdot 0.67H_2O$) and monazite ($LnPO_4$). Inorg. Chem. 57, 6252–6265.

Hutchinson M., Slezak P., Wendlandt R. and Hitzman M. (2022) Rare earth element enrichment in the eeathering profile of the Bull Hill carbonatite at Bear Lodge, Wyoming, USA. Econ. Geol. 117, 813–831.

Ichimura K., Sanematsu K., Kon Y., Takagi T. and Murakami T. (2020) REE redistributions during granite weathering: Implications for Ce anomaly as a proxy for paleoredox states. Am. Mineral. 105, 848–859.

Jenkins H. D. B. and Glasser L. (2003) Standard absolute entropy, S^{o}_{298}, values from volume or density. 1. Inorganic Materials. Inorg. Chem. 42, 8702–8708.

Katsikopoulos D., Fernández-González Á. and Prieto M. (2009) Precipitation and mixing properties of the “disordered” $(Mn,Ca)CO_3$ solid solution. Geochim. Cosmochim. Acta 73, 6147–6161.

Kestin J., Sengers J. V., Kamgar-Parsi B. and Sengers J. M. H. L. (1984) Thermophysical properties of fluid H_2O. J. Phys. Chem. Ref. Data 13, 175–183.

Knight, A.W., Kalugin, N.G., Coker, E. and Ilegen A.G. (2019) Water properties under nano-scale confinement. Sci. Rep. 9, 8246 .

Kolesov B. (2006) Raman investigation of H_2O molecule and hydroxyl groups in the channels of hemimorphite. Am. Min. 91, 1355–1362.

Konings R. J. M., Beneš O., Kovács A., Manara D., Sedmidubský D., Gorokhov L., Iorish V. S., Yungman V., Shenyavskaya E. and Osina E. (2014) The thermodynamic properties of the *f*-elements and their compounds. Part 2. the lanthanide and actinide oxides. J. Phys. Chem. Ref. Data 43, 013101.

Kulik D. A. (2006) Dual-thermodynamic estimation of stoichiometry and stability of solid solution end members in aqueous-solid solution systems. Chem. Geol. 225, 189–212.

Kulik D. A., Vinograd V. L., Paulsen N. and Winkler B. (2010) $(Ca,Sr)CO_3$ aqueous-solid solution systems: from atomistic simulations to thermodynamic modelling. Phys. Chem. Earth 35, 217–232.

Kulik D. A., Wagner T., Dmytrieva S. V., Kosakowski G., Hingerl F. F., Chudnenko K. V. and Berner U. R. (2013) GEM-Selektor geochemical modeling package: revised algorithm and GEMS3K numerical kernel for coupled simulation codes. Comput Geosci. 17, 1–24.

Li Y., Piotr M. K., Blanca-Romero A., Vinograd V. and Bosbach D. (2014) *Ab initio* calculation of excess properties of $La_{1-x}(Ln,An)_xPO_4$ Solid Solutions. J. Solid State Chem. 220, 137–41.

Liu H., Zhao X., Teng Y., Li Y., Zheng X., Wang S., Wu L., Panda P. K. and Ahuja R. (2022) Investigation of Nd^{3+} incorporation in Ce-rhabdophane: insight from structural flexibility and occupation mechanism. J. Am. Ceram. Soc. 105, 4974–4985.

Lutterotti L., Matthies S. and Wenk H. R. (1999) MAUD: a friendly Java program for material analysis using diffraction. Int. U. Crystallogr. Comm. Powder Diffraction Newsletter 21, 14–15.

Majzlan J., Grevel K.-D. and Navrotsky A. (2003) Thermodynamics of Fe oxides: Part II. Enthalpies of formation and relative stability of goethite (α-FeOOH), lepidocrocite (γ-FeOOH), and maghemite (γ-Fe_2O_3). Am. Min. 88, 855–859.

Mazeina L. and Navrotsky A. (2005) Surface enthalpy of goethite. Clays and Clay Min. 53, 113–122.

Mesbah A., Clavier N., Elkaim E., Gausse C., Kacem I. B., Szenknect S. and Dacheux N. (2014) Monoclinic form of the rhabdophane compounds: $REEPO_4 \cdot 0.667H_2O$. Cryst. Growth Des. 14, 5090–5098.

Miron G. D., Kulik D. A., Dmytrieva S. V. and Wagner T. (2015) GEMSFITS: code package for optimization of geochemical model parameters and inverse modeling. Appl. Geochem. 55, 28–45.

Navrotsky A., Lee W., Mielewczyk-Gryn A., Ushakov S. V., Anderko A., Wu H. and Riman R. E. (2015) Thermodynamics of solid phases containing rare earth oxides. J. Chem. Thermodyn. 88, 126–141.

Neumeier S., Kegler P., Arinicheva Y., Shelyug A., Kowalski P. M., Schreinemachers C., Navrotsky A. and Bosbach D. (2017) Thermochemistry of $La_{1-x}Ln_xPO_4$-monazites (Ln= Gd, Eu). J. Chem. Thermodyn. 105, 396–403.

Ni Y., Hughes J. M. and Mariano A. N. (1995) Crystal chemistry of the monazite and xenotime structures. Am. Mineral. 80, 21–26.

Ochiai A. and Utsunomiya S. (2017) Crystal chemistry and stability of hydrated rare-rarth phosphates formed at room temperature. Minerals 7, 84.

Pan R., Gysi A. P., Miron G. D. and Zhu C. (2024) Optimized thermodynamic properties of REE aqueous species (REE^{3+} and $REEOH^{2+}$) and experimental database for modeling the solubility of REE phosphate minerals (monazite, xenotime, and rhabdophane) from 25 to 300 °C. Chem. Geol. 643, 121817.

Poitrasson F., Oelkers E., Schott J. and Montel J.M. (2004) Experimental determination of synthetic $NdPO_4$ monazite end-member solubility in water from 21 °C to 300 °C: implications for rare earth element mobility in crustal fluids. Geochim. Cosmochim. Acta 68, 2207–2221.

Popa K. and Konings R. J. M. (2006) High-temperature heat capacities of $EuPO_4$ and $SmPO_4$ synthetic monazites. Thermochim. Acta 445, 49–52.

Popa K., Konings R. J. M. and Geisler T. (2007) High-temperature calorimetry of $(La_{1-x}Ln_x)PO_4$ solid solutions. J. Chem. Thermodyn. 39, 236–239.

Prieto M. (2009) Thermodynamics of solid solution-aqueous solution systems. Rev. Mineral. Geochem. 70, 47–85.

Qin D., Mesbah A., Gausse C., Szenknect S., Dacheux N. and Clavier N. (2017) Incorporation of thorium in the rhabdophane structure: synthesis and characterization of $Pr_{1-2x}Ca_xTh_xPO_4 \cdot nH_2O$ solid solutions. J. Nucl. Mater. 492, 88–96.

Rafiuddin M. R. and Grosvenor A. P. (2016) A structural investigation of hydrous and anhydrous rare-earth phosphates. Inorg. Chem. 55, 9685–9695.

Robinson R. A. and Stokes R. H. (1968) Electrolyte Solutions, 2nd ed. Butterworths, London.

Schlenz H., Dellen J., Kegler P., Gatzen C., Schreinemachers C., Shelyug A., Klinkenberg M., Navrotsky A. and Bosbach D. (2019) Structural and thermodynamic mixing properties of $La_{1-x}Nd_xPO_4$ monazite-type solid solutions. J. Solid State Chem. 270, 470–478.

Seydoux-Guillaume A.M., Montel J.M., Bingen B., Bosse V., De Parseval P., Paquette J.L., Janots E. and Wirth R. (2012) Low-temperature alteration of monazite: fluid mediated coupled dissolution-precipitation, irradiation damage, and disturbance of the U-Pb and Th-Pb chronometers. Chem. Geol. 330–331, 140–158.

Shannon R. D. (1976) Revised effective ionic radii and systematic studies of interatomie distances in halides and chaleogenides. Acta Cryst. A32, 751–767.

Shelyug A., Mesbah A., Szenknect S., Clavier N., Dacheux N. and Navrotsky A. (2018) Thermodynamics and stability of rhabdophanes, hydrated rare earth phosphates $REPO_4 \cdot n H_2O$. Front. Chem. 6, 604.

Shock E. L. and Helgeson H. C. (1988) Calculation of the thermodynamic and transport properties of aqueous species at high pressures and temperatures: correlation algorithms for ionic species and equation of state predictions to 5 kb and 1000 °C. Geochim. Cosmochim. Acta 52, 2009–2036.

Shock E. L., Sassani D. C., Willis M. and Sverjensky D. A. (1997) Inorganic species in geologic fluids: correlations among standard molal thermodynamic properties of aqueous ions and hydroxide complexes. Geochim. Cosmochim. Acta 61, 907–950.

Silva E. N., Ayala A. P., Guedes I., Paschoal C. W. A., Moreira R. L., Loong C.K. and Boatner L. A. (2006) Vibrational spectra of monazite-type rare-earth orthophosphates. Opt. Mater. 29, 224–230.

Strzelecki A. C., Kriegsman K., Estevenon P., Goncharov V., Bai J., Szenknect S., Mesbah A., Wu D., McCloy J. S., Dacheux N. and Guo X. (2020) High-temperature thermodynamics of cerium silicates, A-$Ce_2Si_2O_7$, and $Ce_{4.67}(SiO_4)_3O$. ACS Earth Space Chem. 4, 2129–2143.

Strzelecki A. C., Reece M., Zhao X., Yu W., Benmore C., Ren Y., Alcorn C., Migdisov A., Xu H. and Guo X. (2022a) Crystal chemistry and thermodynamics of HREE (Er, Yb) mixing in a xenotime solid solution. ACS Earth Space Chem. 6, 1375–1389.

Strzelecki A. C., Ren Y., Chong S., Riley B. J., Xu H., McCloy J. S. and Guo X. (2022b) Structure and thermodynamics of calcium rare earth silicate oxyapatites, $Ca_2RE_8(SiO_4)_6O_2$ (RE = Pr, Tb, Ho, Tm). Phys. Chem. Miner. 49, 13.

Sun Q. (2009) The Raman OH stretching bands of liquid water.Vib. Spec. 51, 213–217.

Thiriet C., Konings R. J. M., Javorský P., Magnani N., and F. Wastin (2005) The low temperature heat capacity of $LaPO_4$ and $GdPO_4$, the thermodynamic functions of the monazite-type $LnPO_4$ series. J. Chem. Thermodyn. 37, 131–139.

Thiriet C., Konings R. J. M., Javorský P. and Wastin F. (2004) The heat capacity of cerium orthophosphate $CePO_4$, the synthetic analogue of monazite. Phys. Chem. Miner. 31, 347–352.

Ushakov S. V., Helean K. B., Navrotsky A. and Boatner L. A. (2001) Thermochemistry of rare-earth orthophosphates. J. Mater. Res. 16, 2623–2633.

Van Hoozen C. J., Gysi A. P. and Harlov D. E. (2020) The solubility of monazite ($LaPO_4$, $PrPO_4$, $NdPO_4$, and $EuPO_4$) endmembers in aqueous solutions from 100 to 250 °C. Geochim. Cosmochim. Acta 280, 302–316.

Vinograd V. and Winkler B. (2010) An efficient cluster expansion method for binary solid solutions: application to the halite-silvite, NaCl-KCl, system. Rev. Mineral. Geochem. 71, 413–436.

Wagner T., Kulik D. A., Hingerl F. F. and Dmytrievava S. V. (2012) GEM-SELEKTOR geochemical modeling package: TSolMod library and data interface for multicomponent phase models. Can. Mineral. 50, 1173–1195.

Williams M. L., Jercinovic M. J., Harlov D. E., Budzyń B. and Hetherington C. J. (2011) Resetting monazite ages during fluid-related alteration. Chem. Geol. 283, 218–225.

Wojdyr M. (2010) Fityk: a general-purpose peak fitting program. J. Appl. Cryst. 43, 1126–1128.

FIGURE CAPTIONS

Figure 1. X-ray diffractograms of rhabdophane endmembers $REEPO_4{\cdot}nH_2O$ (REE= La, Ce, Pr, Nd, Sm, Eu, and Gd) precipitated during the calorimetric experiments showing a comparison

between modeled (Rietveld refinement) and measured XRD spectra indexed for the monoclinic *C*2 structure. Numbers in brackets are the Miller indices for major XRD reflections. The comparison indicates a (51-1) and (711) peak shift towards higher 2θ angles and an increase in (-222) and (-111) peaks sharpness from La to Gd.

Figure 2. Lattice parameters of rhabdophane endmembers precipitated in this study refined in the monoclinic *C*2 crystal structure and comparison to other studies (Mesbah et al., 2014; Ochiai and Utsunomiya, 2017; Shelyug et al., 2018). The unit cell parameters include (a-c) the *a*, *b*, and *c* crystallographic axes and (d) the calculated unit cell molar volumes (V_{cell} in Å). The values of the refined lattice parameters are listed in Table 1.

Figure 3. X-ray diffractograms of (a) Ce-Nd and (b) Ce-Gd binary rhabdophane solid solutions precipitated in the calorimetric experiments showing a comparison between modeled (Rietveld refinement) and measured XRD spectra indexed for the *C*2 crystal structure. Numbers in brackets are the Miller indices for major XRD reflections. Numbers on the right side indicate the compositions of the REE solid solutions (Table 1). The comparison indicates peak shifts between endmembers and solid solution compositions.

Figure 4. Molar volume of binary rhabdophane solid solutions (V_{SS}) as a function of mole fraction REE (*x*) in $Ce_{1-x}REE_xPO_4 \cdot nH_2O$ (REE= La, Pr, Nd, Sm, Eu, Gd).

Figure 5. Excess volume of mixing (ΔV^{ex}) of binary rhabdophane solid solutions as a function of mole fraction REE (x_{REE}) in $Ce_{1-x}REE_xPO_4{\cdot}nH_2O$ (REE= La, Pr, Nd, Sm, Eu, Gd). The experimental data are listed in Table 1 and the fits in Table 2.

Figure 6. Amount of REE phosphates precipitated (in mmol) as a function of mole fraction REE (x_{REE}) in $Ce_{1-x}REE_xPO_4{\cdot}nH_2O$ (REE= La, Pr, Nd, Sm, Eu, Gd), determined from REE measured in the starting and final experimental solutions (Table 3).

Figure 7. Excess enthalpies of mixing (ΔH^{ex} in kJ/mol) as a function of mole fraction REE (x_{REE}) in $Ce_{1-x}REE_xPO_4{\cdot}nH_2O$ (REE= La, Pr, Nd, Sm, Eu, Gd) binary solid solution series determined using calorimetry. The error bars denote the standard deviations based on duplicate to quadruplicate experiments. The experimental data are listed in Table 3 and the fits in Table 4.

Figure 8. TGA-DSC analysis of binary (a) Ce-Nd and (b) Ce-Gd solid solutions from 30−500 °C. Integration bounds for enthalpy dehydration steps calculations are marked by the blue dashed lines. The integrated enthalpy and water contents are listed in Table 5.

Figure 9. Raman spectra of: (a) symmetric (v_1) and asymmetric (v_3) vibrational phosphate stretching bands for monazite-(Ce) and rhabdophane-(Ce) endmembers; (b) peak center shift of the two main subpeaks of v_1-PO_4 in rhabdophane endmembers and solid solutions with decreasing ionic radii; (c) the vibrational stretching band for water in rhabdophane endmembers; (d) water subpeak area 2 (v_1-H_2O at 3458 cm^{-1}) increasing with decreasing ionic radii. White

squares in (c) correspond to the Ce, Nd and Gd endmembers measured in previous studies (Clavier et al., 2018; Liu et al., 2022).

Figure 10. Raman spectra of symmetric vibrational phosphate stretching band shifts (ν_1-PO_4) and full width at half maxima (FWHM) for binary (a,b) Ce-Pr, (c,d) Ce-Nd, (e,f) Ce-Eu and (g,h) Ce-Gd rhabdophane solid solutions. The Δ_{FWHM} values show the departure of FWHM for solid solutions from a linear interpolation between endmembers indicating non-ideal solid solution behavior due to short-range ordering.

Figure 11. Excess Gibbs energy (ΔG^{ex}) and Gibbs energy of mixing (ΔG^{mix}) as a function of mole fraction REE (x_{REE}) in the rhabdophane solid solutions determined using three different approaches: (a-b) assuming disordering and random mixing with ΔG^{ex}=ΔH^{ex} and S^{ex}=0 (section 4.1.1.); (c-d) assuming S^{ex}≠0, with entropy determined from molar volume data (section 4.1.2.); (e-f) ΔG^{ex} calculated from thermodynamic optimizations of solubility data using GEMSFITS and Aq-SS equilibria calculations (section 4.2.1.). Calculated Gibbs energy values are listed in the Supplementary Material Table S2.

Figure 12. Excess entropy (ΔS^{ex}) and entropy of mixing (ΔS^{mix}) as a function of mole fraction REE (x_{REE}) in the rhabdophane solid solutions determined using two different approaches: (a-b) from XRD molar volume data (section 4.1.2.); (c-d) calculated using Eqs. 13 and 14 and the ΔG^{ex} calculated from thermodynamic optimizations of solubility data using GEMSFITS and Aq-

SS equilibria calculations (section 4.2.1.). Calculated entropy values are listed in the Supplementary Material Tables S1 and S3.

Figure 13. Lippmann diagrams (Eqs. 15-18) showing the logarithm of the total dissolved element (TE) solubility product (ΣΠ) as a function of mole fraction REE (x_{REE}) in the rhabdophane solid solutions. These diagrams were constructed using the GEMS code package (Kulik et al., 2013) process simulator and thermodynamic properties optimized using GEMSFITS (Miron et al., 2015) with parameters listed in Table 7. The computed "Solutus" curve indicates the REE composition of the aqueous solution and the "Solidus" curve the composition of the conjugate solid solution. The experimental data represent the REE concentrations measured in the experimental aqueous solutions.

FIGURES

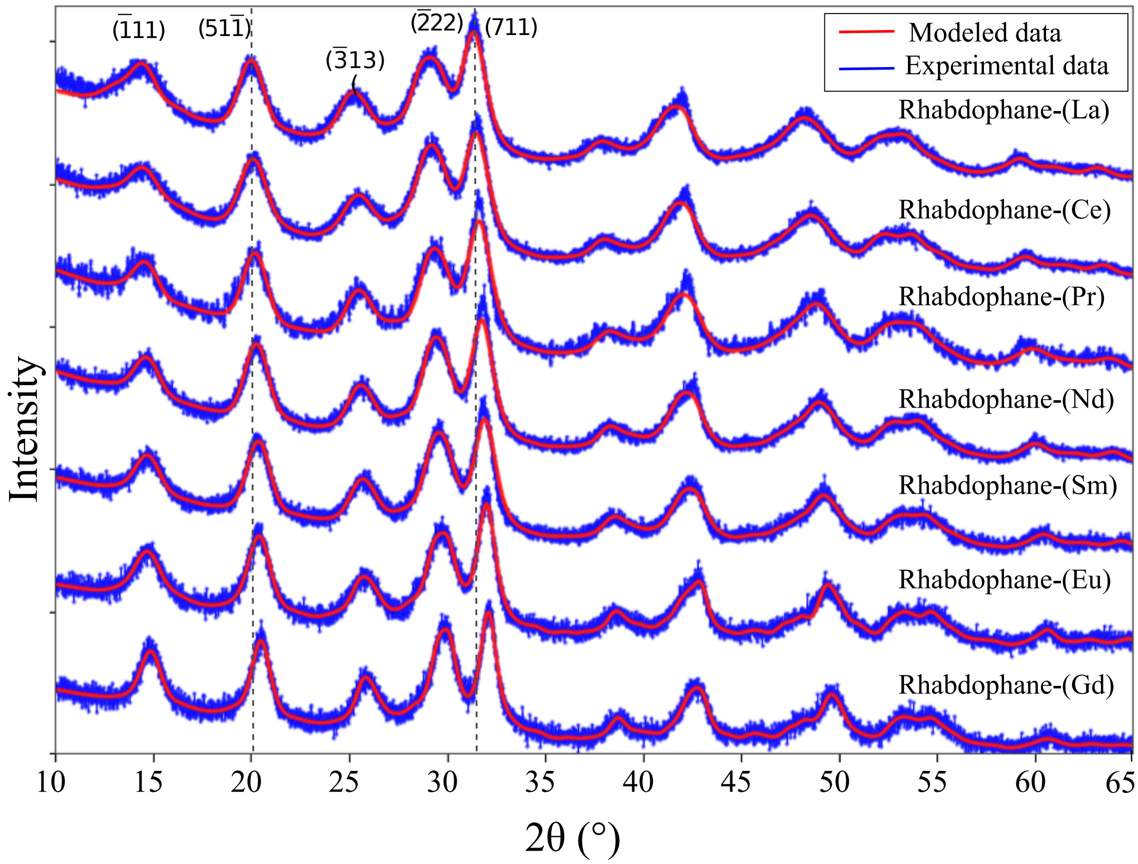

Figure 1. X-ray diffractograms of rhabdophane endmembers $REEPO_4 \cdot nH_2O$ (REE= La, Ce, Pr, Nd, Sm, Eu, and Gd) precipitated during the calorimetric experiments showing a comparison between modeled (Rietveld refinement) and measured XRD spectra indexed for the monoclinic *C*2 structure. Numbers in brackets are the Miller indices for major XRD reflections. The comparison indicates a (51-1) and (711) peak shift towards higher 2θ angles and an increase in (-222) and (-111) peaks sharpness from La to Gd.

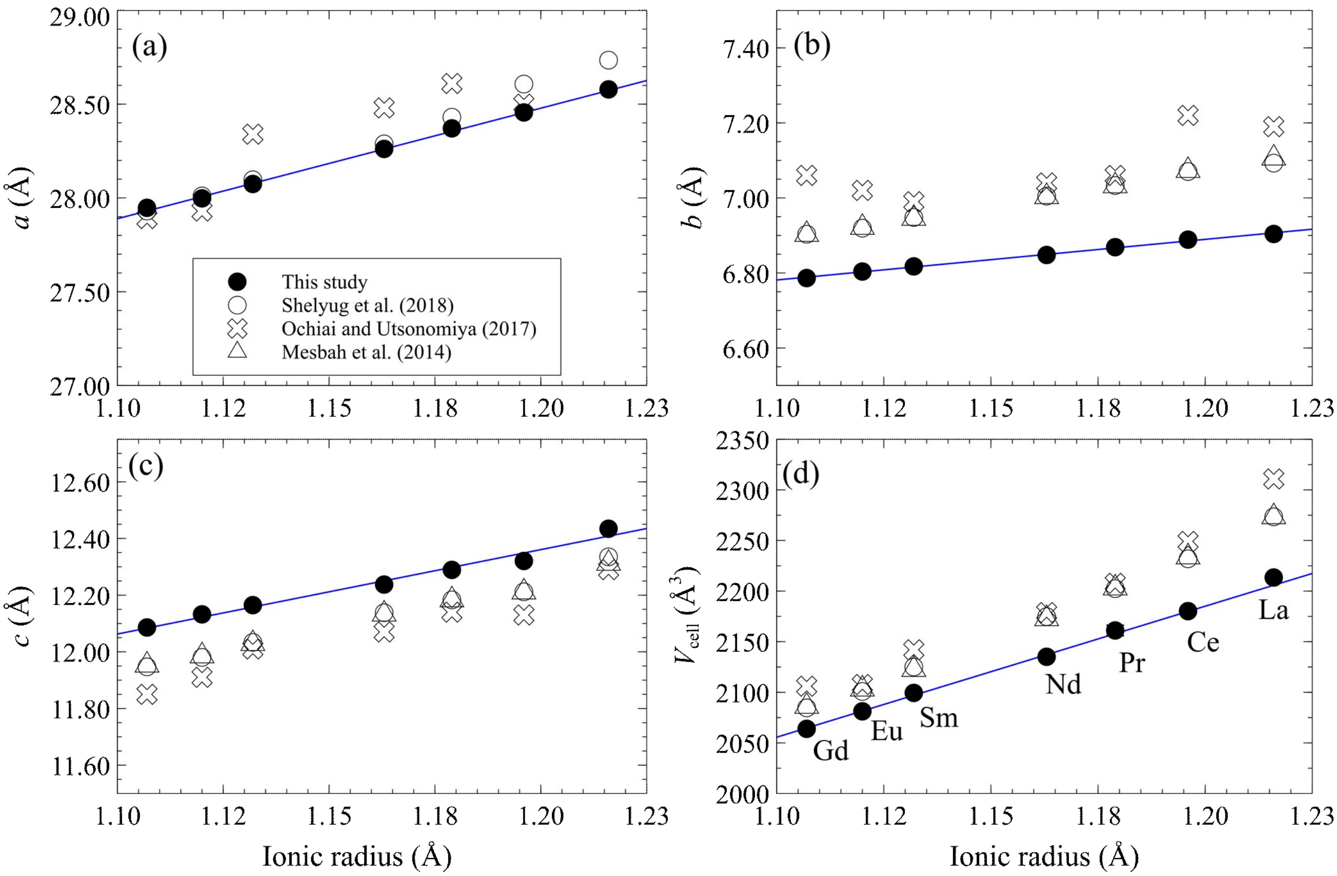

Figure 2. Lattice parameters of rhabdophane endmembers precipitated in this study refined in the monoclinic *C*2 crystal structure and comparison to other studies (Mesbah et al., 2014; Ochiai and Utsunomiya, 2017; Shelyug et al., 2018). The unit cell parameters include (a-c) the *a*, *b*, and *c* crystallographic axes and (d) the calculated unit cell molar volumes (V_{cell} in Å). The values of the refined lattice parameters are listed in Table 1.

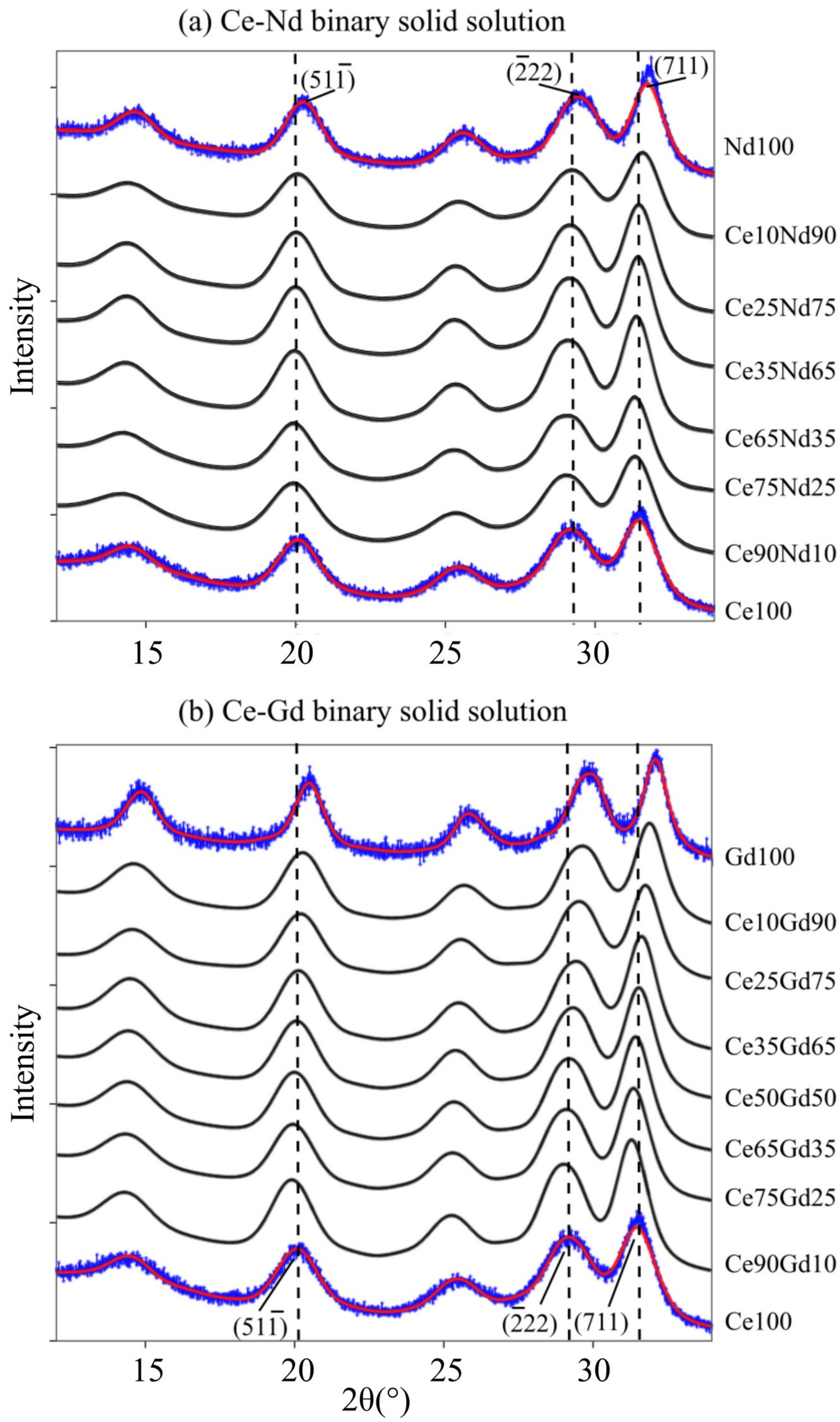

Figure 3. X-ray diffractograms of (a) Ce-Nd and (b) Ce-Gd binary rhabdophane solid solutions precipitated in the calorimetric experiments showing a comparison between modeled (Rietveld refinement) and measured XRD spectra indexed for the *C*2 crystal structure. Numbers in brackets are the Miller indices for major XRD reflections. Numbers on the right side indicate the compositions of the REE solid solutions (Table 1). The comparison indicates peak shifts between endmembers and solid solution compositions.

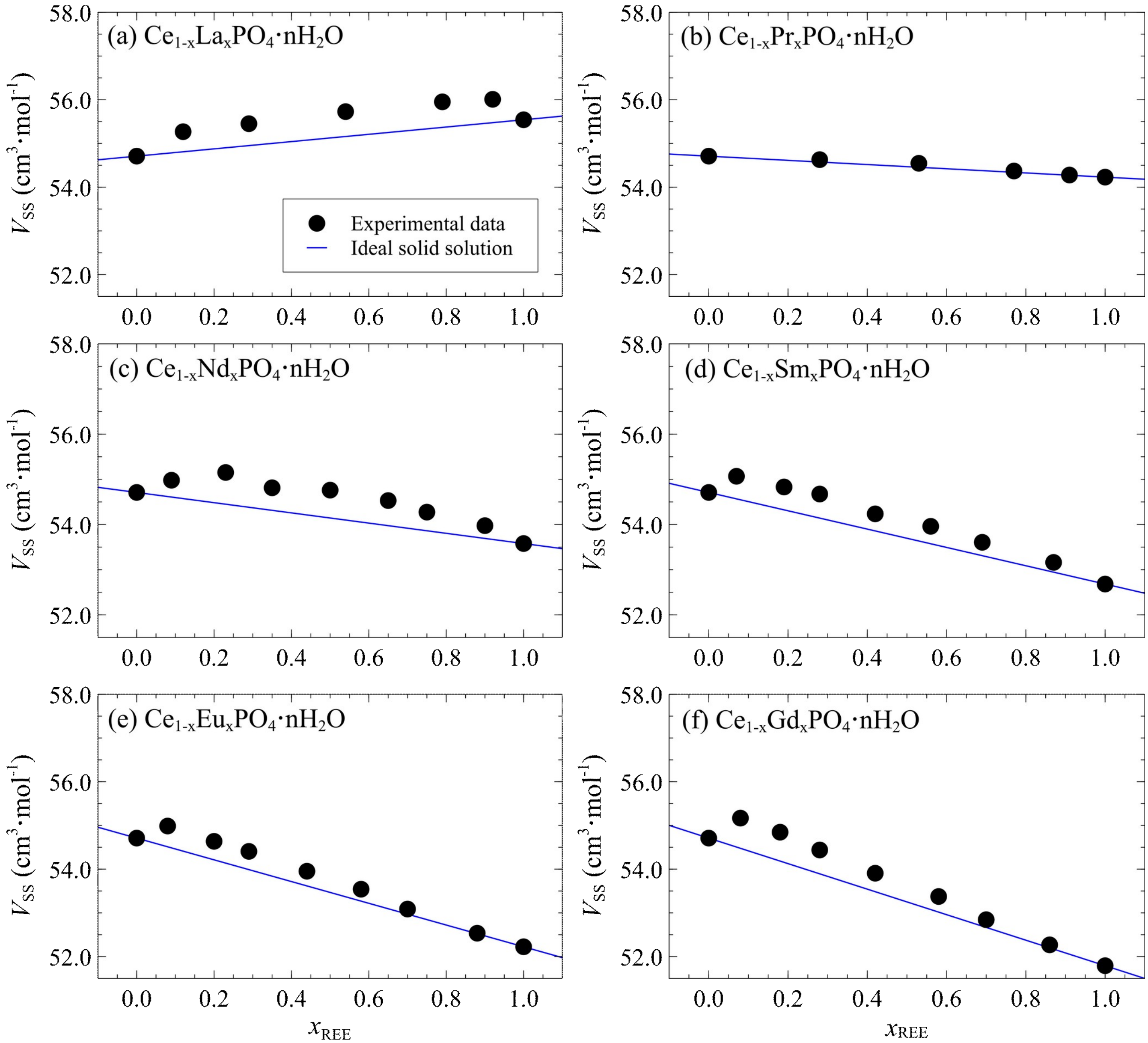

Figure 4. Molar volume of binary rhabdophane solid solutions (V_{SS}) as a function of mole fraction REE (x) in $Ce_{1-x}REE_xPO_4{\bullet}nH_2O$ (REE= La, Pr, Nd, Sm, Eu, Gd).

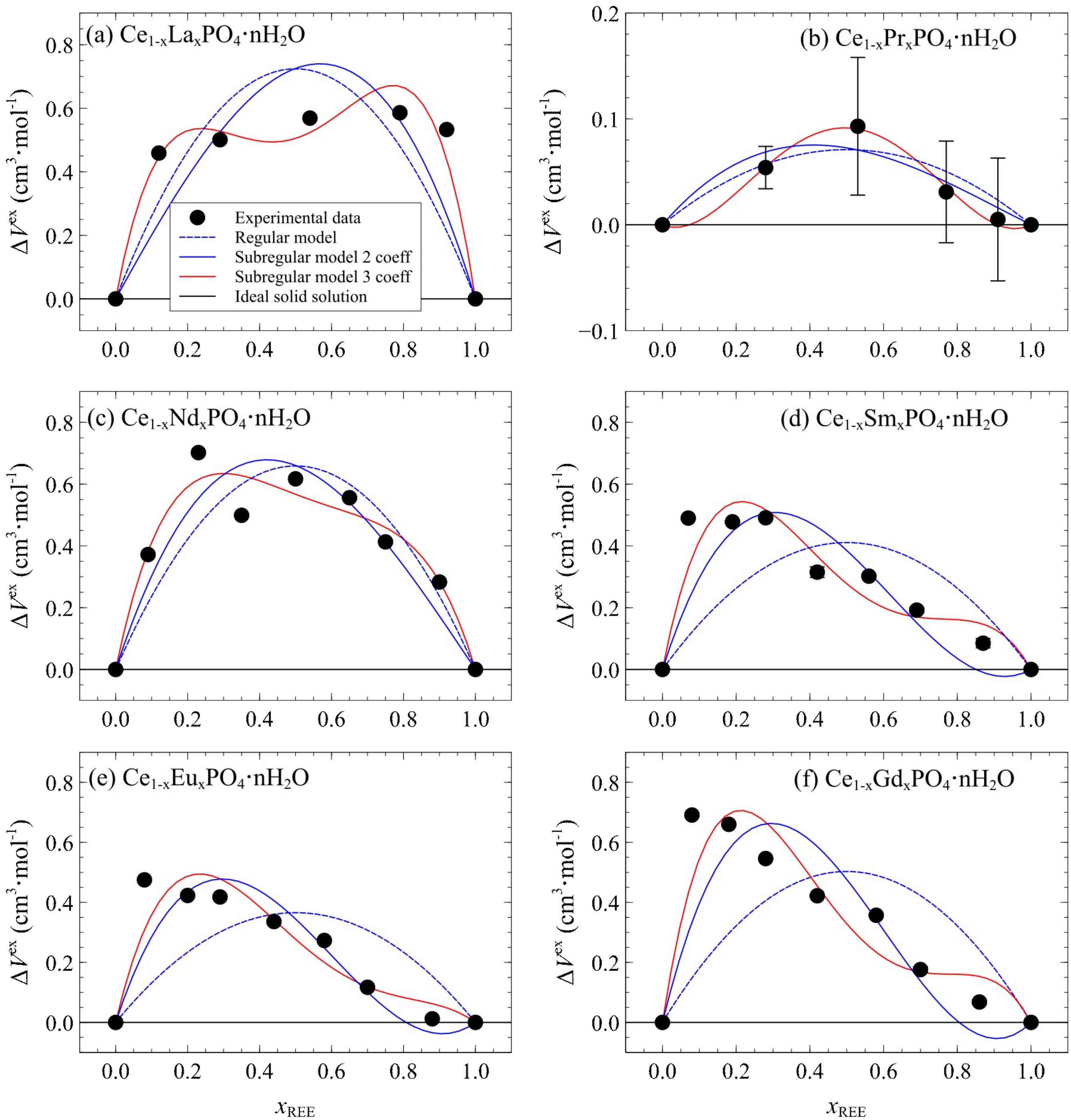

Figure 5. Excess volume of mixing (ΔV^{ex}) of binary rhabdophane solid solutions as a function of mole fraction REE (x_{REE}) in $Ce_{1-x}REE_xPO_4 \cdot nH_2O$ (REE= La, Pr, Nd, Sm, Eu, Gd). The experimental data are listed in Table 1 and the fits in Table 2.

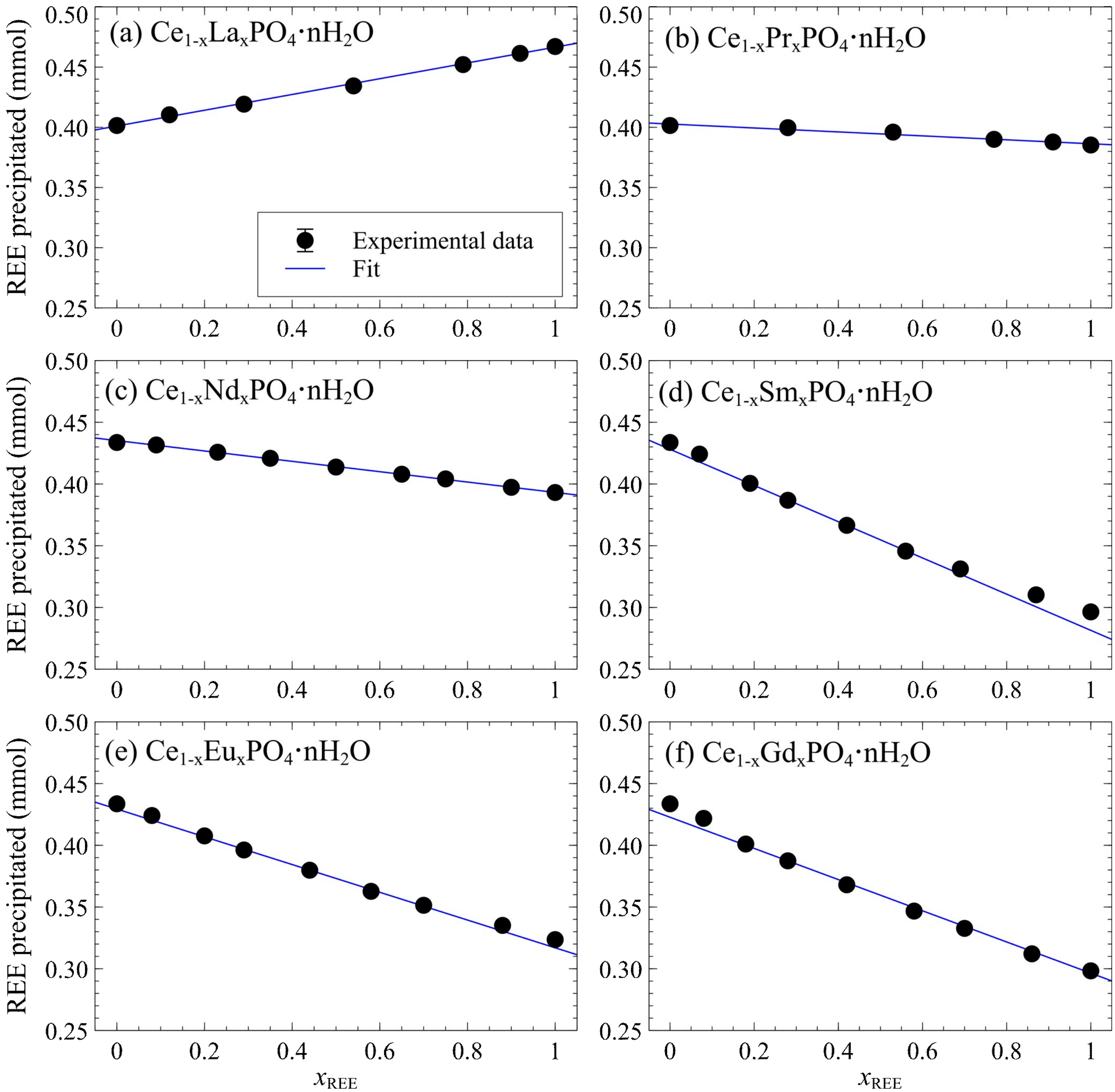

Figure 6. Amount of REE phosphates precipitated (in mmol) as a function of mole fraction REE (x_{REE}) in $Ce_{1-x}REE_xPO_4{\cdot}nH_2O$ (REE= La, Pr, Nd, Sm, Eu, Gd), determined from REE measured in the starting and final experimental solutions (Table 3).

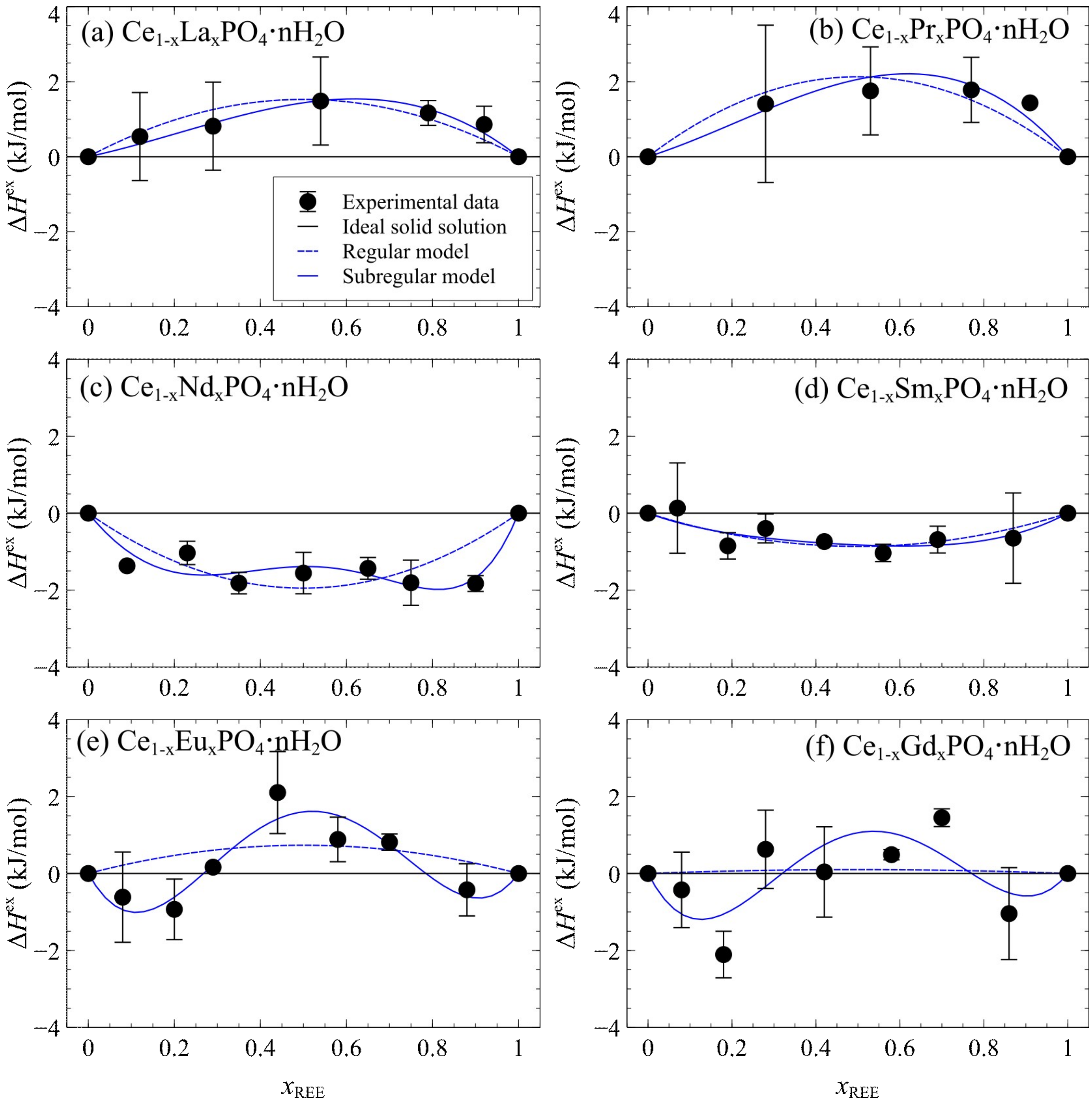

Figure 7. Excess enthalpies of mixing (ΔH^{ex} in kJ/mol) as a function of mole fraction REE (x_{REE}) in $Ce_{1-x}REE_xPO_4 \cdot nH_2O$ (REE= La, Pr, Nd, Sm, Eu, Gd) binary solid solution series determined using calorimetry. The error bars denote the standard deviations based on duplicate to quadruplicate experiments. The experimental data are listed in Table 3 and the fits in Table 4.

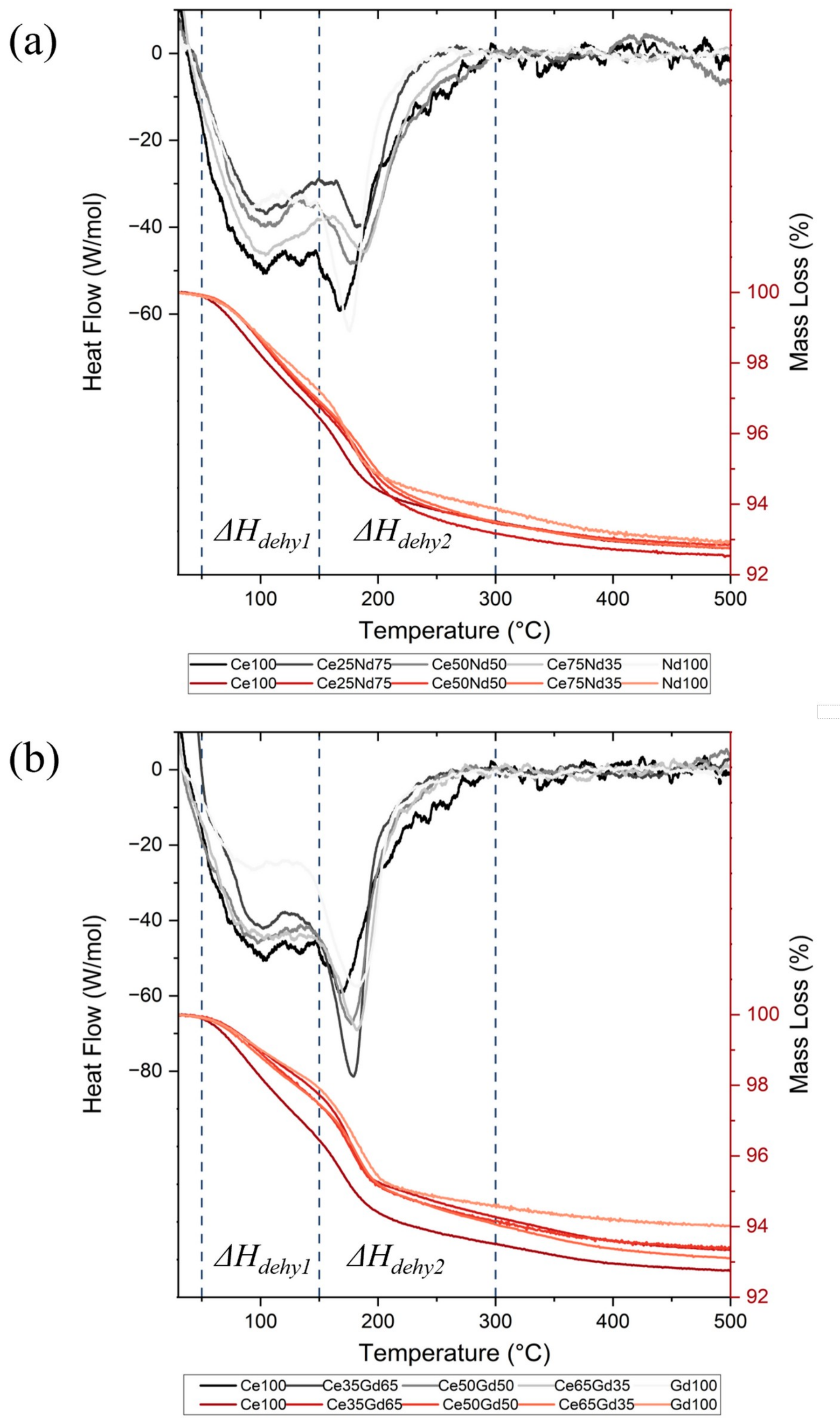

Figure 8. TGA-DSC analysis of binary (a) Ce-Nd and (b) Ce-Gd solid solutions from 30−500 °C. Integration bounds for enthalpy dehydration steps calculations are marked by the blue dashed lines. The integrated enthalpy and water contents are listed in Table 5.

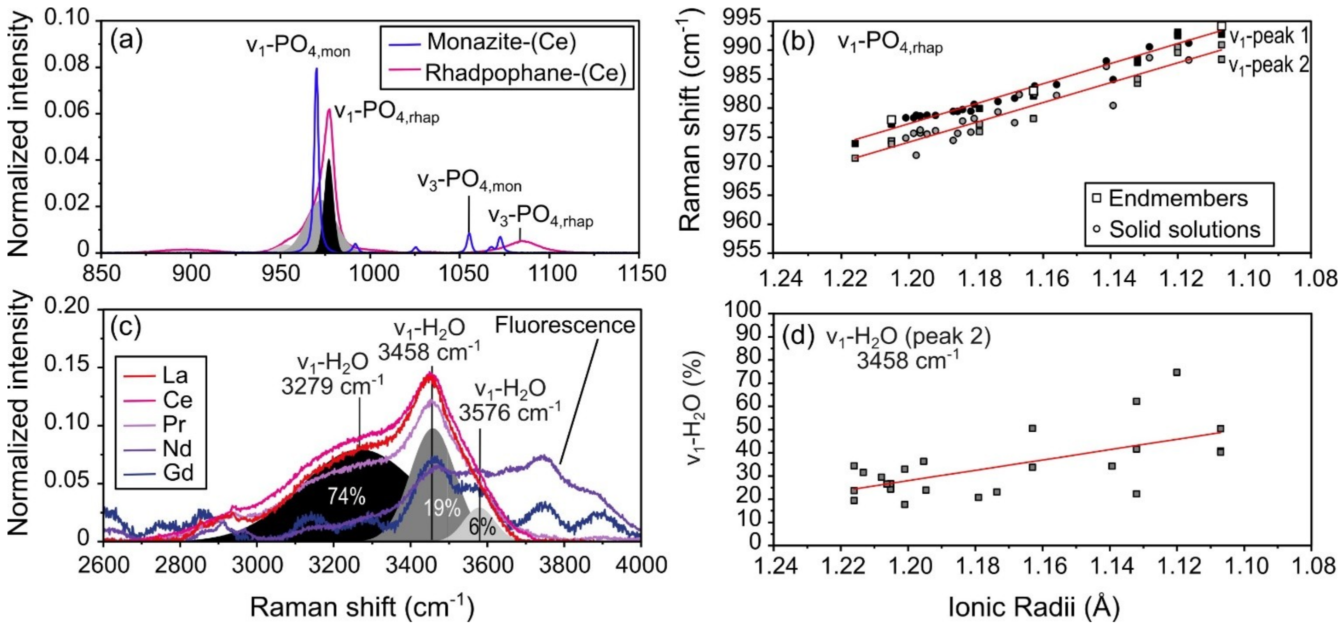

Figure 9. Raman spectra of: (a) symmetric (v_1) and asymmetric (v_3) vibrational phosphate stretching bands for monazite-(Ce) and rhabdophane-(Ce) endmembers; (b) peak center shift of the two main subpeaks of v_1-PO_4 in rhabdophane endmembers and solid solutions with decreasing ionic radii; (c) the vibrational stretching band for water in rhabdophane endmembers; (d) water subpeak area 2 (v_1-H_2O at 3458 cm^{-1}) increasing with decreasing ionic radii. White squares in (c) correspond to the Ce, Nd and Gd endmembers measured in previous studies (Clavier et al., 2018; Liu et al., 2022).

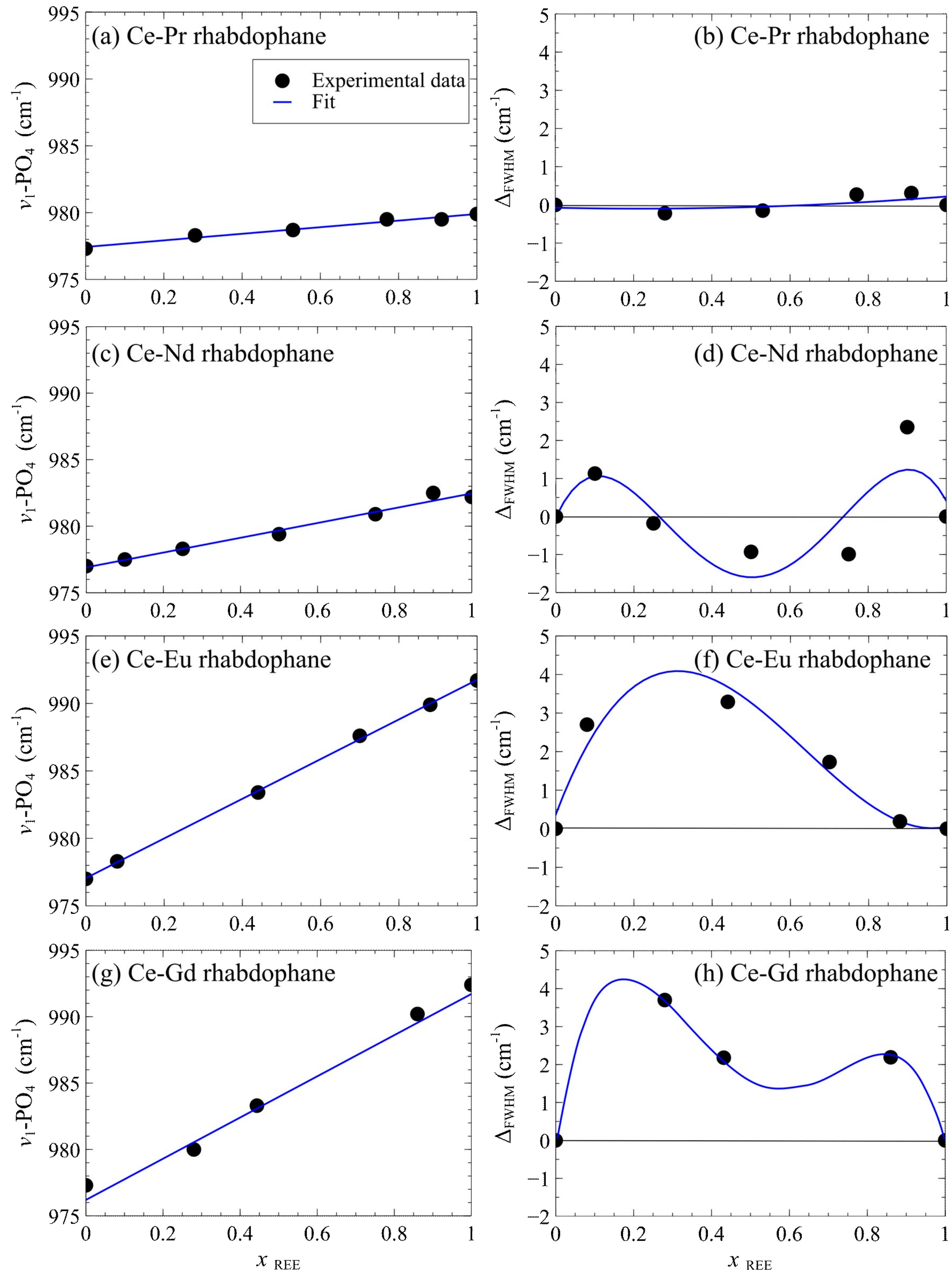

Figure 10. Raman spectra of symmetric vibrational phosphate stretching band shifts (v_1-PO_4) and full width at half maxima (FWHM) for binary (a,b) Ce-Pr, (c,d) Ce-Nd, (e,f) Ce-Eu and (g,h) Ce-Gd rhabdophane solid solutions. The Δ_{FWHM} values show the departure of FWHM for solid solutions from a linear interpolation between endmembers indicating non-ideal solid solution behavior due to short-range ordering.

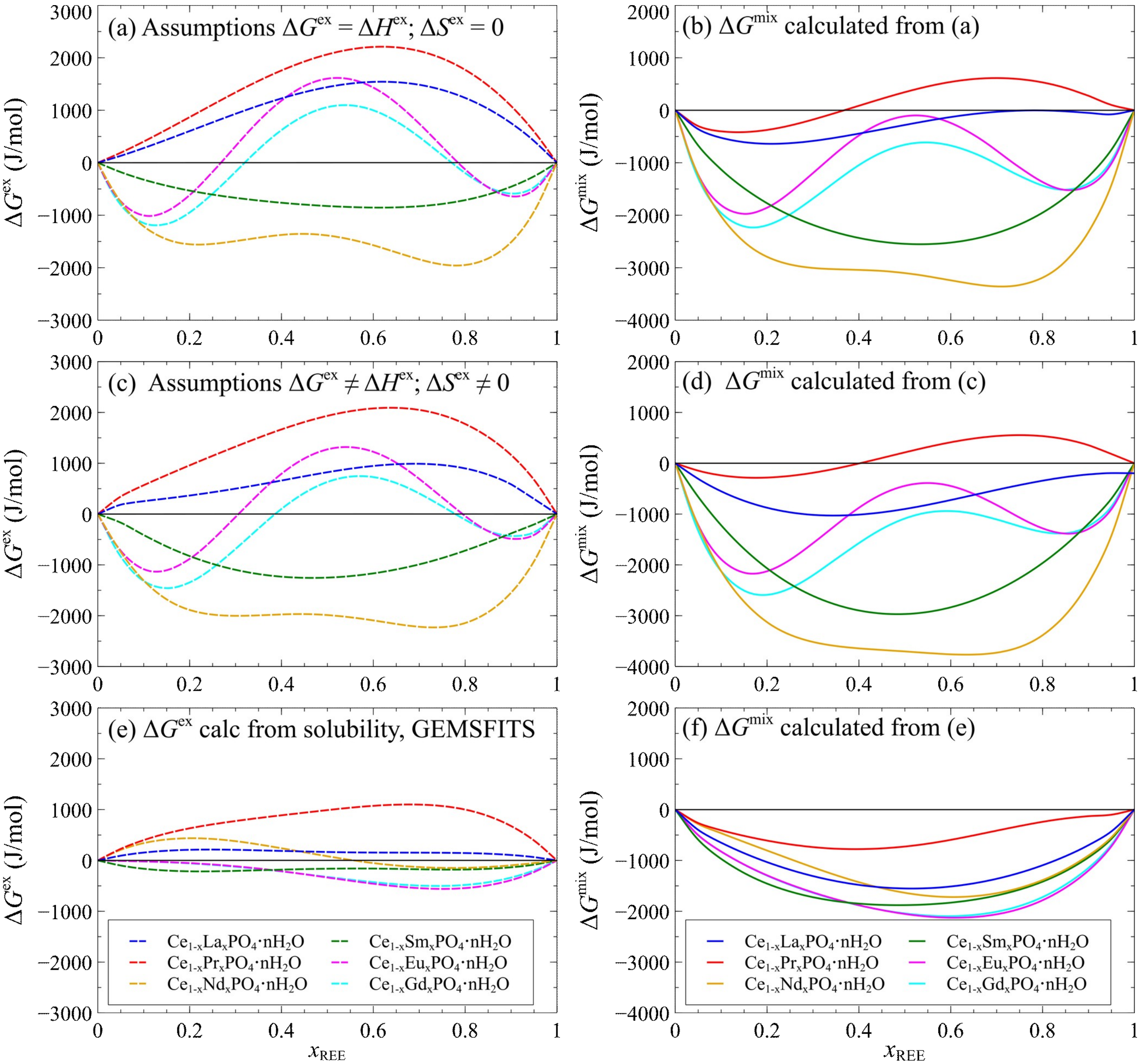

Figure 11. Excess Gibbs energy (ΔG^{ex}) and Gibbs energy of mixing (ΔG^{mix}) as a function of mole fraction REE (x_{REE}) in the rhabdophane solid solutions determined using three different approaches: (a-b) assuming disordering and random mixing with $\Delta G^{ex}=\Delta H^{ex}$ and $S^{ex}=0$ (section 4.1.1.); (c-d) assuming $S^{ex}\neq 0$, with entropy determined from molar volume data (section 4.1.2.); (e-f) ΔG^{ex} calculated from thermodynamic optimizations of solubility data using GEMSFITS and Aq-SS equilibria calculations (section 4.2.1.). Calculated Gibbs energy values are listed in the Supplementary Material Table S2.

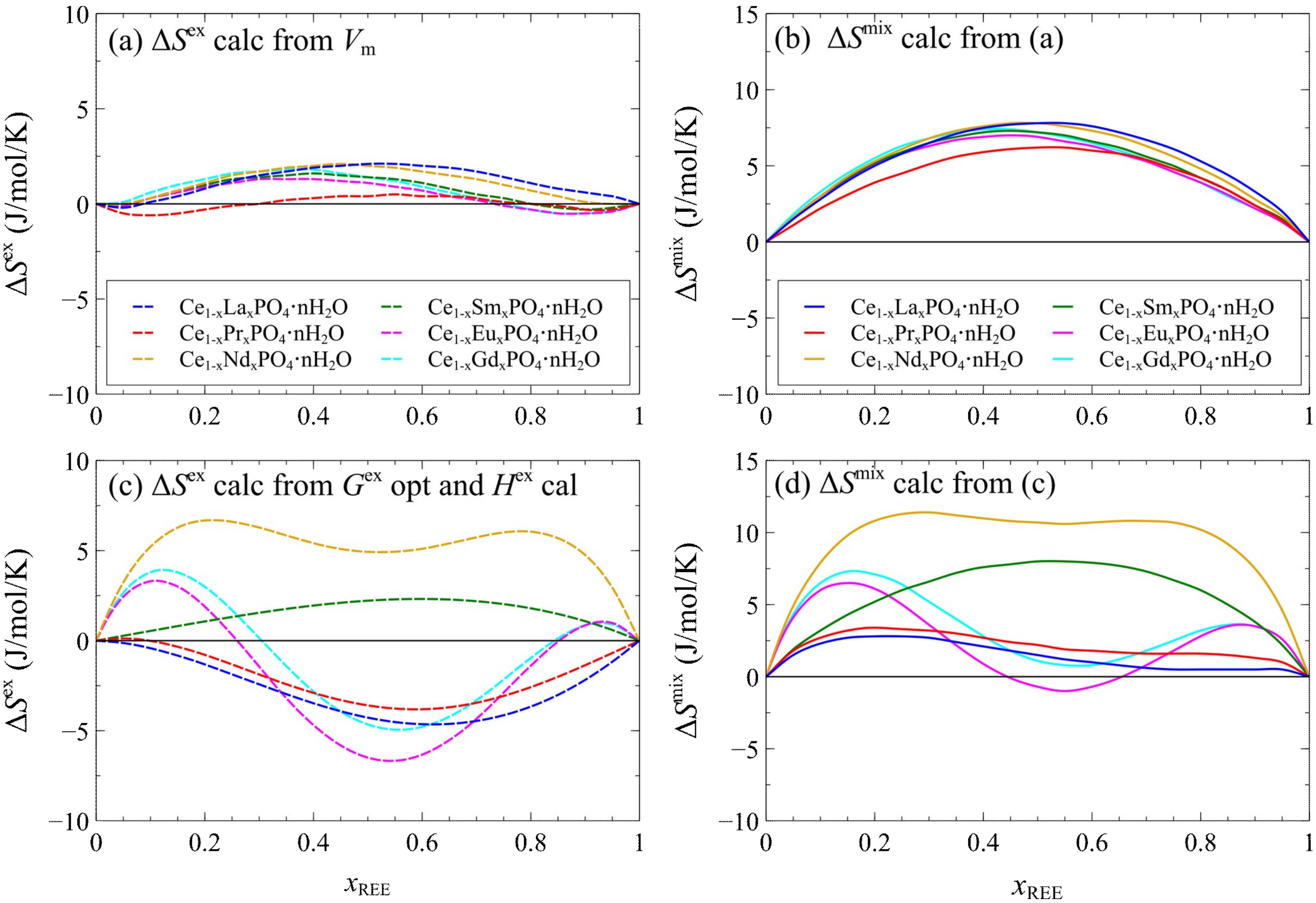

Figure 12. Excess entropy (ΔS^{ex}) and entropy of mixing (ΔS^{mix}) as a function of mole fraction REE (x_{REE}) in the rhabdophane solid solutions determined using two different approaches: (a-b) from XRD molar volume data (section 4.1.2.); (c-d) calculated using Eqs. 13 and 14 and the ΔG^{ex} calculated from thermodynamic optimizations of solubility data using GEMSFITS and Aq-SS equilibria calculations (section 4.2.1.). Calculated entropy values are listed in the Supplementary Material Tables S1 and S3.

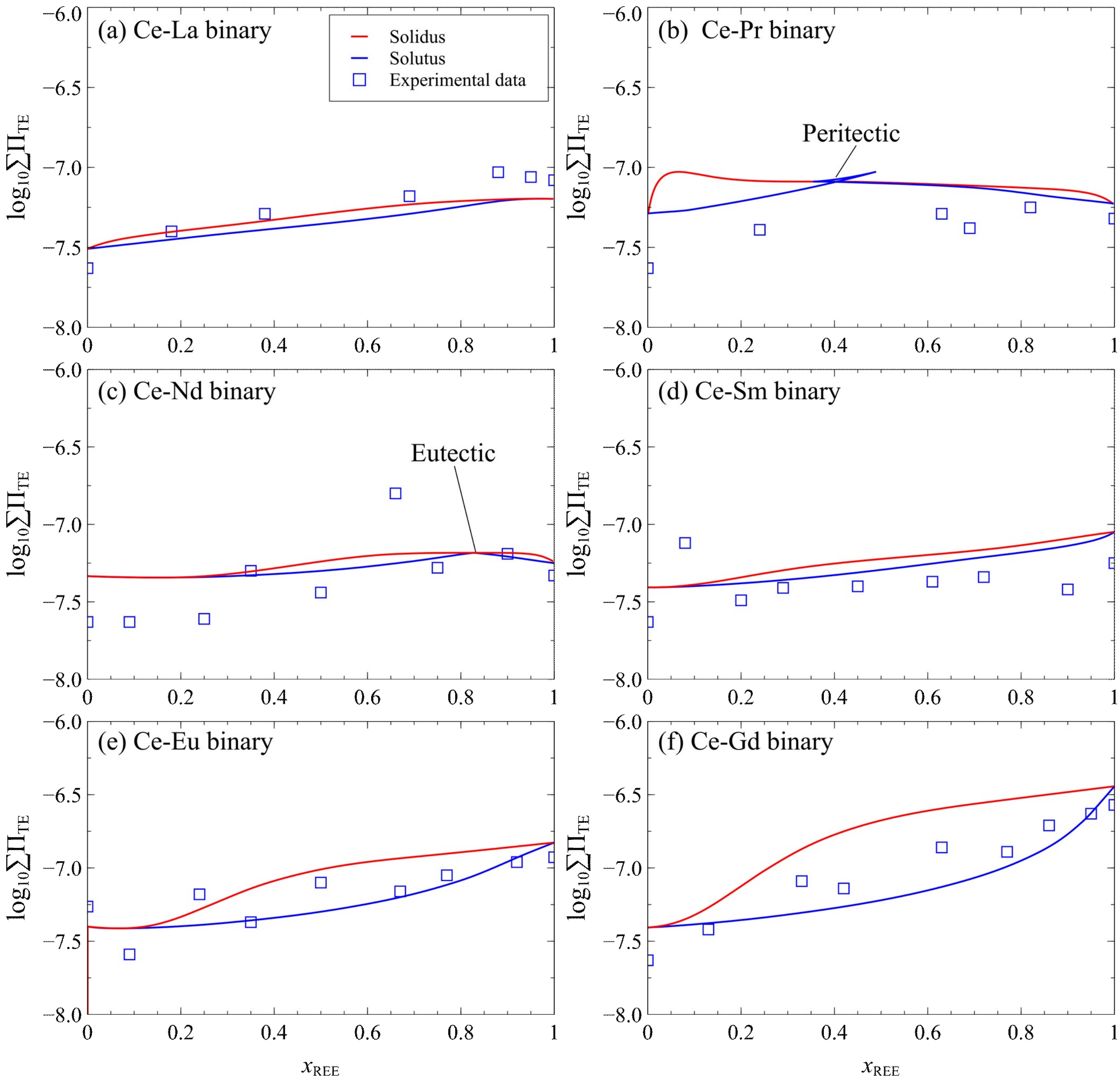

Figure 13. Lippmann diagrams (Eqs. 15-18) showing the logarithm of the total dissolved element (TE) solubility product (ΣΠ) as a function of mole fraction REE (x_{REE}) in the rhabdophane solid solutions. These diagrams were constructed using the GEMS code package (Kulik et al., 2013) process simulator and thermodynamic properties optimized using GEMSFITS (Miron et al., 2015) with parameters listed in Table 7. The computed "Solutus" curve indicates the REE composition of the aqueous solution and the "Solidus" curve the composition of the conjugate solid solution. The experimental data represent the REE concentrations measured in the experimental aqueous solutions.

Table 1. Refined crystal unit cell parameters (*a*, *b*, *c*, and *β*) of rhabdophane endmembers and binary solid solutions ($Ce_{1-X}REE_X$)$PO_4 \cdot nH_2O$, where *x* is the mole fraction REE (La, Pr, Nd, Sm, Eu, and Gd) in the solid solution. The molar volumes, V_{ss} for solid solutions and V_{cell} for endmembers (in $cm^3 \cdot mol^{-1}$) were calculated based on 24 formula units and the excess molar volume of mixing (ΔV^{ex}) was determined according to Eq. 2.

Run ID	*x*	1-*x*	*a* (Å)	±	*b* (Å)	±	*c* (Å)	±	*β* (°)	±	V_{ss}/V_{cell} ($Å^3$)	±	V_{ss}/V_{cell} ($cm^3 \cdot mol^{-1}$)	±	ΔV^{ex} ($cm^3 \cdot mol^{-1}$)	±
La100	1.00	-	28.579	0.008	6.904	0.002	12.434	0.003	115.55	0.03	2213	2	55.54	0.04	-	-
Ce100	-	1.00	28.456	0.009	6.889	0.002	12.321	0.003	115.48	0.03	2180	2	54.71	0.04	-	-
Pr100	1.00	-	28.371	0.028	6.869	0.005	12.289	0.009	115.52	0.10	2161	5	54.23	0.13	-	-
Nd100	1.00	-	28.261	0.010	6.848	0.002	12.237	0.003	115.64	0.03	2135	2	53.58	0.04	-	-
Sm100	1.00	-	28.085	0.005	6.829	0.001	12.155	0.002	115.44	0.01	2105	1	52.83	0.02	-	-
Eu100	1.00	-	27.998	0.008	6.804	0.002	12.132	0.004	115.77	0.02	2081	1	52.22	0.03	-	-
Gd100	1.00	-	27.947	0.011	6.786	0.002	12.086	0.004	115.79	0.03	2064	2	51.79	0.04	-	-
Ce-La binary																
Ce10La90	0.92	0.08	28.744	0.003	6.923	0.001	12.472	0.002	115.93	0.02	2232	1	56.01	0.03	0.533	0.011
Ce25La75	0.79	0.21	28.674	0.010	6.939	0.002	12.445	0.003	115.78	0.03	2230	2	55.95	0.04	0.586	0.007
Ce50La50	0.54	0.46	28.692	0.009	6.925	0.002	12.443	0.003	116.07	0.03	2221	2	55.73	0.04	0.569	0.002
Ce75La25	0.29	0.71	28.633	0.010	6.921	0.002	12.400	0.003	115.94	0.03	2210	2	55.45	0.04	0.501	0.006
Ce90La10	0.12	0.88	28.661	0.010	6.900	0.002	12.413	0.003	116.21	0.03	2203	2	55.27	0.04	0.459	0.006
Ce-Pr binary																
Ce75Pr25	0.28	0.72	28.421	0.002	6.870	0.002	12.361	0.008	115.56	0.02	2177	2	54.63	0.04	0.054	0.020
Ce50Pr50	0.53	0.47	28.384	0.024	6.872	0.002	12.352	0.023	115.55	0.10	2174	6	54.55	0.15	0.093	0.065
Ce25Pr75	0.77	0.23	28.370	0.010	6.874	0.005	12.316	0.009	115.57	0.02	2167	2	54.37	0.06	0.031	0.048
Ce10Pr90	0.91	0.09	28.357	0.004	6.874	0.003	12.298	0.009	115.54	0.04	2163	3	54.28	0.06	0.005	0.058
Ce-Nd binary																
Ce90Nd10	0.09	0.91	28.450	0.009	6.892	0.002	12.377	0.003	115.48	0.02	2191	1	54.98	0.04	0.372	0.003
Ce75Nd25	0.23	0.77	28.503	0.008	6.901	0.001	12.402	0.003	115.72	0.02	2198	1	55.15	0.03	0.702	0.008
Ce65Nd35	0.35	0.65	28.464	0.006	6.888	0.001	12.367	0.002	115.73	0.02	2184	1	54.81	0.03	0.499	0.013
Ce35Nd65	0.65	0.35	28.409	0.003	6.884	0.001	12.336	0.002	115.74	0.01	2173	1	54.53	0.02	0.556	0.025
Ce25Nd75	0.75	0.25	28.419	0.003	6.867	0.001	12.317	0.003	115.87	0.02	2163	1	54.27	0.03	0.413	0.016
Ce10Nd90	0.90	0.10	28.316	0.007	6.853	0.001	12.323	0.003	115.91	0.04	2151	2	53.97	0.04	0.283	0.002
Ce-Sm binary																

Ce90Sm10	0.07	0.93	28.605	0.009	6.888	0.002	12.387	0.003	115.96	0.03	2194	2	55.07	0.04	0.490	0.002
Ce75Sm25	0.19	0.81	28.527	0.008	6.892	0.001	12.345	0.003	115.81	0.02	2185	1	54.83	0.03	0.478	0.004
Ce65Sm35	0.28	0.72	28.511	0.009	6.882	0.002	12.336	0.003	115.83	0.03	2179	1	54.68	0.04	0.491	0.004
Ce50Sm50	0.42	0.58	28.412	0.011	6.876	0.002	12.286	0.004	115.77	0.03	2161	2	54.24	0.05	0.315	0.017
Ce35Sm65	0.56	0.44	28.374	0.007	6.859	0.001	12.280	0.003	115.86	0.02	2150	1	53.96	0.03	0.302	0.004
Ce25Sm75	0.69	0.31	28.296	0.008	6.846	0.002	12.243	0.003	115.73	0.02	2136	1	53.61	0.03	0.192	0.009
Ce10Sm90	0.87	0.13	28.168	0.009	6.835	0.002	12.190	0.003	115.49	0.03	2118	1	53.16	0.04	0.085	0.015
Ce-Eu binary																
Ce90Eu10	0.08	0.92	28.545	0.008	6.904	0.001	12.355	0.003	115.85	0.02	2191	1	54.99	0.03	0.475	0.004
Ce75Eu25	0.20	0.80	28.475	0.000	6.876	0.002	12.342	0.003	115.71	0.03	2177	1	54.64	0.04	0.423	0.001
Ce65Eu35	0.29	0.71	28.490	0.010	6.870	0.002	12.317	0.003	115.92	0.03	2168	2	54.41	0.04	0.418	0.004
Ce50Eu50	0.44	0.56	28.337	0.005	6.867	0.002	12.260	0.003	115.69	0.01	2150	1	53.95	0.02	0.336	0.015
Ce35Eu65	0.58	0.42	28.325	0.007	6.841	0.001	12.227	0.003	115.76	0.02	2134	1	53.54	0.03	0.273	0.009
Ce25Eu75	0.70	0.30	28.199	0.010	6.835	0.002	12.183	0.003	115.71	0.03	2116	2	53.09	0.04	0.117	0.007
Ce10Eu90	0.88	0.12	28.101	0.011	6.810	0.002	12.141	0.004	115.70	0.04	2094	2	52.53	0.05	0.012	0.013
Ce-Gd binary																
Ce90Gd10	0.08	0.92	28.585	0.008	6.899	0.001	12.386	0.003	115.83	0.02	2198	1	55.17	0.03	0.691	0.006
Ce75Gd25	0.18	0.82	28.543	0.009	6.887	0.002	12.358	0.003	115.89	0.03	2186	2	54.84	0.04	0.660	0.001
Ce65Gd35	0.28	0.72	28.470	0.009	6.876	0.002	12.312	0.003	115.83	0.03	2169	1	54.44	0.04	0.546	0.003
Ce50Gd50	0.42	0.58	28.370	0.010	6.857	0.002	12.269	0.003	115.84	0.03	2148	2	53.91	0.04	0.422	0.002
Ce35Gd65	0.58	0.42	28.278	0.009	6.827	0.002	12.238	0.003	115.81	0.03	2127	2	53.37	0.04	0.357	0.003
Ce25Gd75	0.70	0.30	28.154	0.012	6.819	0.002	12.176	0.004	115.74	0.04	2106	2	52.84	0.05	0.176	0.009
Ce10Gd90	0.86	0.14	28.063	0.012	6.785	0.002	12.152	0.004	115.82	0.04	2083	2	52.27	0.05	0.068	0.007

Table 2. Fitted coefficients (a_0-a_3, in cm^3/J) for the Guggenheim function (Eq. 9) relating excess molar volume of mixing (ΔV^{ex}) and mole fraction REE (x). The R^2 linear regression coefficients indicate that the asymmetric 3-term Guggenheim function most accurately reproduces the experimental ΔV^{ex} values derived in this study.

	1-coeff		**2-coeff**			**3-coeff**			
Rhabdophane binary	$a_0\times10^3$	R^2	$a_0\times10^3$	$a_1\times10^3$	R^2	$a_0\times10^3$	$a_1\times10^3$	$a_2\times10^3$	R^2
Ce-La	1.17	0.59	1.17	0.34	0.64	0.82	0.29	1.92	0.95
Ce-Pr	0.11	0.83	0.12	-0.05	0.87	0.15	-0.01	-0.21	0.99
Ce-Nd	1.06	0.80	1.07	-0.36	0.86	0.92	-0.36	1.01	0.94
Ce-Sm	0.66	0.16	0.62	-0.89	0.68	0.45	-0.80	1.22	0.87
Ce-Eu	0.59	0.20	0.56	-0.91	0.79	0.45	-0.85	0.76	0.86
Ce-Gd	0.81	0.07	0.77	-1.26	0.69	0.53	-1.14	1.56	0.86

Table 3. Dissolved REE and P concentrations (in mmol/kg and μmol/kg) before (initial) and after precipitation (final) of rhabdophane measured in the experimental aqueous solutions using ICP-OES and ICP-MS. Enthalpy of precipitation (ΔH^{ppt}) and excess enthalpy of mixing (ΔH^{ex}) were measured at room temperature and 1 bar using calorimetry. The amount of rhabdophane precipitated (REE_{ppt}) was calculated from initial/final REE concentrations in the fluid. The mole fractions (x) of REE corresponds to the composition of the precipitated binary rhabdophane solid solutions ($Ce_xREE_{1-x}PO_4 \cdot nH_2O$).

Run ID	x	1-x	$Ce_{initial}$ (mmol/kg)	Ce_{final} (μmol/kg)	$REE_{initial}$ (mmol/kg)	REE_{final} (μmol/kg)	$P_{initial}$ (mmol/kg)	$^{a}P_{final,calc}$ (mmol/kg)	REE_{ppt} (mmol)	ΔH_{ppt} (kJ/mol)	1σ[b]	ΔH^{ex} (kJ/mol)	1σ[b]
Endmembers													
La100	1.00	-	-	-	4.58	2.16	42.86	38.28	0.467	34.59	-	-	-
Ce100	-	1.00	4.25	0.61	-	-	42.86	38.61	0.434	33.20	0.11	-	-
Pr100	1.00	-	-	-	3.78	1.23	43.12	39.34	0.385	36.87	-	-	-
Nd100	1.00	-	-	-	3.86	1.36	38.03	34.18	0.393	38.76	0.93	-	-
Sm100	1.00	-	-	-	2.91	1.40	43.32	40.42	0.296	38.95	-	-	-
Eu100	1.00	-	-	-	3.18	2.81	44.56	41.38	0.324	36.83	0.90	-	-
Gd100	1.00	-	-	-	2.93	6.68	43.05	40.12	0.298	44.13	0.85	-	-
Ce-La binary													
Ce90La10	0.12	0.88	3.54	0.83	0.48	0.19	42.86	38.84	0.410	33.90	-	0.54	-
Ce75La25	0.29	0.71	2.95	0.82	1.16	0.51	42.86	38.75	0.419	34.41	-	0.81	-
Ce50La50	0.54	0.46	1.98	0.53	2.28	1.17	43.12	38.86	0.434	35.43	-	1.48	-
Ce25La75	0.79	0.21	0.99	0.30	3.44	2.09	43.12	38.69	0.452	35.46	0.33	1.17	0.33
Ce10La90	0.92	0.08	0.39	0.12	4.13	2.13	43.12	38.60	0.461	35.34	0.49	0.86	0.49
Ce-Pr binary													
Ce75Pr25	0.28	0.72	2.95	0.33	0.97	0.74	43.11	39.19	0.400	35.62	2.10	1.41	2.10
Ce50Pr50	0.53	0.47	1.98	0.79	1.90	0.25	43.29	39.41	0.396	36.91	-	1.76	-
Ce25Pr75	0.77	0.23	0.99	0.47	2.84	0.82	43.30	39.48	0.390	37.82	0.87	1.78	0.87
Ce10Pr90	0.91	0.09	0.40	0.26	3.41	1.17	43.30	39.50	0.388	37.98	0.01	1.44	0.01
Ce-Nd binary													
Ce90Nd10	0.09	0.91	3.84	0.63	0.39	0.07	38.03	33.80	0.432	32.33	0.06	-1.37	0.06
Ce75Nd25	0.23	0.77	3.20	0.55	0.97	0.18	38.03	33.86	0.426	33.45	0.30	-1.03	0.30
Ce65Nd35	0.35	0.65	2.77	0.85	1.35	0.45	43.19	39.07	0.421	33.33	0.28	-1.82	0.28
Ce50Nd50	0.50	0.50	2.13	0.47	1.93	0.46	43.05	38.99	0.414	34.43	0.54	-1.56	0.54
Ce35Nd65	0.65	0.35	1.50	1.40	2.51	2.67	43.19	39.19	0.408	35.38	0.28	-1.43	0.28
Ce25Nd75	0.75	0.25	1.07	0.33	2.89	1.00	43.11	39.15	0.404	35.57	0.59	-1.81	0.59
Ce10Nd90	0.90	0.10	0.43	0.16	3.47	1.47	43.11	39.21	0.397	36.38	0.21	-1.83	0.21
Ce-Sm binary													
Ce90Sm10	0.07	0.93	3.84	1.82	0.29	0.15	43.08	38.93	0.424	33.73		0.13	

Ce75Sm25	0.19	0.81	3.20	0.66	0.73	0.16	43.32	39.40	0.400	33.44	0.34	-0.85	0.34
Ce65Sm35	0.28	0.72	2.78	0.70	1.02	0.28	43.08	39.29	0.387	34.41	0.38	-0.40	0.38
Ce50Sm50	0.42	0.58	2.14	0.55	1.45	0.46	42.48	38.89	0.366	34.88	0.02	-0.74	0.02
Ce35Sm65	0.56	0.44	1.50	0.41	1.89	0.65	43.08	39.69	0.346	35.38	0.23	-1.03	0.23
Ce25Sm75	0.69	0.31	1.07	0.32	2.18	0.84	42.48	39.23	0.331	36.48	0.35	-0.69	0.35
Ce10Sm90b	0.87	0.13	0.42	0.10	2.62	0.86	42.48	39.44	0.310	37.55	-	-0.65	-
Ce-Eu binary													
Ce90Eu10	0.08	0.92	3.84	0.61	0.32	0.06	43.08	38.93	0.424	32.87	-	-0.62	-
Ce75Eu25	0.20	0.80	3.20	1.24	0.79	0.40	44.55	40.56	0.408	32.99	0.79	-0.93	0.79
Ce65Eu35	0.29	0.71	2.78	0.70	1.11	0.38	43.19	39.31	0.396	34.42	0.00	0.16	0.00
Ce50Eu50	0.44	0.56	2.13	0.99	1.59	1.00	43.22	39.50	0.380	36.90	1.07	2.10	1.07
Ce35Eu65	0.58	0.42	1.49	0.58	2.06	1.16	43.19	39.64	0.363	36.19	0.58	0.88	0.58
Ce25Eu75	0.70	0.30	1.07	0.52	2.38	1.73	43.11	39.66	0.351	36.56	0.21	0.82	0.21
Ce10Eu90	0.88	0.12	0.43	0.24	2.86	2.54	43.11	39.82	0.335	35.97	0.68	-0.42	0.68
Ce-Gd binary													
Ce90Gd10	0.08	0.92	3.84	0.84	0.29	0.13	43.08	38.95	0.422	33.36	0.57	-0.43	0.98
Ce75Gd25	0.18	0.82	3.20	1.40	0.73	0.68	43.05	39.12	0.401	33.06	0.60	-2.11	0.60
Ce65Gd35	0.28	0.72	2.77	1.07	1.03	0.76	43.19	39.39	0.387	36.89	1.02	0.63	1.02
Ce50Gd50	0.42	0.58	2.13	1.27	1.48	2.17	43.34	39.73	0.368	37.83	-	0.04	-
Ce35Gd65	0.58	0.42	1.50	0.73	1.91	2.51	43.19	39.79	0.347	40.03	0.13	0.49	0.13
Ce25Gd75	0.70	0.30	1.07	0.70	2.20	4.21	43.34	40.08	0.333	42.30	0.23	1.45	0.23
Ce10Gd90	0.86	0.14	0.43	0.27	2.64	5.60	43.34	40.28	0.312	41.55	1.20	-1.04	1.20

[a] Calculated from amounts of REE precipitated and initial P concentrations.

[b] Standard deviation calculated based on duplicates to quadruplicates experiments.

Table 4. Fitted coefficients (a_0-a_3) for the Guggenheim function relating excess enthalpy of mixing (ΔH^{ex}) and mole fraction REE according to Eq. 10.

	1-coeff		**2-coeff**			**3-coeff**			
rhabdophane binary	$a_0 \times 10^3$	R^2	$a_0 \times 10^3$	$a_1 \times 10^3$	R^2	$a_0 \times 10^3$	$a_1 \times 10^3$	$a_2 \times 10^3$	R^2
Ce-La	2.47	0.68	2.32	1.33	0.82	-	-	-	-
Ce-Pr	3.44	0.36	3.33	1.90	0.45	-	-	-	-
Ce-Nd	-3.14	0.41	-3.14	-0.78	0.44	-2.23	-0.84	-6.05	0.75
Ce-Sm	-1.39	0.58	-1.41	-0.30	0.59	-1.33	-0.38	-0.65	0.60
Ce-Eu	1.19	0.19	1.23	1.43	0.25	2.59	1.03	-9.79	0.70
Ce-Gd	0.16	-0.01	0.20	2.38	0.12	1.71	1.58	-8.76	0.40

Table 5. Results from the TGA-DSC experiments between 25 and 500 °C showing a comparison of the first (ΔH_{dehy1}), second (ΔH_{dehy2}), and overall (ΔH_{dehy}) dehydration enthalpies and atom per formula units rhabdophane (apfu) of H_2O derived from the dehydration reactions. Water contents from this study and literature values for end-member Ce, Nd, and Gd rhabdophanes are also listed.

	(this study)				[Sh18][1]		[Och17][2]	[Anf14][3]
Run ID	ΔH_{dehy1} (kJ/mol H_2O)	ΔH_{dehy2} (kJ/mol H_2O)	ΔH_{dehy} (kJ/mol H_2O)	$n H_2O$ (apfu)	ΔH_{dehy} (kJ/mol)	$n H_2O$ (apfu)	$n H_2O$ (apfu)	$n H_2O$ (apfu)
Ce100	103.1	101.7	96.5	0.96	68.3	0.73	1.71	-
Nd100	92.5	63.5	73.6	0.96	67.2	0.75	1.76	1.20
Gd100	91.4	72.8	95.6	0.85	86.1	0.53	1.96	0.80
Ce25Nd75	76.4	51.0	58.6	1.01	-	-	-	-
Ce50Nd50	86.8	84.4	91.9	0.96	-	-	-	-
Ce75Nd35	105.4	74.7	84.8	0.97	-	-	-	-
Ce35Gd65	122.0	79.1	100.0	0.93	-	-	-	-
Ce50Gd50	127.7	83.0	97.2	1.09	-	-	-	-
Ce65Gd35	132.8	86.4	104.3	0.95	-	-	-	-

[1]Shelyug et al. (2018); [2]Ochiai et al. (2017); [3]Anfimova et al. (2014).

Table 6. Raman spectroscopy of rhabdophane solid solutions showing the peak centers and the full width half maximum (FWHM) of the symmetrical v_1 stretching vibration band of the PO_4 tetrahedron.

Solid solution	x_{REE}	v_1-PO_4 cm^{-1}	±	FWHM-v_1 cm^{-1}	±	[a]$FWHM_{calc}$ cm^{-1}	[b]Δ_{FWHM} cm^{-1}
Ce-Pr binary	0	977.3	0.5	5.59	0.27	5.59	0
	0.28	978.3	0.5	5.28	0.27	5.50	-0.22
	0.53	978.7	0.5	5.28	0.27	5.43	-0.15
	0.77	979.5	0.5	5.63	0.27	5.36	0.27
	0.91	979.5	0.5	5.62	0.27	5.31	0.31
	1	979.9	0.5	5.29	0.27	5.29	0
Ce-Nd binary	0	977.0	0.5	6.17	0.27	6.17	0
	0.10	977.5	0.5	7.75	0.27	6.62	1.13
	0.25	978.3	0.5	7.12	0.27	7.30	-0.18
	0.50	979.4	0.5	7.49	0.27	8.43	-0.93
	0.75	980.9	0.5	8.56	0.27	9.56	-0.99
	0.90	982.5	0.5	12.6	0.27	10.23	2.35
	1	982.2	0.5	10.7	0.27	10.68	0
Ce-Eu binary	0	977.0	0.5	6.13	0.27	6.13	0
	0.08	978.3	0.5	9.18	0.27	6.48	2.70
	0.44	983.4	0.5	11.4	0.27	8.08	3.29
	0.70	987.6	0.5	11.0	0.27	9.23	1.73
	0.88	989.9	0.5	10.2	0.27	10.03	0.19
	1	991.7	0.5	10.6	0.27	10.57	0
Ce-Gd binary	0	977.3	0.5	5.92	0.27	5.92	0
	0.28	980.0	0.5	10.3	0.27	6.59	3.70
	0.42	983.3	0.5	9.11	0.27	6.93	2.18
	0.86	990.2	0.5	10.2	0.27	7.99	2.19
	1	992.4	0.5	8.32	0.27	8.32	0

[a] Calculated from linear interpolation of rhabdophane endmember FWHM-v_1 values.

[b] Difference calculated by subtracting $FWHM_{calc}$ values from measured rhabdophane solid solution FWHM values.

Table 7. Optimized standard Gibbs energy of formation (ΔfG_{opt}) of rhabdophane endmembers and binary solid solution interaction coefficients using a 3-term Guggenheim function (a_0, a_1, and a_2) for determination of the excess Gibbs energy (ΔG^{ex}) according to Eq. 6 and activity coefficients according to Eqs. 7 and 8.

	[a]$\Delta fG^o_{initial}$ (J/mol)	[b]± (J/mol)	ΔfG^o_{opt} (J/mol)	[c]± (J/mol)	[d]Δ (J/mol)	a_0	[c]±	a_1	[c]±	a_2	[c]±
rhabdophane-(Ce)	-2,012,495	5,000	-2,001,517	504	10,978	-0.54	0.41	-1.03	0.56	-0.58	0.97
rhabdophane-(Eu)	-1,867,033	10,000	-1,854,966	409	12,067						
rhabdophane-(Ce)	-2,012,495	5,000	-2,000,871	572	11,624	-0.52	0.46	-0.89	0.66	-0.43	0.86
rhabdophane-(Gd)	-1,951,506	2,000	-1,936,636	424	14,869						
rhabdophane-(Ce)	-2,012,495	5,000	-2,002,766	588	9,729	0.13	0.55	-1.23	0.78	0.65	1.38
rhabdophane-(Nd)	-2,012,677	3,000	-2,000,783	531	11,894						
rhabdophane-(Ce)	-2,012,495	5,000	-2,004,023	121	8,472	1.60	0.21	0.78	0.28	1.28	0.55
rhabdophane-(Pr)	-2,013,411	5,000	-2,000,317	141	13,093						
rhabdophane-(Ce)	-2,012,495	5,000	-2,002,253	355	10,243	-0.26	0.38	0.08	0.51	-0.64	0.04
rhabdophane-(Sm)	-1,979,169	7,000	-1,966,614	336	12,555						
rhabdophane-(Ce)	-2,012,495	5,000	-2,003,183	207	9,313	0.27	0.15	-0.13	0.19	0.50	0.38
rhabdophane-(La)	-2,037,235	3,000	-2,028,839	104	8,396						

[a] Initial standard Gibbs energy of formation ($\Delta fG_{initial}$) of rhabdophane calculated based on the rhabdophane solubility products ($\log K_{sp}$) derived in the solubility study from Gausse et al. (2016) and internally consistent with the aqueous REE^{3+}, PO_4^{3-} and $H_2O(aq)$ species implemented in the MINES thermodynamic database (Gysi et al., 2023). These values are also consistent within those reported by Shelyug et al. (2018).

[b] Uncertainties reported by Gausse et al. (2016) for Gibbs energies of rhabdophane dissolution based on $\log K_{sp}$ values reported from the solubility experiments.

[c] Calculated uncertainties of the optimizations based on 200 Monte Carlo simulations in GEMSFITS (Miron et al., 2015).

[d] Difference between $\Delta fG_{initial}$ and ΔfG_{opt}.

SUPPLEMENTARY MATERIAL

Reaction calorimetry and structural crystal properties of non-ideal binary rhabdophane solid solutions ($Ce_{1-x}REE_xPO_4 \cdot nH_2O$)

Alexander P. Gysi[*a,b], Nicole C. Hurtig[b], Hannah Juan Han[a], Emma C. Kindall[c], Xiaofeng Guo[c], Dmitrii A. Kulik[d], George Dan Miron[d]

[a] New Mexico Bureau of Geology and Mineral Resources, New Mexico Institute of Mining and Technology, 801 Leroy Place, Socorro, NM 87801, USA

[b] Department of Earth and Environmental Science, New Mexico Institute of Mining and Technology, 801 Leroy Place, Socorro, NM 87801, USA

[c] Department of Chemistry, Washington State University, Pullman, WA 99164, USA

[d] Paul Scherrer Institute, Laboratory for Waste Management, Villigen PSI 5232, Switzerland

REVISION 1

* Corresponding author: e-mail, alexander.gysi@nmt.edu

Tel: +1 575-835-5754

To be submitted to GCA, for the Special Issue "Hydrothermal Geochemistry and Beyond: A Tribute to Terry M. Seward"

Table S1. Estimated excess entropy based on XRD data from the vibrational entropy term ($\Delta S^{mix,vib}$) and calculated configurational entropy term ($\Delta S^{mix,ideal}$). The entropy of mixing (ΔS^{mix}) was calculated according to Eq. 14 and other terms are described in section 4.1.2.

Run ID	x	1-x	$\Delta S^{mix,vib}$ J mol^{-1}K^{-1}	±	$\Delta S^{mix,\ ideal}$ J mol^{-1}K^{-1}	ΔS^{mix} J mol^{-1}K^{-1}
Ce-La binary						
Ce10La90	0.92	0.08	1.31	2.34	2.29	3.60
Ce25La75	0.79	0.21	1.44	2.34	4.30	5.74
Ce50La50	0.54	0.46	1.40	2.34	5.74	7.14
Ce75La25	0.29	0.71	1.24	2.35	4.98	6.22
Ce90La10	0.12	0.88	1.13	2.35	3.06	4.19
Ce-Pr binary						
Ce75Pr25	0.28	0.72	0.13	2.32	4.90	5.04
Ce50Pr50	0.53	0.47	0.23	2.31	5.74	5.97
Ce25Pr75	0.77	0.23	0.08	2.31	4.45	4.53
Ce10Pr90	0.91	0.09	0.01	2.30	2.52	2.53
Ce-Nd binary						
Ce90Nd10	0.09	0.91	0.92	2.32	2.52	3.43
Ce75Nd25	0.23	0.77	1.73	2.33	4.48	6.21
Ce65Nd35	0.35	0.65	1.23	2.32	5.38	6.61
Ce35Nd65	0.65	0.35	1.37	2.30	5.38	6.75
Ce25Nd75	0.75	0.25	1.02	2.29	4.68	5.69
Ce10Nd90	0.90	0.10	0.70	2.28	2.70	3.40
Ce-Sm binary						
Ce90Sm10	0.07	0.93	1.23	2.33	2.11	3.34
Ce75Sm25	0.19	0.81	1.25	2.32	4.04	5.29
Ce65Sm35	0.28	0.72	1.31	2.31	4.93	6.24
Ce50Sm50	0.42	0.58	0.93	2.29	5.66	6.59
Ce35Sm65	0.56	0.44	0.95	2.28	5.70	6.65
Ce25Sm75	0.69	0.31	0.73	2.27	5.15	5.87
Ce10Sm90	0.87	0.13	0.53	2.25	3.21	3.74
Ce-Eu binary						
Ce90Eu10	0.08	0.92	1.17	2.32	2.32	3.49
Ce75Eu25	0.20	0.80	1.04	2.31	4.16	5.20
Ce65Eu35	0.29	0.71	1.03	2.30	5.01	6.03
Ce50Eu50	0.44	0.56	0.83	2.28	5.70	6.53
Ce35Eu65	0.58	0.42	0.67	2.27	5.66	6.33
Ce25Eu75	0.70	0.30	0.29	2.25	5.08	5.37
Ce10Eu90	0.88	0.12	0.03	2.23	3.05	3.08
Ce-Gd binary						
Ce90Gd10	0.08	0.92	1.70	2.33	2.32	4.02
Ce75Gd25	0.18	0.82	1.62	2.31	3.92	5.54
Ce65Gd35	0.28	0.72	1.34	2.30	4.93	6.27
Ce50Gd50	0.42	0.58	1.04	2.28	5.66	6.70
Ce35Gd65	0.58	0.42	0.88	2.26	5.66	6.53
Ce25Gd75	0.70	0.30	0.43	2.24	5.08	5.51
Ce10Gd90	0.86	0.14	0.17	2.22	3.37	3.54

Table S2. Calculated excess Gibbs energy (ΔG^{ex}) and Gibbs energy of mixing (ΔG^{mix}) based on the three approaches presented in sections 4.1. and 4.2. with curves shown in Figure 11.

1) $\Delta G^{ex} = \Delta H^{ex}$

x_{REE}	ΔG^{ex}_Ce-La (J/mol)	ΔG^{ex}_Ce-Pr (J/mol)	ΔG^{ex}_Ce-Nd (J/mol)	ΔG^{ex}_Ce-Sm (J/mol)	ΔG^{ex}_Ce-Eu (J/mol)	ΔG^{ex}_Ce-Gd (J/mol)	ΔG^{mix}_Ce-La (J/mol)	ΔG^{mix}_Ce-Pr (J/mol)	ΔG^{mix}_Ce-Nd (J/mol)	ΔG^{mix}_Ce-Sm (J/mol)	ΔG^{mix}_Ce-Eu (J/mol)	ΔG^{mix}_Ce-Gd (J/mol)
0.00	0	0	0	0	0	0	0	0	0	0	0	0
0.05	132	191	-752	-179	-738	-802	-360	-301	-1244	-671	-1230	-1294
0.10	280	404	-1214	-323	-1004	-1151	-525	-402	-2020	-1129	-1810	-1957
0.15	439	632	-1459	-438	-926	-1166	-608	-416	-2507	-1486	-1974	-2213
0.20	604	869	-1552	-531	-617	-948	-636	-372	-2792	-1772	-1857	-2189
0.25	770	1106	-1548	-607	-174	-590	-624	-288	-2942	-2001	-1568	-1984
0.30	931	1338	-1493	-669	318	-168	-583	-176	-3007	-2183	-1197	-1682
0.35	1084	1557	-1426	-720	789	254	-521	-48	-3031	-2325	-816	-1351
0.40	1223	1755	-1374	-763	1184	622	-445	87	-3042	-2431	-484	-1046
0.45	1343	1927	-1356	-798	1465	900	-363	221	-3062	-2503	-241	-806
0.50	1439	2064	-1384	-825	1604	1061	-279	346	-3103	-2543	-114	-657
0.55	1506	2160	-1459	-844	1591	1094	-200	454	-3165	-2550	-115	-612
0.60	1539	2207	-1572	-852	1429	998	-129	539	-3241	-2521	-239	-670
0.65	1534	2200	-1708	-848	1136	789	-71	595	-3313	-2452	-469	-816
0.70	1486	2129	-1841	-826	746	491	-29	615	-3355	-2340	-769	-1023
0.75	1388	1990	-1936	-782	304	145	-6	596	-3330	-2176	-1090	-1249
0.80	1237	1773	-1949	-711	-127	-196	-3	533	-3190	-1951	-1368	-1436
0.85	1028	1473	-1828	-605	-471	-466	-20	425	-2876	-1653	-1519	-1514
0.90	755	1082	-1512	-457	-638	-587	-50	276	-2318	-1263	-1443	-1393
0.95	414	594	-929	-259	-520	-467	-78	101	-1421	-751	-1013	-959
1.00	0	0	0	0	0	0	0	0	0	0	0	0

2) ΔS^{ex} calc from XRD data

x_{REE}	ΔG^{ex}_Ce-La (J/mol)	ΔG^{ex}_Ce-Pr (J/mol)	ΔG^{ex}_Ce-Nd (J/mol)	ΔG^{ex}_Ce-Sm (J/mol)	ΔG^{ex}_Ce-Eu (J/mol)	ΔG^{ex}_Ce-Gd (J/mol)	ΔG^{mix}_Ce-La (J/mol)	ΔG^{mix}_Ce-Pr (J/mol)	ΔG^{mix}_Ce-Nd (J/mol)	ΔG^{mix}_Ce-Sm (J/mol)	ΔG^{mix}_Ce-Eu (J/mol)	ΔG^{mix}_Ce-Gd (J/mol)
0.00	0	0	0	0	0	0	0	0	0	0	0	0
0.05	185	346	-742	-169	-723	-836	-307	-146	-1234	-661	-1215	-1328

0.10	254	568	-1312	-413	-1084	-1317	-552	-238	-2118	-1219	-1889	-2123
0.15	307	767	-1679	-638	-1105	-1458	-740	-281	-2727	-1685	-2153	-2506
0.20	363	958	-1886	-827	-882	-1345	-877	-282	-3127	-2068	-2123	-2586
0.25	427	1145	-1981	-980	-506	-1063	-967	-249	-3375	-2374	-1900	-2457
0.30	498	1327	-2005	-1097	-58	-686	-1016	-187	-3519	-2611	-1573	-2201
0.35	577	1502	-1993	-1180	392	-281	-1028	-103	-3598	-2785	-1212	-1886
0.40	659	1664	-1975	-1231	790	98	-1009	-4	-3643	-2900	-878	-1570
0.45	742	1809	-1968	-1254	1093	412	-964	103	-3674	-2960	-612	-1294
0.50	820	1930	-1985	-1250	1273	630	-898	212	-3703	-2968	-445	-1088
0.55	890	2022	-2028	-1220	1316	737	-815	316	-3734	-2926	-389	-969
0.60	946	2077	-2092	-1166	1222	727	-722	409	-3760	-2835	-446	-941
0.65	981	2089	-2162	-1089	1005	611	-623	484	-3767	-2694	-600	-994
0.70	990	2048	-2215	-990	692	409	-524	534	-3730	-2504	-822	-1106
0.75	965	1947	-2222	-867	326	153	-429	553	-3616	-2261	-1068	-1241
0.80	897	1774	-2144	-723	-39	-111	-343	534	-3384	-1964	-1280	-1351
0.85	776	1518	-1934	-559	-336	-327	-272	470	-2982	-1607	-1383	-1375
0.90	585	1161	-1545	-381	-486	-431	-220	355	-2351	-1187	-1292	-1237
0.95	298	674	-929	-204	-411	-359	-194	182	-1421	-696	-903	-851
1.00	0	0	0	0	0	0	-197	-197	-197	-197	-197	-197

3) ΔG^{ex} calc Aq-SS equilibria

x_{REE}	ΔG^ex_Ce-La (J/mol)	ΔG^ex_Ce-Pr (J/mol)	ΔG^ex_Ce-Nd (J/mol)	ΔG^ex_Ce-Sm (J/mol)	ΔG^ex_Ce-Eu (J/mol)	ΔG^ex_Ce-Gd (J/mol)	ΔG^mix_Ce-La (J/mol)	ΔG^mix_Ce-Pr (J/mol)	ΔG^mix_Ce-Nd (J/mol)	ΔG^mix_Ce-Sm (J/mol)	ΔG^mix_Ce-Eu (J/mol)	ΔG^mix_Ce-Gd (J/mol)
0.00	0	0	0	0	0	0	0	0	0	0	0	0
0.05	93	228	208	-100	-10	-9	-399	-264	-284	-592	-502	-501
0.10	155	400	341	-164	-19	-20	-651	-406	-464	-969	-825	-826
0.15	191	531	414	-199	-33	-36	-857	-517	-634	-1247	-1080	-1083
0.20	209	631	437	-213	-52	-58	-1031	-609	-803	-1454	-1292	-1298
0.25	213	711	422	-214	-79	-87	-1180	-683	-972	-1608	-1473	-1481
0.30	209	776	378	-205	-115	-123	-1305	-738	-1136	-1720	-1629	-1637
0.35	199	834	315	-193	-160	-167	-1406	-771	-1290	-1798	-1765	-1771
0.40	187	888	240	-180	-212	-216	-1481	-780	-1428	-1848	-1881	-1884
0.45	176	940	160	-168	-272	-269	-1530	-766	-1545	-1874	-1977	-1975
0.50	166	990	82	-161	-335	-324	-1552	-728	-1636	-1879	-2053	-2043
0.55	159	1035	10	-159	-398	-378	-1547	-670	-1696	-1864	-2104	-2084
0.60	155	1073	-52	-160	-458	-428	-1513	-595	-1720	-1829	-2126	-2096

0.65	154	1097	-100	-166	-509	-468	-1451	-508	-1705	-1770	-2114	-2073
0.70	153	1099	-132	-172	-544	-494	-1361	-415	-1646	-1686	-2059	-2008
0.75	151	1071	-148	-177	-558	-501	-1243	-323	-1542	-1570	-1952	-1895
0.80	145	1000	-146	-175	-543	-481	-1095	-240	-1387	-1416	-1783	-1722
0.85	132	874	-129	-163	-489	-430	-916	-174	-1176	-1211	-1537	-1477
0.90	107	677	-96	-135	-388	-338	-699	-129	-902	-941	-1194	-1143
0.95	65	392	-52	-83	-228	-197	-427	-100	-544	-575	-720	-689
1.00	0	0	0	0	0	0	0	0	0	0	0	0

Table S3. Calculated excess entropy (ΔS^{ex}) and entropy of mixing (ΔS^{mix}) based on the two approaches presented in sections 4.1.2. and 4.2.1. with curves shown in Figure 12.

1) $\Delta G^{ex} = \Delta H^{ex}$												
x_{REE}	ΔS^{ex}_Ce-La J mol^{-1}K^{-1}	ΔS^{ex}_Ce-Pr J mol^{-1}K^{-1}	ΔS^{ex}_Ce-Nd J mol^{-1}K^{-1}	ΔS^{ex}_Ce-Sm J mol^{-1}K^{-1}	ΔS^{ex}_Ce-Eu J mol^{-1}K^{-1}	ΔS^{ex}_Ce-Gd J mol^{-1}K^{-1}	ΔS^{mix}_Ce-La J mol^{-1}K^{-1}	ΔS^{mix}_Ce-Pr J mol^{-1}K^{-1}	ΔS^{mix}_Ce-Nd J mol^{-1}K^{-1}	ΔS^{mix}_Ce-Sm J mol^{-1}K^{-1}	ΔS^{mix}_Ce-Eu J mol^{-1}K^{-1}	ΔS^{mix}_Ce-Gd J mol^{-1}K^{-1}
0.00	0	0	0	0	0	0	-	-	-	-	-	-
0.05	0	0	0	0	0	0	-	-	-	-	-	-
0.10	0	0	0	0	0	0	-	-	-	-	-	-
0.15	0	0	0	0	0	0	-	-	-	-	-	-
0.20	0	0	0	0	0	0	-	-	-	-	-	-
0.25	0	0	0	0	0	0	-	-	-	-	-	-
0.30	0	0	0	0	0	0	-	-	-	-	-	-
0.35	0	0	0	0	0	0	-	-	-	-	-	-
0.40	0	0	0	0	0	0	-	-	-	-	-	-
0.45	0	0	0	0	0	0	-	-	-	-	-	-
0.50	0	0	0	0	0	0	-	-	-	-	-	-
0.55	0	0	0	0	0	0	-	-	-	-	-	-
0.60	0	0	0	0	0	0	-	-	-	-	-	-
0.65	0	0	0	0	0	0	-	-	-	-	-	-
0.70	0	0	0	0	0	0	-	-	-	-	-	-
0.75	0	0	0	0	0	0	-	-	-	-	-	-
0.80	0	0	0	0	0	0	-	-	-	-	-	-
0.85	0	0	0	0	0	0	-	-	-	-	-	-
0.90	0	0	0	0	0	0	-	-	-	-	-	-
0.95	0	0	0	0	0	0	-	-	-	-	-	-
1.00	0	0	0	0	0	0	-	-	-	-	-	-
2) ΔS^{ex} calc from XRD data												
x_{REE}	ΔS^{ex}_Ce-La J mol^{-1}K^{-1}	ΔS^{ex}_Ce-Pr J mol^{-1}K^{-1}	ΔS^{ex}_Ce-Nd J mol^{-1}K^{-1}	ΔS^{ex}_Ce-Sm J mol^{-1}K^{-1}	ΔS^{ex}_Ce-Eu J mol^{-1}K^{-1}	ΔS^{ex}_Ce-Gd J mol^{-1}K^{-1}	ΔS^{mix}_Ce-La J mol^{-1}K^{-1}	ΔS^{mix}_Ce-Pr J mol^{-1}K^{-1}	ΔS^{mix}_Ce-Nd J mol^{-1}K^{-1}	ΔS^{mix}_Ce-Sm J mol^{-1}K^{-1}	ΔS^{mix}_Ce-Eu J mol^{-1}K^{-1}	ΔS^{mix}_Ce-Gd J mol^{-1}K^{-1}
0.00	0.0	0.0	0.0	0.0	0.0	0.0	0.0	0.0	0.0	0.0	0.0	0.0

0.05	-0.2	-0.5	0.0	0.0	-0.1	0.1	1.5	1.1	1.6	1.6	1.6	1.8
0.10	0.1	-0.6	0.3	0.3	0.3	0.6	2.8	2.2	3.0	3.0	3.0	3.3
0.15	0.4	-0.5	0.7	0.7	0.6	1.0	4.0	3.1	4.3	4.2	4.1	4.5
0.20	0.8	-0.3	1.1	1.0	0.9	1.3	5.0	3.9	5.3	5.2	5.1	5.5
0.25	1.2	-0.1	1.5	1.3	1.1	1.6	5.8	4.5	6.1	5.9	5.8	6.3
0.30	1.5	0.0	1.7	1.4	1.3	1.7	6.5	5.1	6.8	6.5	6.3	6.8
0.35	1.7	0.2	1.9	1.5	1.3	1.8	7.1	5.6	7.3	6.9	6.7	7.2
0.40	1.9	0.3	2.0	1.6	1.3	1.8	7.5	5.9	7.6	7.2	6.9	7.4
0.45	2.0	0.4	2.1	1.5	1.2	1.6	7.7	6.1	7.8	7.3	7.0	7.4
0.50	2.1	0.4	2.0	1.4	1.1	1.4	7.8	6.2	7.8	7.2	6.9	7.2
0.55	2.1	0.5	1.9	1.3	0.9	1.2	7.8	6.2	7.6	7.0	6.6	6.9
0.60	2.0	0.4	1.7	1.1	0.7	0.9	7.6	6.0	7.3	6.6	6.3	6.5
0.65	1.9	0.4	1.5	0.8	0.4	0.6	7.2	5.8	6.9	6.2	5.8	6.0
0.70	1.7	0.3	1.3	0.5	0.2	0.3	6.7	5.4	6.3	5.6	5.3	5.4
0.75	1.4	0.1	1.0	0.3	-0.1	0.0	6.1	4.8	5.6	5.0	4.6	4.6
0.80	1.1	0.0	0.7	0.0	-0.3	-0.3	5.3	4.2	4.8	4.2	3.9	3.9
0.85	0.8	-0.1	0.4	-0.2	-0.5	-0.5	4.4	3.4	3.9	3.4	3.1	3.0
0.90	0.6	-0.3	0.1	-0.3	-0.5	-0.5	3.3	2.4	2.8	2.4	2.2	2.2
0.95	0.4	-0.3	0.0	-0.2	-0.4	-0.4	2.0	1.4	1.7	1.5	1.3	1.3
1.00	0.0	0.0	0.0	0.0	0.0	0.0	0.7	0.0	0.0	0.0	0.0	0.0

3) ΔG^{ex} calc from Aq-SS equilibria

x_{REE}	ΔS^{ex}_Ce-La	ΔS^{ex}_Ce-Pr	ΔS^{ex}_Ce-Nd	ΔS^{ex}_Ce-Sm	ΔS^{ex}_Ce-Eu	ΔS^{ex}_Ce-Gd	ΔS^{mix}_Ce-La	ΔS^{mix}_Ce-Pr	ΔS^{mix}_Ce-Nd	ΔS^{mix}_Ce-Sm	ΔS^{mix}_Ce-Eu	ΔS^{mix}_Ce-Gd
	J mol^{-1}K^{-1}	J mol^{-1}K^{-1}	J mol^{-1}K^{-1}	J mol^{-1}K^{-1}	J mol^{-1}K^{-1}	J mol^{-1}K^{-1}	J mol^{-1}K^{-1}	J mol^{-1}K^{-1}	J mol^{-1}K^{-1}	J mol^{-1}K^{-1}	J mol^{-1}K^{-1}	J mol^{-1}K^{-1}
0.00	0.0	0.0	0.0	0.0	0.0	0.0	0.0	0.0	0.0	0.0	0.0	0.0
0.05	-0.1	0.1	3.2	0.3	2.4	2.7	1.5	1.8	4.9	1.9	4.1	4.3
0.10	-0.4	0.0	5.2	0.5	3.3	3.8	2.3	2.7	7.9	3.2	6.0	6.5
0.15	-0.8	-0.3	6.3	0.8	3.0	3.8	2.7	3.2	9.8	4.3	6.5	7.3
0.20	-1.3	-0.8	6.7	1.1	1.9	3.0	2.8	3.4	10.8	5.2	6.1	7.1
0.25	-1.9	-1.3	6.6	1.3	0.3	1.7	2.8	3.3	11.3	6.0	5.0	6.4
0.30	-2.4	-1.9	6.3	1.6	-1.5	0.1	2.7	3.2	11.4	6.6	3.6	5.2
0.35	-3.0	-2.4	5.8	1.8	-3.2	-1.4	2.4	3.0	11.2	7.2	2.2	4.0
0.40	-3.5	-2.9	5.4	2.0	-4.7	-2.8	2.1	2.7	11.0	7.6	0.9	2.8
0.45	-3.9	-3.3	5.1	2.1	-5.8	-3.9	1.8	2.4	10.8	7.8	-0.1	1.8
0.50	-4.3	-3.6	4.9	2.2	-6.5	-4.6	1.5	2.2	10.7	8.0	-0.7	1.1

0.55	-4.5	-3.8	4.9	2.3	-6.7	-4.9	1.2	1.9	10.6	8.0	-1.0	0.8
0.60	-4.6	-3.8	5.1	2.3	-6.3	-4.8	1.0	1.8	10.7	7.9	-0.7	0.8
0.65	-4.6	-3.7	5.4	2.3	-5.5	-4.2	0.8	1.7	10.8	7.7	-0.1	1.2
0.70	-4.5	-3.5	5.7	2.2	-4.3	-3.3	0.6	1.6	10.8	7.3	0.8	1.8
0.75	-4.1	-3.1	6.0	2.0	-2.9	-2.2	0.5	1.6	10.7	6.7	1.8	2.5
0.80	-3.7	-2.6	6.0	1.8	-1.4	-1.0	0.5	1.6	10.2	6.0	2.8	3.2
0.85	-3.0	-2.0	5.7	1.5	-0.1	0.1	0.5	1.5	9.2	5.0	3.5	3.6
0.90	-2.2	-1.4	4.7	1.1	0.8	0.8	0.5	1.3	7.5	3.8	3.5	3.5
0.95	-1.2	-0.7	2.9	0.6	1.0	0.9	0.5	1.0	4.6	2.2	2.6	2.6
1.00	0.0	0.0	0.0	0.0	0.0	0.0	0.0	0.0	0.0	0.0	0.0	0.0

XRD Rietveld refinement

The initial crystal structure and lattice parameter of rhabdophane was adopted from the monoclinic *C*2 structure of rhabdophane-(Sm) determined by Mesbah et al. (2014). This allowed determining first the crystal lattice parameters for the endmembers synthesized in our study and also determine peak broadening (i.e., due to small crystallite sizes) and shifts in 2θ angles and other parameters in MAUD (Lutterotti et al., 1999) before refining the lattice parameters of the binary solid solutions. A typical refinement in MAUD using the wizard consists of background and scale parameters, basic phase parameters, microstructure parameters, and crystal structure parameters. An example of structure refinement output for rhabdophane-(Sm) is shown in Fig. S1 with parameters listed in Table S4. The refined .cif file can be found in the accompanying Mendeley Data repository link.

Table S4. Crystal data and structure refinement parameters for rhabdophane-(Sm).

	(This study)	Mesbah et al. (2014)
formula	$SmPO_4 \cdot nH_2O$[1]	$SmPO_4 \cdot 0.667H_2O$
T (K)	room	293
system	monoclinic	monoclinic
space group	*C*2	*C*2
a (Å)	28.085(5)	28.0904(1)
b (Å)	6.829(1)	6.9466(1)
c (Å)	12.155(2)	12.0304(1)
β (°)	115.44(1)	115.23(1)
V (Å^3)	2105(1)	2123.4(4)
Density (g/cm^3)	4.846	4.8
Z	24	24
B_{iso}	0.008	0.00818
R_p	0.062	0.068
R_{wp}	0.042	0.091
R_{Bragg}	0.074	0.041

[1]Based on measured TGA-DSC data for Ce, Nd, and Gd rhabdophane endmembers (Table 5), n = 0.85-0.96. For the refinement a value of 0.667 was taken as standard for each rhabdophane.

Table S5. Fitted powder XRD data showing shifts of peak positions and FHWM for the 711 reflection in Ce-Nd rhabdophane and Ce-Gd rhabdophane endmembers and solid solutions.

		Peak center (2θ)					FHWM				
	x_{REE}	peak1	peak2	peak3	peak4	peak5	peak1	peak2	peak3	peak4	peak5
CePO4b	0.00	14.35	19.98	25.52	29.01	31.43	2.472	1.694	2.342	2.273	1.561
CePO4a	0.00	14.36	20.00	25.52	29.03	31.42	2.491	1.690	2.425	2.154	1.517
Ce90Nd10a	0.09	14.42	19.97	25.57	29.02	31.46	2.468	1.797	2.481	2.226	1.633
Ce75Nd25a	0.23	14.40	20.03	25.52	29.08	31.46	2.372	1.719	2.591	2.105	1.522
Ce65Nd35a	0.35	14.49	20.03	25.51	29.14	31.50	2.241	1.684	2.269	2.077	1.316
Ce35Nd65a	0.65	14.50	20.12	25.54	29.24	31.60	2.236	1.644	2.337	2.032	1.255
Ce25Nd75a	0.75	14.48	20.12	25.60	29.24	31.65	2.459	1.704	2.273	2.141	1.411
Ce10Nd90b	0.90	14.56	20.10	25.66	29.24	31.70	2.644	1.839	2.339	2.250	1.537
NdPO4b	1.00	14.56	20.20	25.69	29.35	31.76	2.039	1.600	2.185	2.165	1.400
NdPO4a	1.00	14.60	20.14	25.64	29.32	31.72	2.387	1.723	2.053	2.061	1.315
Ce90Gd10	0.08	14.42	20.02	25.51	29.10	31.45	2.567	1.659	2.272	2.046	1.319
Ce75Gd25	0.18	14.54	20.10	25.58	29.23	31.58	2.257	1.593	2.093	2.063	1.295
Ce65Gd35	0.28	14.56	20.09	25.57	29.27	31.59	2.154	1.570	1.951	2.017	1.256
Ce50Gd50	0.42	14.59	20.18	25.62	29.40	31.70	1.927	1.515	2.108	2.043	1.215
Ce35Gd65	0.58	14.65	20.23	25.66	29.46	31.76	2.022	1.549	2.009	1.994	1.186
Ce25Gd75	0.70	14.67	20.31	25.76	29.61	31.91	2.012	1.590	2.097	1.965	1.098
Ce10Gd90	0.86	14.75	20.38	25.93	29.70	32.05	2.155	1.729	2.632	2.028	1.268
GdPO4b	1.00	14.80	20.39	25.97	29.72	32.05	1.465	1.306	2.046	1.951	1.172

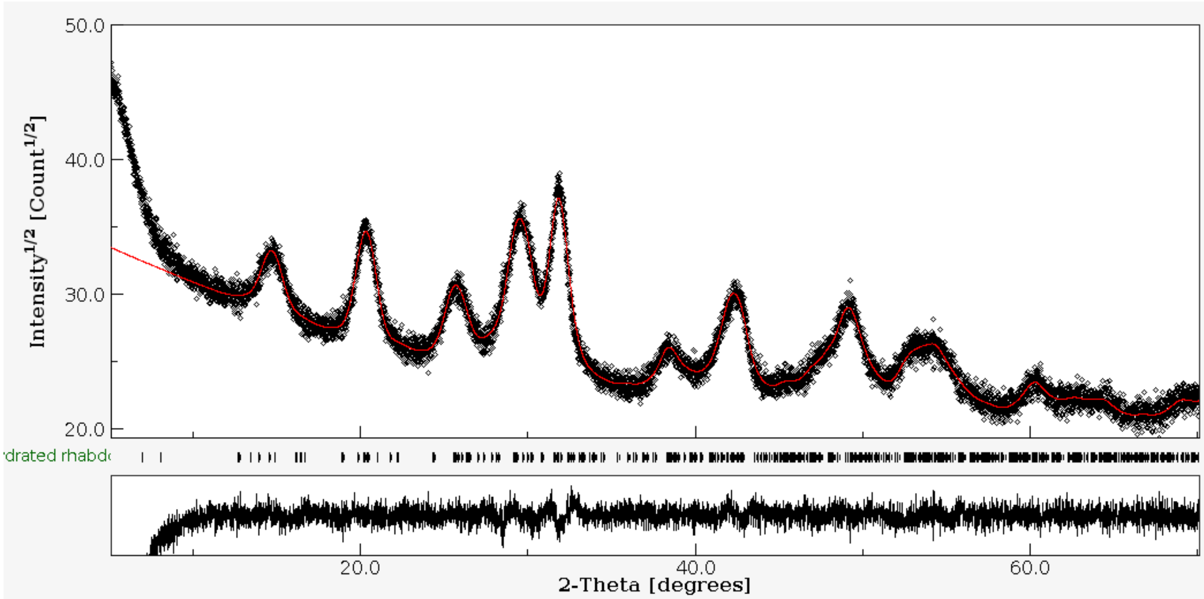

Figure S1. Example of Rietveld refinement output using Maud showing the observed, calculated, and residuals for rhabdophane-(Sm). The structure refinement and crystal structure data are listed in Table S4.

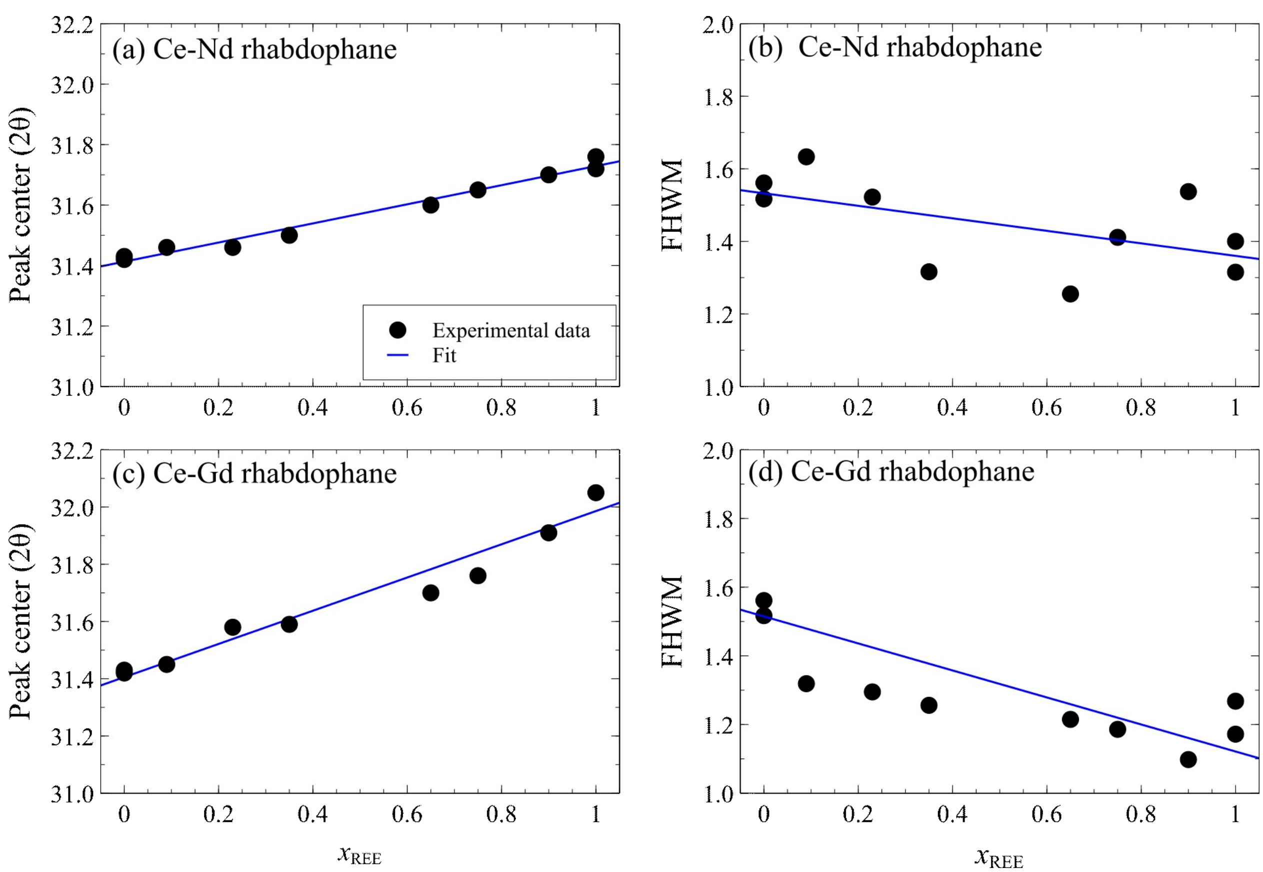

Figure S2. Fitted powder XRD spectra showing the shift of peak positions and FHWM for the 711 reflection (Fig. 3) for (a-b) Ce-Nd rhabdophane, and (c-d) Ce-Gd rhabdophane endmembers and solid solutions.

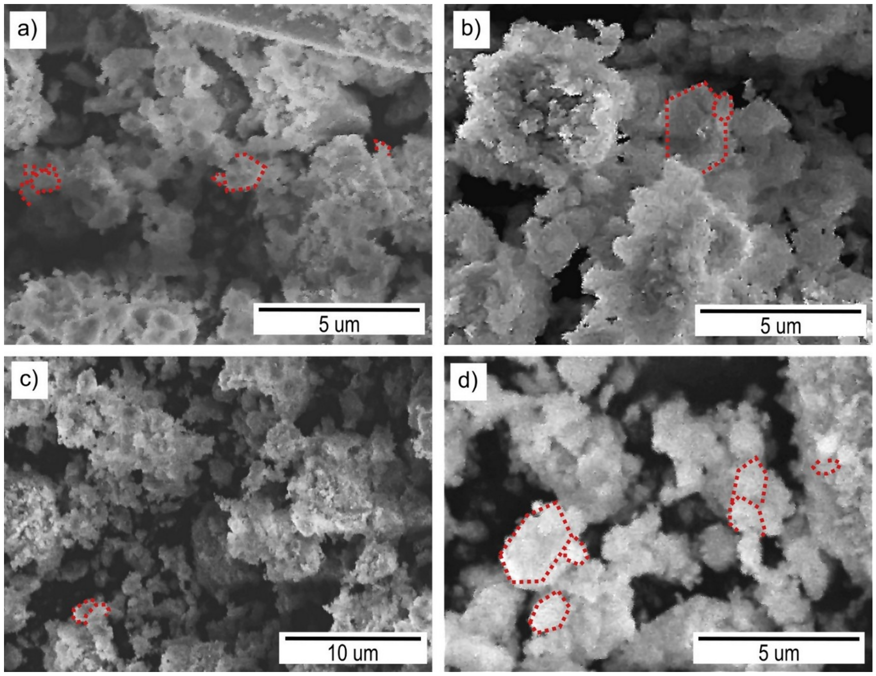

Figure S3. Scanning electron microscope images of Ce-Pr rhabdophane endmembers and solid solutions. a) Rhabdophane-(Ce) and (b) rhabdophane-(Pr) endmembers and (c-d) $Ce_{0.5}Pr_{0.5}PO_4 \cdot 0.667H_2O$ solid solutions showing that some of the larger grains are ~1 um in size showing a monoclinic shape and smaller grain aggregates of 100s of nm in size.